Three-Dimensional Radio Channel Modeling for Mobile Communication Systems

Doktor Ingeniør Dessertation

Magne Pettersen

Department of Telecommunications
Norwegian University of Science and Technology
N-7491 Trondheim, Norway

September 2001

URN:NBN:no-1290

URN:NBN:no-1290

Abstract

The work described in this report is within the area of three-dimensional (3D) radio channel modeling for mobile communications. The focus was towards rural areas, because radio coverage of rural areas is more costly when using higher frequencies, comparing UMTS to GSM. In addition seasonal and environmental variations are strongest here. The model used was a *3D radar model*, comprised of a 2D vertical Tx-Rx-plane component and a 3D components to include off-axis scattering. The latter components are estimated using bistatic radar techniques. The model is able to provide an accurate estimation of the path loss (signal level), and is also able to estimate time dispersion and angular dispersion, taking into account off-axis contributions. Radio frequencies around 2 GHz were selected, as these are the most important frequency bands for 3. generation mobile systems, even though the envisaged approach supports radio planning for GSM 900 and WLAN systems.

A novel approach to the modeling of scattering from random rough surfaces for 3D channel modeling was developed. This *amplitude/phase model* is simple and accurate compared to conventional models. It makes no inherent assumption about the degree of roughness, making it suited to model all surfaces. The model outperforms the conventional models Plane surface, SPM, Kirchoff and Oren with respect to accuracy by 1.5 to 10 dB depending on the degree of roughness.

An experimental methodology to characterise random rough surfaces was developed. The work characterised natural surfaces such as asphalt, grass, agriculture, and forest, each of them having a different degree of roughness. Variations due to weather and seasonal changes were taken into account. Typical surface height variations estimated were 10 mm for asphalt, 25 mm for grass, 100 mm for ploughed field and 500 mm for forest. Snow reduced the apparent roughness of ploughed field by 50 %, water on grass increased the reflection coefficient by 50 %.

An analysis of the implications of the results on 3D channel modeling was performed using a demonstration model. The analysis included a comparison between 2D and 3D model prediction for different area types and land use classes. Also the prediction sensitivity to seasonal and weather variations and model parameter variations were inspected. A 3D model is necessary when the 2D component is attenuated more than typically 15 dB relative to free space, depending on area and land usage. In the network planning example Lillehammer (N) this attenuation of at least 15 dB existed in 40 % of all locations. Weather and seasonal variations may change the mean predicted value by up to 4-5 dB.

URN:NBN:no-1290

URN:NBN:no-1290

Preface

The work described in this thesis took place during the period 1998-2001. The experimental work was performed in and around Kjeller, Norway, mainly in 1998 and 1999. The theoretical work was performed at Kjeller, Norway, as well as Ipswich and Bristol, UK, during August 1999 to August 2000.

I would like to thank Telenor for financing my studies, and thereby providing me with the opportunity to perform this work. Also, I want to thank my supervisors, Dr. Josef Noll at Telenor, and Professor Gunnar Stette at the Norwegian University of Science and Technology for their invaluable guidance throughout the whole period. I want to thank my colleagues at Telenor for useful and interesting discussions, especially Lars Bråten, Ragnar Eckhoff, Per Hjalmar Lehne and Olaf Røstbakken. I could not have performed the experiments on my own, and I am grateful for the people who helped me, both with the measurements and with building the equipment, in particular Egil Antonsen.

During my stay in the UK I spend some time at BT Laboratories, Ipswich. I would like to thank Dr. Adrian Sharples and Dr. Jon Moss for their contributions to this work. Also, I am grateful to Dr. Andy Nix and Dr. Eustace Tameh at the University of Bristol for letting me use their propagation prediction tool and for providing test digital elevation maps from the Bristol area.

Lastly I want to thank my friends and family, for their support and for being who they are, especially my parents. My father Terje Pettersen doubled as a supervisor, and provided very useful inputs.

URN:NBN:no-1290

List of abbreviations

3GPP	Third Generation Partnership Project
AS	Azimuth Spread
BRAN	Broadband Radio Access Networks
CDMA	Code Division Multiple Access
CIR	Complex Impulse Response
DEM	Digital Elevation Map
DoA	Direction of Arrival
DS	Delay Spread
EDGE	Enhanced Data rate for GSM Evolution
EFIE	Electric Field Integral Equation
EIRP	Equivalent Isotropic Radiated Power
EM	Expectation-Maximisation
ESPRIT	Estimation of Signal Parameters via Rotational Invariance Techniques
ETSI	European Telecommunications Standards Institute
GO	Geometrical Optics
GPRS	General Packet Radio Service
GSM	Global System for Mobile communications
GTD	Geometrical Theory of Diffraction
Hiperlan	High Performance Local Area Network
HPBW	Half Power Beamwidth
IMT	International Mobile Telecommunications
ITU	International Telecommunication Union
JTC	Joint Technical Committee
LOS	Line Of Sight
MFIE	Magnetic Field Integral Equation
ML	Maximum Likelihood
OLOS	Obstructed Line Of Sight
PCS	Personal Communications Services
PDF	Probability Density Function
PEC	Perfect Electric Conductor
PO	Physical Optics

SAGE	Space-Alternating Generalised Expectation-maximisation
STD	(statistical) Standard Deviation
UMTS	Universal Mobile Telecommunications System
UTD	Uniform Theory of Diffraction
WLAN	Wireless Local Area Network

List of symbols

ϕ	Azimuth angle
θ	Elevation angle (relative to vertical)
η	Doppler frequency
τ	Time Delay
λ	Wavelength
σ	Conductivity
ν	Fresnel-Kirchoff diffraction parameter
ψ	Complement of incidence elevation angle
δ	Forward scattering coefficient
σ	Radar cross section
Γ	Reflection coefficient
η	Surface impedance
$\delta()$	Dirac Delta function
λ_0	Wavelength in free space
σ^0	Radar cross section per unit area
σ_0	Rayleigh parameter
ϕ_i	Incidence azimuth angle
θ_i	Incidence elevation angle (relative to vertical)
ε_r	Relative permittivity
ε_r'	Real part of relative permittivity
ε_r''	Imaginary part of relative permittivity
ϕ_s	Scattering azimuth angle
θ_s	Scattering elevation angle (relative to vertical)
a	Fieldstrength
D()	Doppler spectrum
E	Electric fieldstrength
f	Frequency
G()	Green's function
g	Antenna gain
g_r	Receiving antenna gain
g_t	Transmitting antenna gain

H	Magnetic fieldstrength
h()	(Complex) impulse response
k	Propagation constant
k'	Real part of propagation constant
k''	Complex part of propagation constant
k_0	Propagation constant in free space
L	Path loss
L_0	Surface correlation length
n	Refractive index
P	Power
p	Polarisation factor
P()	Power azimuth spectrum
P_r	Received power
P_t	Transmitted power
q	Depolarisation factor
Q()	Power delay profile
R	Propagation distance
R_r	Rx-scatterer distance
R_t	Tx-scatterer distance
S	Power density
S()	Scattering function
T	Refraction coefficient
T()	(Complex) transfer function

Contents

1 Scope and motivation

Within the area of terrestrial mobile communications there is a rapid development towards new services and higher bit rates. The entry into packet based data services is GPRS (General Packet Radio Service), which will soon be followed by more advanced technologies. GPRS has an envisaged maximum bit rate of 115 kbit/s, which will result in user bit rates up to approximately 50 kbit/s. EDGE (Enhanced Data rate for GSM Evolution) is an enhanced GSM (Global System for Mobile communications) implementation that by using new modulation schemes will offer up to 384 kbit/s services in a microcell environment. UMTS (Universal Mobile Telecommunications System) is the European implementation of the third generation mobile communication system, which will provide user bit rates up to 1-1.5 Mbit/s (typical maximum achievable value for microcell [Holma00]). UMTS is standardised by ETSI1, and will be a part of the world wide International Mobile Telecommunications 2000 (IMT-2000) standard, being standardised by ITU2. UMTS, as defined by 3GPP3, is in accordance with the third generation requirements described in the IMT-2000 report from Helsinki 1999 [ITU99].

Wireless Local Area Networks (WLAN),) like the BRAN family of standards being developed within ETSI, will provide up to 25 Mbit/s user bit rate in 2001/2002 (typical value for Hiperlan/2 [Torsner99]), and considerable higher bit rates in the next generation. While the data calls in the GSM network are in the order of 4% (1999) of the total traffic, data calls contribute to more than 50% of the total traffic in the fixed network. It is expected that in the future a similar trend will be visible for cellular networks. This trend will be accelerated by the new systems mentioned above offering a considerable improvement with respect to the 9,6 kbit/s currently being the standard within most GSM networks.

The growing traffic will contribute to an increased demand for capacity, which means that efficient use of the limited frequency spectrum is required. This will put demands on optimal system design as well as radio network roll-out. With respect to both these aspects it is essential to have high performance radio channel prediction tools. Accurate models to describe the radio channel are necessary to design the mobile communications systems. In addition radio channel models are essential to ensure a cost efficient radio planning and base station deployment while still maintaining capacity and quality of service. Thus, it is important that radio prediction models become more accurate and take into account a wide range of topographies and demographies.

The scope of the work described in this report is to enhance the radio planning tools to be used for future terrestrial mobile communications systems. These tools should be superior to existing ones and be able to

- estimate the channel characteristics (i.e. path loss and variance due to environmental changes) of the mobile radio channel accurately to allow efficient radio planning,
- estimate the time dispersion (impulse response) of the channel to allow the estimation of the behaviour of high speed, large bandwidth systems, and

[1] European Telecommunications Standards Institute.

[2] International Telecommunications Union

[3] 3GPP (Third Generation Partnership Project) is a global project devoted to developing technical specifications for third generation mobile systems based on evolved GSM networks.

- estimate the direction of arrival of the radio signal components to allow the estimation of the behaviour of systems employing smart antennas[4] and multiple-input-multiple-output (MIMO) systems[5].

In addition the models should be flexible and

- operate over a wide range of radio frequencies, with a focus on 2 GHz, which is a "hot spot" for future mobile communications, but also at 5 GHz, used for wireless local area networks (WLAN), and mm.-wave frequencies, planned for future broadband systems, and for the next generation of WLAN,
- operate over a wide range of environment types, and estimate mean and statistical variations due to environmental and seasonal changes as e.g. harvest, rain or snow.

Since the dominating propagation mechanisms will be different depending on the type of environment, it will be necessary to use specific models in different area types. Taking into account the frequency dependence of the mobile radio channel, it may also be desirable to use specific models for the various frequency bands.

A large number of approaches are currently being used in channel modeling. The models range from purely statistical to deterministic. Statistical models are empirical, based on measurements only and describe the statistical behaviour of the radio channel in a particular area type. These types of models are typically used in system simulations, system design and to aid initial estimates of the required network topology. Deterministic models on the other hand are models that take into account the knowledge about the terrain belonging to a particular radio link and estimates the radio channel characteristics for this link. The terrain data are normally acquired from digital elevation maps (DEM). These types of models are typically used for radio planning of a system in a specific area.

Radio channel models also differ in the parameters being used to describe the channel. *Narrowband models* are concerned only with the signal level (path loss), while *wideband models* also estimate the time dispersion (impulse response). *Directional models* provide information about the direction-of-arrival (DoA) of the signal components.

In radio planning tools deterministic channel models are preferable, as they allow a higher accuracy for a specific link, taking into account auxiliary data. The accuracy of the estimation in this type of models is limited by a number of factors, of which two are of principle concern:

1. The terrain description. The DEMs will have inaccuracies with respect to both position and size of obstacles and terrain formations. In addition season dependant obstacles like foliage will not be accurately described. Also, the terrain and foliage needs to be described by its electromagnetic properties at the desired frequency. This task on its own is quite difficult, as the outdoor environment changes with season and weather. Obviously, the terrain description will neither cope with moving objects like cars or people. The ability to describe the terrain accurately is one of the fundamental limitations in deterministic channel modeling.

[4] *Smart antennas* are base station antennas with an adaptive antenna diagram, able to receive and transmit in the direction of the desired user only. This definition follows the one from Lehne and Pettersen [Lehne99].

[5] *MIMO systems* use array antennas on both transmitter and receiver and can exploit the mobile radio channel properties to increase link capacity.

2. The model assumptions. Models that solve the propagation equations through the entire space, as e.g. *integral equation* methods, are computationally intensive. In order to limit the computational effort, models are developed which use underlying assumptions about the radiowave propagation. Examples of such assumptions are the Kirchoff based *geometrical optics* (GO) or *physical optics* (PO) approaches, which use the assumption of large obstacles, compared to the electromagnetic wavelength. The validity of these assumptions will depend on the frequency and the terrain.

The availability of DEMs is of principle concern when performing radio planning, and as it is normally unrealistic to develop or digitise maps for the sole purpose of planning a radio network, the planning must normally be based on already available map underlay. In many parts of the world these maps will be low detail, making propagation prediction of the type described in subsequent chapters of this report difficult.

The work described in this report is performed in cooperation with a project sponsored by Telenor. The objectives were to identify requirements for the next generation of radio planning tools. It was in particular important to evaluate different types of channel models and make suggestions about models to be used for different area types. The main emphasis has been put on the usefulness of the method as seen from an operator's point of view; the accuracy, the complexity and time consumption and the inherent uncertainties due to weather and seasonal changes or map inaccuracies as described above. The scope of the work covered in this report is limited to rural areas without building, due to the following two reasons: Firstly, the use of higher frequencies in UMTS compared to GSM makes radio network planning more costly in rural areas. Secondly, seasonal and environmental variations are strongest in rural areas. The focus is on frequencies around 2 GHz as foreseen for UMTS, since deployment of high frequency systems are limited to indoor or very dense urban environments in the foreseeable future.

The work on the rural area models can be divided into four main tasks:

1. Theoretical model study*:* Evaluation of existing types of radio channel prediction models, based on the requirements defined in this chapter. If necessary a new model was to be developed.

2. Propagation study: Experimental evaluation of propagation assumptions, like models for reflection/scattering from rough surfaces. Suggestions of extensions and modifications to existing models.

3. Model implementation: Implement the chosen model extensions in software. The implemented model will make propagation predictions based on 3D scattering from natural surfaces, taking into account environmental and seasonal variations.

4. Validation and sensitivity analysis*:* Verify the model accuracy by comparing with measurements and perform a sensitivity analysis with respect to key parameters.

This report mainly focuses on the first two tasks above. The latter two tasks are accomplished in a more general way. A demonstration implementation has been developed, as described in Chapter 7. A sensitivity analysis was carried out using this implementation on example scenarios. More detailed work is left for future studies.

Chapter 2 introduces the necessary definitions of terms as well as the chosen mathematical description of the mobile radio channel. The most important propagation mechanisms are also discussed briefly. Chapter 3 contains an analysis of the different existing types of radio channel models, as well as an evaluation with respect to the requirements. The type of model recommended for rural areas uses a 2D solution in the vertical plane through transmitter and

receiver, and uses a 3D extension to identify dominant off-axis scatterers. The contributions from these scatterers are estimated using bistatic radar theory. This type of model is referred to as a 3D radar model. Chapter 4 describes existing theory of electromagnetic scattering from rough surfaces, which is essential in the 3D extension of the model. Existing implementations using the techniques mentioned are discussed and compared. Chapter 5 gives a novel approach to model scattering from rough surfaces, and describes experiments performed to verify and test scattering from different natural surfaces. Chapter 6 contains a performance analysis of the new model in comparison with existing models for the scattering measurements. Chapter 7 contains suggestions about usage of the model, including a description of the implementation and a discussion of the parameterisation. Also, the chapter contains results from a sensitivity analysis using a demonstration implementation of a 3D radar model. A discussion of applicability and suggestions for future work is included. Chapter 8 contains the main conclusions from the work undertaken.

The novel work in the report is mainly within the following areas:

- The development of a novel approach to the modeling of scattering from random rough surfaces for 3D channel modeling. The model is simple, accurate compared to other models and makes no inherent assumption about the degree of roughness on the surface.
- The development of an experimental methodology to characterise random rough surfaces. Characterisation of a number of natural surfaces was carried out, including the inspection of variations due to weather and seasonal changes.
- An analysis using a test 3D channel model implementation. The analysis included a comparison between 2D and 3D model prediction for different area types and land use classes. Also the prediction sensitivity to seasonal and weather variation as well as model parameter variations was inspected.

2 The characteristics of the mobile radio channel

In the first section of this chapter, the basic mathematical description of the mobile radio channel is defined. In the second section some of the propagation mechanisms that are most important in the terrestrial mobile radio channel are discussed. The most common assumption for analysis of mobile channels is that of ray theory, leading the radio propagation to be along straight lines only bent by refraction, reflection, diffraction and scattering [COST231_98]. These are the concepts of Geometrical Optics (GO), and are approximately valid under a high frequency assumptiom and is the underlying assumption used in the remains of this chapter.

2.1 Terminology

In a mobile radio channel the transmitted signal will arrive at the receiver from various directions over a multiplicity of paths due to reflections and diffractions. This will be the case both from the mobile station to the base station (uplink) and in the opposite direction (downlink). Mathematically this means that when *u(t)* is the transmitted baseband signal the received signal in the most general case can be expressed as

$$y(t) = \int\int\int\int g_t(\phi,\theta) g_r(\phi,\theta) h(\tau,\phi,\theta,\eta) e^{j2\pi\eta t} u(t-\tau) d\tau d\phi d\theta d\eta \qquad \textit{(eq. 1)}$$

In this equation $g_t(\phi,\theta)$ *and* $g_r(\phi,\theta)$ are the complex antenna radiation patterns in azimuth (ϕ) and elevation (θ) angles on transmit and receive, respectively. *h(τ,ϕ,θ,η)* is the four-dimensional impulse response function in azimuth, elevation, relative time delay (τ) and Doppler frequency (η) domains. The most usual assumption is that the signal arriving at the receiver is a sum of a finite number of plane waves [Bello63]. In this case the impulse response can be written as

$$h(\tau,\phi,\theta,\eta) = \sum_{l=1}^{L} \alpha_l \delta(\tau-\tau_l)\delta(\phi-\phi_l)\delta(\theta-\theta_l)\delta(\eta-\eta_l) \qquad \textit{(eq. 2)}$$

where δ denotes the Dirac Delta function. L is the number of waves. For each wave α_l is the complex amplitude, ϕ_l and θ_l are the azimuth and elevation incidence angles and η_l is the Doppler frequency. This type of radio channel, where the signal arrives via a number of independent paths, is often referred to as a *multipath propagation channel*.

For outdoor environments the elevation angle is often neglected, removing the dependency on θ from the equations above. In a stationary environment, the Doppler frequency will be zero for all components, removing η from the equations. Thus, in a stationary outdoor environment the impulse response is written

$$h(\tau,\phi) = \sum_{l=1}^{L} \alpha_l \delta(\tau-\tau_l)\delta(\phi-\phi_l) \qquad \textit{(eq. 3)}$$

If the dependency on direction is disregarded, the impulse response can be written simply as

$$h(\tau) = \sum_{l=1}^{L} \alpha_l \delta(\tau-\tau_l) \qquad \textit{(eq. 4)}$$

This is often called a *tapped delay line* description. The description of the radio channel given in this section is equivalent to the radio channel being described as a linear filter in the temporal and/or spatial domains.

2.2 Propagation mechanisms

A number of propagation mechanisms will contribute to the multiplicity of signal components at the receiver. A short description of the most important mechanisms for the frequency bands relevant for mobile communications under the ray theory assumption will be given in this section.

2.2.1 Line-of-sight, obstructed line-of-sight

Line-of-sight

In the case where there are no obstructions near the line between transmitter and receiver, there will be a *direct* signal component, which is called the *line-of-sight* (LOS) component. This component can be assumed to follow the well-known laws of free space propagation. Assuming isotropic antennas, the ratio of received (P_r) to transmitted (P_t) power is given by (e.g. [Parsons92])

$$\frac{P_r}{P_t} = \left(\frac{\lambda}{4\pi R} \right)^2 \qquad \textit{(eq. 5)}$$

where λ is wavelength [m] and R is the distance between transmitter and receiver. In dB this can be written

$$P_r = P_t - 20\log(f) - 20\log(R) + 147.6 \qquad \textit{(eq. 6)}$$

where f is the frequency [Hz], R is the distance [m] and P_t is the transmitted power [dB].

Obstructed line-of-sight, refraction

In many cases the direct signal component exists, but is attenuated by some sort of obstruction. This is often called *obstructed line-of-sight* (OLOS). In a mobile radio channel this can become significant for instance in the case of foliage between transmitter and receiver or for indoor to outdoor propagation. The geometry and the electrical parameters of the obstruction determine the attenuation. Figure 1 shows the case of a “slab-like” obstruction. The signal attenuation in this case is given by the amount of power being reflected back from the surfaces, and the loss in the material. The signal that propagates through the slab (the useful signal in this case) is called the overall refraction. Figure 1 a) illustrates the multiple reflections and refractions in the two surfaces. The overall refraction coefficient T_O in such a case can be shown to be [Pahlavan95]

$$T_O = \frac{(1-\Gamma)P_D P_T}{1-\Gamma^2 {P_D}^2 P_A} \qquad \textit{(eq. 7)}$$

where Γ is the reflection coefficient in the boundary from air into the slab (the calculation of the reflection coefficient will be performed in the next section). The other parameters are defined as

$$P_D = e^{-j \cdot k_S \cdot \frac{d}{\cos\theta}}, \quad P_A = e^{2 \cdot k_0 \frac{d}{\cos\theta} \cdot \sin^2\theta}, \quad P_T = e^{-j \cdot k_0 \cdot \frac{d}{\cos\theta}} \qquad \textit{(eq. 8)}$$

where k_S is the propagation constant in the slab and k_0 is the propagation constant in free space. The propagation constant k is in general defined as

$$k = \frac{2\pi}{\lambda_0 \sqrt{\varepsilon_r}} = \frac{k_0}{\sqrt{\varepsilon_r}} \qquad \textit{(eq. 9)}$$

where λ_0 is the wavelength in free space and ε_r is the relative permittivity, which for a lossy material will be complex, defined as

$$\varepsilon_r = \varepsilon_r' - j \cdot \varepsilon_r'' = \varepsilon_r' - j60\sigma\lambda \qquad \textit{(eq. 10)}$$

where σ is the conductivity.

When the material is lossy, the propagation constant is complex and the electric field strength E along an axis z can be written as [Marshall90]

$$E(z) = E_0 e^{-jkz} = E_0 e^{-\alpha z} e^{-j\beta z} \qquad \textit{(eq. 11)}$$

where E_0 is the field strength at the slab entry point, defined as $z = 0$, and the loss factor L is given as

$$L[dB/m] = 20 \cdot \log\left(e^{\alpha}\right) = 8.68 \cdot \alpha[dB/m] \qquad \textit{(eq. 12)}$$

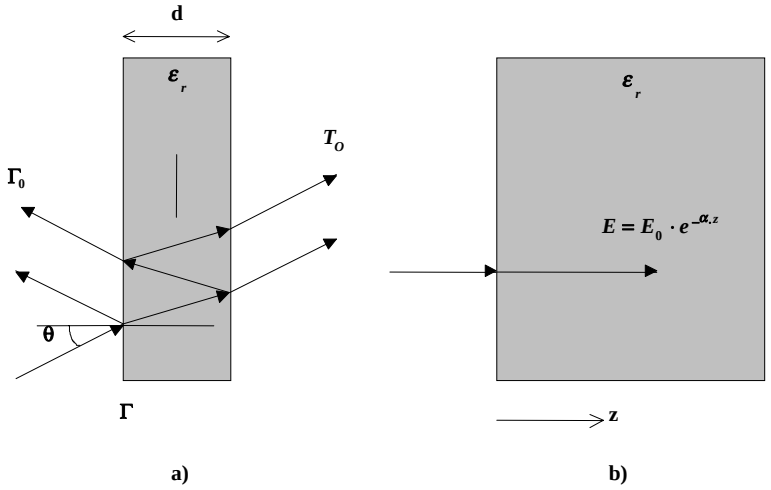

Figure 1. Illustration of obstructed line-of-sight case. a) Propagation through a slab, multiple reflections lead to an overall reflection coefficient Γ_O and an overall refraction coefficient T_O. b) Electrical field strength E decreasing in a lossy material. Taken from [Pahlavan95]

2.2.2 Reflections

When two media with different electrical properties are separated by a surface, an incident wave will be partly reflected and partly refracted. The reflection of waves at surfaces is a very important mechanism in mobile radio channels. The reflection coefficients will depend on the incidence angle of the wave with respect to the surface, and the electrical properties of the two media. In this subsection it will be made a distinction between the cases of plane surfaces, giving rise to specular reflections, and rough surfaces, giving rise to diffuse scattering. A more detailed discussion of the latter case can be found in Chapter 4.

Plane surfaces, specular reflections

Figure 2 illustrates the case of a plane surface. It is assumed that medium 1 is free space, and medium 2 is a medium with relative complex permittivity ε_r (ε_r in free space is 1). It should be distinguished between the cases of horizontal[6] and vertical[7] polarisation.

[6] Horizontal polarisation is defined as the case when the electric field vector is parallel with the direction of the plane of separation.

[7] Vertical polarisation is defined as the case when the magnetic field vector is parallel with the direction of the plane of separation.

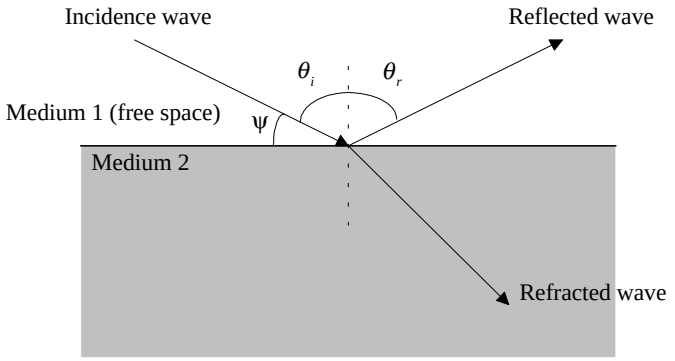

Figure 2. Reflection from plane surfaces.

Using the boundary conditions for the electric and the magnetic fields, it is possible to calculate the reflection coefficient of the surface. The angle of reflection θ_r will always be equal to the angle of incidence θ_i[8]. When the incidence wave is horizontally polarised, the Fresnel reflection coefficient can be expressed as [Pahlavan95]

$$\Gamma_h = \frac{\sin\psi - \sqrt{\varepsilon_r - \cos^2\psi}}{\sin\psi + \sqrt{\varepsilon_r - \cos^2\psi}} \qquad \textit{(eq. 13)}$$

where ψ is the complement of the angle of incidence as shown in Figure 2. When the wave is vertically polarised the reflection coefficient is

$$\Gamma_v = \frac{\varepsilon_r \sin\psi - \sqrt{\varepsilon_r - \cos^2\psi}}{\varepsilon_r \sin\psi + \sqrt{\varepsilon_r - \cos^2\psi}} \qquad \textit{(eq. 14)}$$

In the case of dielectric media, the vertical reflection coefficient will be zero for a certain angle of incidence, given by

$$\theta_i = \tan^{-1}(\sqrt{\varepsilon_{r\_2}}) \qquad \textit{(eq. 15)}$$

where ε_{r_2} is the (real) relative permittivity in medium 2, and medium 1 is (still) assumed to be vacuum. This angle is called the *Brewster angle*. In the more general case of a medium with non-zero conductivity there will not be a zero but a minimum, at an angle referred to in this

[8] The angle of incidence is defined relative to the normal vector of the surface.

case as the *pseudo-Brewster angle*. Figure 3 shows the absolute value of Γ in the case of horizontal and vertical polarisation for medium dry soil (ε_r'=15, σ=0.1). The *pseudo-Brewster angle* in this case appears at around 75°[9].

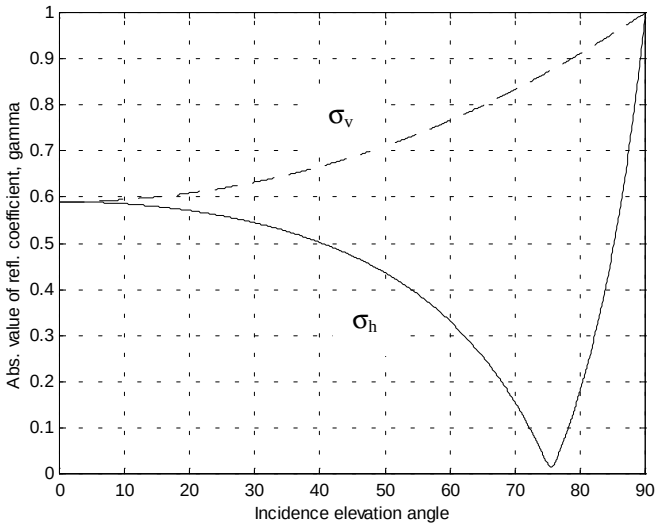

Figure 3. Reflection coefficient as a function of incidence angle for vertical (solid) and horizontal (dashed) polarisation. Example for medium dry soil (ε_r'=15, σ=0.1: [Boithias87]), 2 GHz.

The expressions in eq. 13 and eq. 14, giving contribution only in the direction $\theta_i = \theta_r$, is valid only under the assumption that the reflecting surface is infinite. For practical applications, these surfaces are known from earth- or sea-reflections.

If the reflecting area cannot be assumed large, the scattered signal will be spread to other directions, and some other method must be used to solve the scattering problem. This can for instance be done by solving for the boundary conditions and using the surface equivalence theorem [Balanis89]. These are techniques well known e.g. from antenna theory. As an example, consider a square, plane surface with dimensions $a \cdot b$ as shown in Figure 4. The incident wave is plane, vertically polarised and arriving with an incidence angle θ_i. In this case the power of the scattered signal can be written

[9] In [DeRoo94] it was observed in experiments that the (pseudo-)Brewster angle was shifted towards slightly lower angles for a rough surface compared to a plane surface, but no theoretical explanation to the phenomenon was given.

$$P_S = const \cdot \left(\cos^2\theta_S \cdot \sin^2\phi_S + \cos^2\phi_S\right) \cdot \left[\frac{\sin X}{X}\right]^2 \cdot \left[\frac{\sin Y}{Y}\right]^2$$

$$X = k_0 \cdot \frac{a}{2} \cdot \sin\theta_S \cdot \cos\phi_S \qquad \textit{(eq. 16)}$$

$$Y = k_0 \cdot \frac{b}{2}\left(\sin\theta_S \cdot \sin\phi_S - \sin\theta_i\right)$$

In Figure 5 plots of the scattered power in the case of $\theta_i = 45°$ for the cases a) $a = b = 1\lambda$ and b) $a = b = 5\lambda$ are shown. Note that in both cases the maximum power is found in the specular direction, $\theta_i = \theta_S, \phi_S = 90°$. Note also that as the surface gets larger the "beam" gets narrower and will in the limit approach the large surface case described earlier in this section.

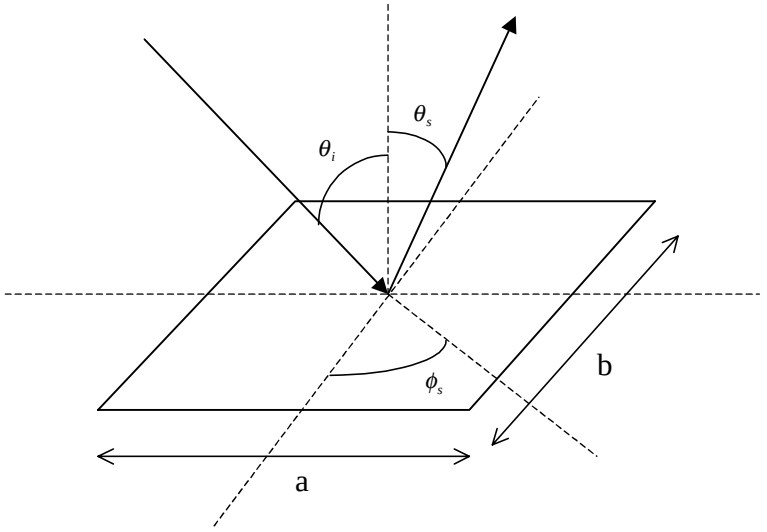

Figure 4. Scattering from a plane, square surface

URN:NBN:no-1290

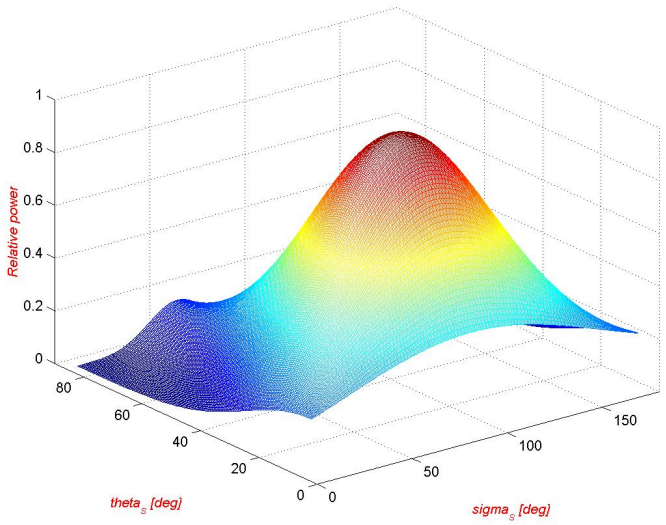

a)

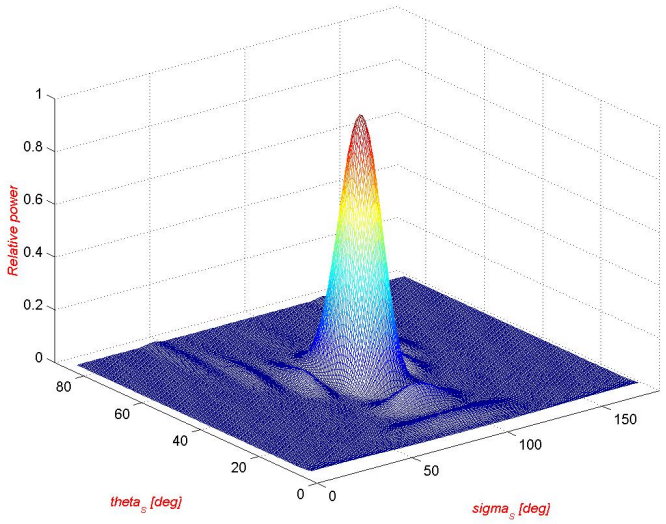

b)

Figure 5. Scattering from plane surface, vertical polarisation, θi=45°. a) a=b=1 λ. b) a=b=5 λ

It can be shown by Huygens principle (e.g. [Boithias87]) that most of the energy in the reflection comes from the area around the geometric point of reflection. A common approximation is that the reflection is *complete* if the reflecting area contains the entire first Fresnel zone. The Fresnel zone for reflection is obtained by finding the intersection between the ground and the Fresnel ellipsoid defined by the receiver and the transmitter mirror image

below the ground surface[10]. Figure 6 illustrates the resulting first Fresnel reflection zone. T is the transmitter point, R is the receiver point and I is the geometric point of reflection.

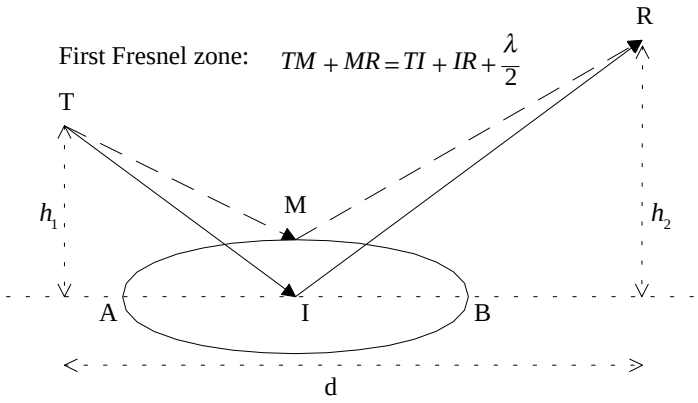

Figure 6. First Fresnel zone. Taken from [Boithias87]

Unless the angle of incidence is close to 0°, the Fresnel zone will have an elongated shape, the long axis being in the direction AB in the figure. The long axis will have the length

$$L_{long} = AB = d\frac{\sqrt{1+\frac{4h_1h_2}{\lambda d}}}{1+\frac{(h_1+h_2)^2}{\lambda d}} \qquad \textit{(eq. 17)}$$

and the short axis the length

$$L_{short} = \sqrt{\sqrt{d^2+(h_1+h_2)^2}\cdot\lambda} \qquad \textit{(eq. 18)}$$

For instance, for $f = 2GHz$, $d = 200m$ and $h_1 = h_2 = 50m$; $L_{long} = 10{,}9m$ and $L_{short} = 5{,}8m$.

As will be discussed in the next section, not only the size, but also the roughness of the surface will determine the characteristics of the reflected/scattered field.

Rough surfaces, diffuse reflections

When the irregularities of the reflecting surface can no longer be regarded small compared to the wavelength, the reflection will not be specular. There will still be a maximum in the geometric direction of reflection, but there will also be radiation in other directions, increasing with roughness. The most common way of describing the scattering in this case is by a

[10] The Fresnel ellipsoid is defined as the set of points from which the sum of the distance to transmitter and receiver exceeds the Tx-Rx shortest distance by λ/2.

statistical description using the bistatic radar cross-section of the surface. Existing theories and methods to estimate the scattering from rough surfaces is described in some detail in Chapter 4. Below the geometry of the scattering problem as well as the definitions of the radar cross-section is given.

The terminology used by Ulaby and Dobson in [Ulaby89] and others has been selected in this study to describe the scattering geometry. This is illustrated in Figure 7. The axes are defined so that the plane that describes the average scattering surface is the x-y-plane. The incident wave is assumed to be plane; the x-axis is then defined as the line that is the intersection between the wavefront and the (average) surface. θ_i and θ_S are the incident and scattering elevation angles, respectively, defined relative to the z-axis as shown. Similarly, ϕ_i and ϕ_S indicate the azimuth angles, defined in the x-y-plane counter-clockwise relative to the x-axis. $\hat{v}$ and $\hat{h}$ are the unit vertical and horizontal polarisation vectors and $\hat{k}$ is the unit propagation vector. The directions of the propagation vectors follow the definition given by the *forward scatter alignment*.

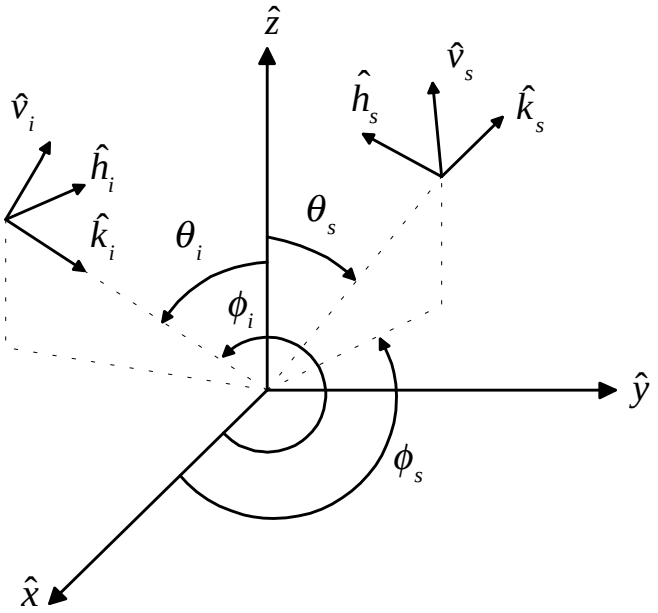

Figure 7. Scattering geometry, taken from [Ulaby89].

In radar terms the applicable theory is referred to as *bistatic scattering from a distributed target*. The radar equation for an object is defined as the ratio of received to transmitted power by

$$\frac{P_r}{P_t} = \frac{g_t(\theta_i,\phi_i)g_r(\theta_s,\phi_s)\lambda^2}{(4\pi)^3 {R_t}^2 {R_r}^2}\cdot\sigma \qquad \textit{(eq. 19)}$$

where g_t and g_r are the antenna gains in the incidence and scattered directions, respectively, R_t and R_r [m] are the distance from the scatterer to the transmitter and receiver, respectively, and σ [m^2] is the bistatic radar cross-section, which is used in this study to determine the scattering characteristics of natural surfaces. The bistatic radar cross-section is dependent on polarisation and is defined as

$$\sigma_{\alpha\beta} = \lim_{R\to\infty}\left(4\pi R^2 \frac{S_\beta^s}{S_\alpha^i}\right) \qquad \textit{(eq. 20)}$$

where S_α^i is the power density of the incident wave and S_β^s is the power density of the scattered wave at a distance R from the scatterer. α and β denote the polarisation (*v* or *h*) of the scattered and incident waves, respectively. For a complete description, the cross-section must therefore be given as σ_{vv}, σ_{vh}, σ_{hv} and σ_{hh}. In general $\sigma_{\alpha\beta}$ is dependant on the incident and scattering directions as

$$\sigma_{\alpha\beta} = \sigma_{\alpha\beta}(\theta_i, \theta_s, \phi_i, \phi_s) \qquad \textit{(eq. 21)}$$

Assuming isotropic surfaces, as done in this study, the radar cross section is dependent only on the difference in azimuth angles, $\Delta\phi$. For a distributed target, like a natural surface, the radar equation extends to an integral over the illuminated area,

$$P_r = \iint_A \frac{P_t g_t(\theta_i,\phi_i) g_r(\theta_s,\phi_s)\lambda^2}{(4\pi)^3 {R_t}^2 {R_r}^2} \cdot \sigma^0 \cdot dA \qquad \textit{(eq. 22)}$$

where σ^0 is the *bistatic scattering cross-section* $\sigma_{\alpha\beta}$ *per unit area*. In this report it will be assumed that the target has uniform properties[11] across the area. Estimation of the radar coefficient can be done by measurements of P_r for different angles. As eq. 22 shows, this leads to the solution of an integral equation. The solution to this equation based on measurements is discussed in Chapter 5.

2.2.3 Diffraction

The theory of diffraction must be used when the assumptions from geometrical optics (GO) are no longer valid. Diffraction is important in channel modeling to explain the apparent "bending" of waves, leading to signal components extending into shadow regions. One often used technique to estimate diffraction is *Uniform Theory of Diffraction* (UTD). UTD is an extension of the earlier *Geometrical Theory of Diffraction* (GTD) first suggested by Keller in 1962 [Keller62]. These are high-frequency techniques that allow the estimation of diffraction off objects that are considerable larger than the wavelength (e.g. [Balanis89]).

It is a formidable task to calculate the diffracted field from an obstruction of arbitrary shape and electrical properties. However, analytical solutions exist for a limited number of cases, like conducting wedges or cylinders. The theory will then provide a diffraction coefficient, much like the reflection coefficients in Subsection 2.2.2. The wave will appear to arrive as a ray from the edge of the obstruction (see Figure 8). A real case can often be approximated as a

[11] This is eqivalent to assuming the surface to being *statistically uniform*, meaning that both the height distribution function and the distribution of the electro-magnetic properties are uniform over the area. This is discussed further in chapter 4.

combination of such cases, and the total field can be found by superposition. Figure 8 shows the case of diffraction over a knife-edge shaped obstruction, infinitely long and with infinite conductivity [Boithias87]. Solutions also exist for diffractions from other geometries, e.g. conducting cylinders.

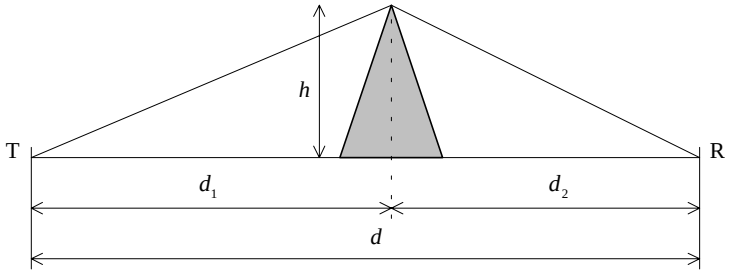

Figure 8. Knife-edge diffraction. Taken from [Parsons92].

The electric field strength E relative to free space (E_0) in the case of knife edge diffraction is given by

$$\frac{E}{E_0} = \frac{1}{1+j}\int_{v}^{\infty} e^{j\pi\frac{t^2}{2}}\,dt \qquad \textit{(eq. 23)}$$

where *v*, which is referred to as the *Fresnel-Kirchoff diffraction parameter* [Parsons92], is defined as

$$v = h\sqrt{\frac{2}{\lambda}\cdot\frac{d_1 d_2}{d}} \qquad \textit{(eq. 24)}$$

For *h=0*, i.e. when the transmitter and receiver are aligned with the top of the knife-edge, the power ($|E|^2$) is 6 dB lower than for free space.

2.2.4 Polarisation spread, depolarisation

Each of the *L* signal components in eq. 2, 3, 4 will have a direction of polarisation. Even though all the components originate from the same source (the transmitted signal), they will in general have different polarisation[12]. This is because scattering and reflections lead to a change in polarisation, which is called *depolarisation*. Linearly polarised signals will change direction,

[12] This means that signals received in orthogonal directions, e.g. vertical and horizontal, will fade independently. This is sometimes exploited in mobile communications by using two receiver antennas with dual polarisation.

and circularly polarised signals will become elliptic[13]. This means that in addition to the antenna gain in the direction from which the component arrives and the field strength, the value of the received component is depending on the difference in polarisation between the signal component and the receiving antenna. The loss due to this polarisation mismatch is called *polarisation loss*.

In the cases of rough surfaces, a purely horizontally polarised field will have a reflected vertical component (and vice versa). For random rough surfaces, the statistics of the surface determine the degree of depolarisation.

Formally any wave can by characterised by its complex *polarisation factor p*, defined as

$$p = \frac{E_v}{E_h} \qquad \textit{(eq. 25)}$$

where E_v and E_h are the complex amplitude of the vertical and horizontal electric field respectively [Beckman87]. For instance; for a linearly polarised wave we have $\mathrm{Im}(p) = 0$, for a right-handed circularly polarised wave we have $p = j$.

The *depolarisation factor q* in a reflection is defines as

$$q = \frac{p_R}{p_I} \qquad \textit{(eq. 26)}$$

where p_R and p_I are the polarisation factors of the reflected and incidence waves. Note that for a perfectly conducting smooth surface $q = \frac{E_{vR}/E_{vI}}{E_{hR}/E_{hI}} = \frac{1}{-1} = -1$.

For rough surfaces *q* results from the solution of the integral equation eq. 22. This is discussed further in Chapter 4.

2.2.5 Other propagation mechanisms

A number of other propagation mechanisms will also be present in the mobile radio channel, but are not described in any detail in this chapter as they are considered of minor importance with respect to inclusion into radio channel propagation models for mobile communications.

- *Doppler effects*: Doppler shifts due to mobiles moving at high speed can be an important issue in mobile systems, especially at higher frequencies. However, this is an item to be considered principally in system design and normally plays no role in radio channel propagation prediction for radio planning.
- *Gas absorption:* Up to 2 GHz gas absorption is less than approx. 0.01 dB/km [Boithias87]. From X-band (6.8 – 12.6 GHz) gas absorption should be taken into account, it is especially important around 60 GHz, where a peak in the atmospheric attenuation is found due to oxygenic absorption.

[13] In mobile communications, the polarisation will almost exclusively be linear.

- *Rain attenuation:* Much like gas absorption, rain attenuation can be considered unimportant at frequencies up to “a few GHz”. Since mobile systems at higher frequencies are normally very short range, rain attenuation is not considered.
- *Atmospheric refraction:* The bending of rays in the atmosphere due to the vertical gradient of the refractive index is well known [Boithias87]. This effect is important in radio relay and satellite systems, but is normally ignored in terrestrial mobile systems due to the shorter links and less dependency on a direct link.

3 Analysis of channel models for mobile communications

This chapter provides an overview and analysis of existing radio channel models used in terrestrial mobile communications. As discussed in Chapter 1 a mathematical description of the radio channel resembling reality is necessary both for radio planning purposes and for system design. Focus will be on models for rural, macrocellular environments, as coverage for 3G systems will be a key issue. The overview should not be considered as comprehensive, but will contain the most commonly types of models used in the environments in question.

Radio propagation models can be grouped into *deterministic* and *statistical* channel models. Most often a deterministic model will be used for radio planing in a specific area, while a statistical model is typically most useful for system design or initial coverage consideration. A further classification will be performed with respect to *narrowband* and *wideband* channel models. The output provided by the models will differ according to the special characteristics of each radio system and the type of mechanisms one wants to study.

The first section in this chapter will establish some parameters that are used later, and also define the concept of fading. The second section gives an overview of narrowband models, and the third section describes wideband models. The last section provides an analysis based on the requirements identified in Chapter 1. Overviews of radio channel prediction models can be found in e.g. [Bertoni94] and [COST231_98].

3.1 Introduction

This section gives an overview of some of the terms and parameters used in the channel models, and should be regarded as a reference for the rest of the chapter.

3.1.1 The concept of fading

Fading in mobile radio channels is the effect of variations of the received signal level when a terminal is moving. In mobile radio the received signal will, due to multipath propagation, consist of a number of reflected or diffracted replicas of the transmitted signal as described in Chapter 2. The total received signal level will be decided by addition of these components in amplitude and phase. When the terminal moves more than a fraction of a carrier wavelength the phase of the multipath components will change and the received signal level would therefore fluctuate rapidly. This effect is called *short-term fading*[14] [Lee82]. The large-scale effect of variations in the *average* signal level due to terrain variations is called *long-term fading*[15]. Because the long-term fading is due to buildings or terrain obstacles present in the area between the transmitter and receiver, it is often referred to as *shadow fading*. The total fading is made up of a combination of these two effects, as illustrated in Figure 9.

Normally, channel models do not attempt to estimate the level of the short-term fading for a specific position. The exception is real-time methods to estimate future fade levels based on past levels used to improve the performance in systems using adaptive transmission techniques (e.g. [Duel-Hallen00]).

[14] The *short-term fading* is often assumed to be Rayleigh-distributed or Rice-distributed.

[15] The *long-term fading* is often assumed to be lognormally distributed.

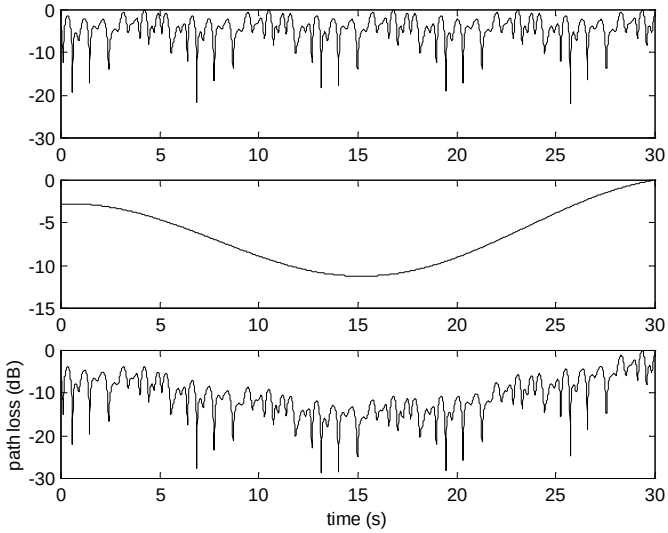

Figure 9. Example of short-term (top), long-term (middle) and total fading (bottom). Short-term fading is in this case modelled as Rayleigh distributed, long-term fading is modelled as lognormally distributed. Example for 2 GHz, approximately 0.15 m/s, all values relative to max. [dB].

3.1.2 Narrowband and wideband channels

Because the multipath components propagate different distances to the receiver, multipath propagation introduces time dispersion. When the time dispersion is small compared to the symbol length of the (digital) communications system, the channel is referred to as *narrowband*. This also means that the channel response in the frequency domain is constant over the system bandwidth. Therefore this type of channel is also referred to as a *flat fading* channel. When the time dispersion is significant compared to the symbol length, the channel is called *wideband*. This means that the channel response in the frequency domain is no longer constant over the system bandwidth. This is also referred to as a *frequency-selective fading* channel. Note that the same channel can be narrowband for one system and wideband for another. The bandwidth for which the channel response in the frequency domain can be assumed constant is called the *coherence bandwidth*. The coherence bandwidth is often defined as the necessary frequency change to make the correlation between two monochromatic signal components 0.5 [Løvnes91]. The concept of *narrowband* and *wideband* channels is illustrated in Figure 10.

GSM has a radio bandwidth of approximately 200 kHz, which means that it must be considered wideband in large time dispersion cases, like mountainous areas or in urban macrocells. For small cells GSM can normally be considered narrowband. UMTS, using a CDMA (Code Division Multiple Access) spread spectrum technique, has a much larger radio bandwidth of approximately 5 MHz and must therefore be assumed to be wideband for almost all mobile channels. This is one of the reasons why wideband models are preferred in future network-planning tools. The radio bandwidth also affects the fading, because a larger bandwidth will average out the fast fading, leading to smaller signal level fluctuations.

URN:NBN:no-1290

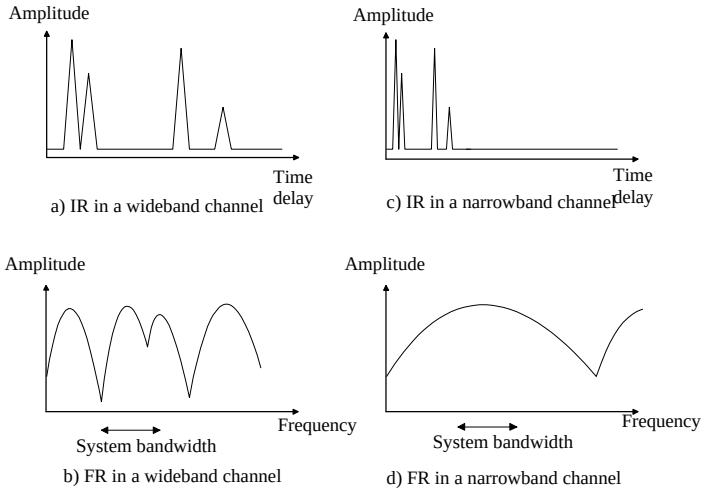

Figure 10. Narrowband and wideband channels. a) and b) show the impulse response (IR) and frequency domain channel response (FR) respectively for a wideband channel. c) and d) show the impulse response and frequency domain channel response respectively for a narrowband channel. Note that the system bandwidth is the same in the two cases.

3.1.3 The delay-azimuth-Doppler spread function

As explained in Chapter 2 the mobile radio channel will cause dispersion in both space and time delay and also a Doppler shift of the frequency. By ignoring the elevation angle of the received signal[16] and assuming a finite number (L) of impinging waves, the channel impulse response (transfer) function can be written as

$$h(\tau,\phi,\nu) = \sum_{l=1}^{L} \alpha_l \delta(\tau-\tau_l)\delta(\phi-\phi_l)\delta(\nu-\nu_l) \qquad \textit{(eq. 27)}$$

where α_l, τ_l, ϕ_l and ν_l are the complex amplitude, the relative propagation delay, incidence azimuth angle and Doppler frequency of the *l*th wave, respectively [Pedersen98]. This function is called the *delay-azimuth-Doppler spread function*[17].

The *power delay profile* $Q(\tau)$ is defined as

$$Q(\tau) = \iint \left\langle \left| h(\tau,\phi,\nu) \right|^2 \right\rangle d\phi d\nu \qquad \textit{(eq. 28)}$$

[16] Ignoring the elevation angle variation is a justifiable assumption for outdoor terrestrial mobile radio channels due to the variation normally being less than the antenna beamwidth.

[17] Integrating this function over the entire azimuth and Doppler range gives the familier complex impulse response (CIR) function in just the temporal domain, $h(\tau)$.

where <…> denotes the local average to remove short-term fading[18].

The *delay spread (DS)* parameter is the second order moment of the *power delay profile*. *DS* is defined as

$$DS = \sqrt{\frac{\int (\tau - m)^2 \cdot Q(\tau) d\tau}{\int Q(\tau) d\tau}} \qquad \textit{(eq. 29)}$$

where *m* is the mean delay defined as

$$m = \frac{\int \tau \cdot Q(\tau) d\tau}{\int Q(\tau) d\tau} \qquad \textit{(eq. 30)}$$

The *power azimuth spectrum* is given by

$$P(\phi) = \iint \left\langle \left| h(\tau, \phi, \nu) \right|^2 \right\rangle d\tau d\nu \qquad \textit{(eq. 31)}$$

The *azimuth spread (AS)* parameter is defined in exactly the same way as the *delay spread.* It is the second order moment of the *power azimuth spectrum* and is defined as

$$AS = \sqrt{\frac{\int (\tau - \psi)^2 \cdot P(\phi) d\tau}{\int P(\phi) d\tau}} \qquad \textit{(eq. 32)}$$

where ψ is the mean azimuth angle given by

$$\psi = \frac{\int \tau \cdot P(\phi) d\tau}{\int P(\phi) d\tau} \qquad \textit{(eq. 33)}$$

The *AS* and *DS* are often used as parameters to characterize the dispersion in the channel, in the angular and temporal domains, respectively.

The *Doppler spectrum* D(ν) can be derived in the same manner as the *power delay profile* and the *power azimuth spectrum.* In a manner similar to the delay spread above, the *Doppler spread* can be defined. The *scattering function*, which is a three dimensional function often used to describe the variations in both time delay and Doppler frequency domains can be derived from [Pahlavan95]

$$S(\tau, \nu) = \int \left\langle \left| h(\tau, \phi, \nu) \right|^2 \right\rangle d\phi \qquad \textit{(eq. 34)}$$

[18] Averaging over approximately 20-50 λ is recommended for measurements [Parsons92]

3.2 Narrowband channel models

Narrowband channel models are only concerned with the *received signal level*, or rather the *path loss* on the link, most often defined as the difference between transmitted and received signal level when isotropic antennas are used [COST207_88]. In this section, when nothing else is mentioned, the model provides the average values, the fading has to be taken into account by additional assumptions.

3.2.1 Statistical models

A large number of statistical narrowband models exist and are being used. These models are empirical descriptions of the radio wave propagation based on measurements. It is common to use *correction factors* to improve accuracy somewhat for different types of scenarios, for instance can street width, building height etc. be used as input data for the models to improve the performance. This means that the distinction between the statistical and the deterministic methods can sometimes become blurred. This subsection gives an overview of commonly used statistical models.

Okumura-Hata (O-H)

Okumura's formulation was based on a large number of measurements made in the area around Tokyo, Japan. The original description was simply a number of curves fitted to the data [Okumura68]. Several authors have provided equations that are curve fittings to Okumura's original description. The best known mathematical approximations are by Hata [Hata80]. The Okumura-Hata model is valid in the range 100 MHz to 1.5 GHz, but has been extended up to frequencies in the range 1.5-2 GHz by COST 231 [COST231_98]. The path loss L_b is given by

$$L_b[dB] = 46.3 + 33.9 \cdot \log f[MHz] - 13.82 \log h_{base}[m] - a(h_{mobile}[m]) + (44.9 - 6.55 \log h_{base}[m]) \log R[km] + C_m \qquad \textit{(eq. 35)}$$

where h_{base} and h_{mobile} is the height above local ground for the base station and the mobile station, respectively. The factor $a(h_{mobile})$ is defined as

$$a(h_{mobile}) = (1.1 \cdot \log f[MHz] - 0.7) h_{mobile}[m] - (1.56 \cdot \log f[MHz] - 0.8) \qquad \textit{(eq. 36)}$$

The correction factor C_m is *0 dB for medium sized cities and suburban centres with medium tree density* and *3 dB for metropolitan centres*. The model is applicable for Tx-Rx-distances larger than approximately 1 km. A number of additional correction factors has been suggested, for instance to account for vegetation (e.g. [Leppänen92]).

The Okumura-Hata model is still extensively used, even for radio planning purposes. This is due to its simplicity and the fact that detailed DEMs are not always available.

Walfisch-Ikegami (W-I)

The Walfisch-Ikegami model ([Walfisch88], [Ikegami84], [COST231_98]) is a model for use in *urban environments*. Compared to Okumura-Hata this model takes a larger number of correction factors into account, for instance *house spacing* and *street orientation*. The full description of this model can be found in e.g. [COST231_98].

Like Okumura-Hata this model is often used, sometimes in combination with the O-H model, as W-I can be used also for microcells.

Neural network methods

Methods which base the prediction on neural network training have been suggested, e.g. by Stocker et.al. in [Stocker92] and [Stocker93]. The training can be done by either theoretical methods or by measurements. The advantage of the method is the possibility to derive training patterns directly from measurements. The system will become very flexible, and will be able to adapt to any environment by providing measurements. The training is time consuming, but once the network is trained, the results are obtained immediately [COST231_98].

There are some disadvantages to these techniques. The models are not physically based; therefore they give no physical inside into propagation. Also the performance of the model may be very specific to the area in which the measurements were performed. In addition the structure of the neural network, e.g. the number of hidden nodes might determine results.

Modeling of the fading

As mentioned in the introduction to this section, most of the statistical narrowband models only provide prediction of the average signal level and therefore do not consider fading. If fading and temporal signal variations are to be taken into account, an extension of existing models is needed. A common assumption is that of *wide-sense stationary uncorrelated scatterers* (WSSUS) (e.g. [Pahlavan95]) which means that signal variations on paths arriving at different delays are uncorrelated, and that the correlation properties of the channel are stationary. The latter assumption allows the modeling of fading as a stationary process. A distribution for the fading process must be assumed, for instance Rayleigh fading in the short-term and lognormal fading in the long-term. In addition an autocorrelation function must be assumed, or equivalently its power density spectrum, which is equivalent to the Doppler Spectrum (see Subsection 3.1.3) of the channel.

The short-term fading:

One very simple and therefore popular model for the short-term fading is the one suggested by Clarke [Clarke68]. This model assumes all the multipath signal components to have equal amplitude. It is further assumed that the components arrive in the horizontal plane with a uniformly distributed arrival angle and that the phase is uniformly distributed over 0 to 2π. This leads the received signal level to be Rayleigh-distributed and the Doppler spectrum $D(\nu)$ to be of the form

$$D(\nu) = \frac{1}{2\pi\nu_m} \cdot \left[1 - (\frac{\nu}{\nu_m})^2\right]^{-1/2} \qquad (eq.\ 37)$$

where ν_m is the maximum Doppler frequency given by

$$\nu_m = \frac{v}{\lambda} \qquad (eq.\ 38)$$

and where v is the speed of the mobile. This Doppler spectrum shape is often called a *classical spectrum*.

If a direct, specular component exists in addition to the scattered ones, the signal level distribution will be Rician instead of Rayleigh, and the Doppler spectrum will have an impulse at the frequency corresponding to the direction towards the base station. This Doppler spectrum is called *Rician*.

Other models for the short-term fading include for instance the *flat Doppler spectrum*, which is applicable in indoor environments [Parsons92], or a *Gaussian Doppler spectrum* [Løvnes92].

The long-term fading:

If the model only provides a wide area average, the long-term fading as well as the short-term fading must be modelled by an additional model. A possible way to model the long-term fading is by the use of a Markov model. In this case it is assumed that the fading process can be modelled as being stationary only within certain *states*, for instance corresponding to *line-of-sight*, *non-line-of-sight* and *obstructed line-of sight.* A Markov process can describe the switching from one state to another [Bråten98], such that the overall process becomes non-stationary.

Sørensen [Sørensen98] has suggested modeling the long-term fading as an ARMA (autoregressive moving average) process (e.g. [Janacek93]). An often-used model was suggested by Gudmundson [Gudmundson91] and is based on the correlation function of the long-tern fading process to be of the form

$$R(k) = const \cdot a^{|k|} \qquad (eq.\ 39)$$

where the correlation coefficient *a* is area dependant and the distance between two points is given by *k*.

Other models

A large number of other models than the ones mentioned in this subsection has been suggested and used. These include for instance models by *Xia and Bertoni* ([Xia92]), which is a model for urban environments that takes a large number of correction factors into account and therefore sometimes is used in radio planning tools. *Ibraham and Parsons* [COST207_89] have suggested a very simple model based on a large number of measurements in central London. The model uses a *distance power law*[19] and uses correction factors based on the degree of urbanisation.

3.2.2 Deterministic models

All methods described in this subsection are based on using a two dimensional terrain description of the terrain profile between the transmitter and receiver. The models provide accurate or approximate solutions to the propagation equations in two dimensions in the vertical plane. These methods are all considered narrowband because the time dispersion due to vertical plane variations normally are small.

Three-dimensional methods or two-dimensional methods in the horizontal plane are considered wideband and are all mentioned in Subsection 3.3.2 even though they often are developed to provide path loss solutions only.

[19] A *distance power law* means that the path loss is assumed to be proportional to a term R^{α} where R is the Tx-Rx-distance and α is normally in the range 2 (free space) to 5.

Common for all the methods described in this subsection is that since they ignore the contributions by obstacles outside the vertical Tx-Rx-plane the performance is strongly area dependant, and the accuracy is limited in e.g. heavily built-up or mountainous areas.

Models based on *Uniform theory of diffraction* (UTD)

One model using UTD was suggested by Lebherz et.al. [Lebherz92]. In this model the terrain obstacles are first replaced with simple geometrical objects (Figure 11 a)). Then N main obstacles (MOs) are identified and the profile is divided into N profile sections. The main obstacles are obstacles that directly obstruct the line-of-sight between other MOs. Between MOs secondary obstacles (SO) may exist which cause minor diffraction or scattering (Figure 11 b)). Specular ground reflections between MOs are considered SOs.

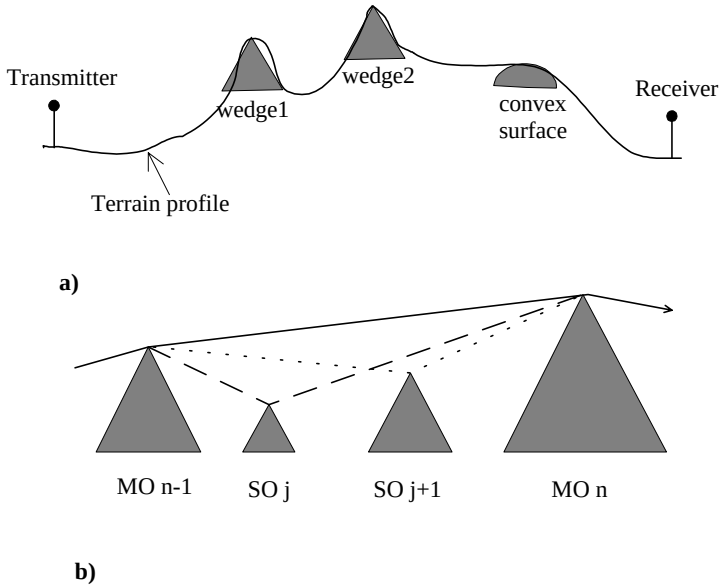

Figure 11. The UTD model. a) The terrain obstacles are replaced by wedges and convex surfaces, for which UTD solutions exist. b) Illustration of one of the N profile sections. Two SOs are present between the MOs. Taken from [Lebherz92].

The model uses an effective recursive matrix notation to calculate the total field, consisting of contributions from all the relevant rays, including both the main diffracted and secondary diffracted components. Mutual interaction between the SOs is ignored.

Models based on Parabolic Equations (PE)

The parabolic equation is an approximation of the wave equation. The starting point of PE is the scalar Helmholtz wave equation, written as

$$\nabla^2\psi + k^2 n^2 \psi = 0 \qquad (eq.\ 40)$$

where *k* is the propagation constant and *n* is the refractive index. The parabolic differential equation approximation to this equation in the two dimensions range x and height z (ignoring the variations in the y-direction) can be written as [Craig96]

$$\frac{\partial^2 u}{\partial z^2} + 2jk\frac{\partial u}{\partial x} + k^2(n^2(x,z) + 2z/a - 1)u = 0 \qquad (eq.\ 41)$$

where u is the *amplitude function* where the fast phase variations are removed from ψ and a is the world radius of curvature. This equation is normally solved by some kind of *split-step algorithm*, which means that the solution is produced by marching along the x-direction and solving a vertical stripe $u(x+\Delta x, z)$ in an iterative manner based on $u(x, z)$. This means that *back-scattering* is disregarded. The boundary conditions at the earth, which need to be taken into account, are dependent on whether the polarisation is vertical or horizontal.

The first solution based on PE was by Hufford in his master thesis from 1948 [Hufford48]. A recent model based on two-dimensional PE has been suggested by Janaswamy and Andersen [Janaswamy98]. The model takes into account both lossy (finite conductivity) and lossless ground. Buildings can be superimposed onto the terrain profile and can have different electrical properties from the ground. A similar method where the terrain is approximated by absorbing half-screens is described in [Berg94]. Also in [Geng95] a PE modeling approach is described, showing excellent closeness to fit with experiments in rural areas.

In addition to these models being 2D, the most obvious disadvantage is the fact that back-scattering is ignored. This may not represent a large error on uplink, since the base station antennas are normally strongly directional, but may be a significant source of error on downlink.

Models based on Integral Equations (IE)

Following the IE approach, the field at a scattering surface is written in the form of an integral equation where the unknown field-strength (either electric- or magnetic-) is given by an integral where the current density on the surface is part of the integrand. The current density is then written as a series of basis functions with unknown coefficients. By satisfying the boundary conditions on the surface, where the field-strength is known, the unknown current density can be found using numerical methods, for instance (and most commonly) by the *method of moments* [Balanis89].

The *Electric-field-integral-equation* (EFIE) uses the boundary condition on a *perfectly electric conducting* (PEC) surface for the electric field. This formulation takes on a particularly simple form in the case of a horizontally polarised incident wave. The *Magnetic-field-integral-equation* (MFIE) solves the boundary condition for the magnetic field on any point on the surface. This formulation takes on its simplest form in the case of vertically polarised incident field. If the surface is neither perfectly magnetically nor electrically conducting, both the EFIE and MFIE are needed for a complete description, the equations will then be coupled.

Hviid et.al. [Hviid95] describe a method based on MFIE. The model assumes a smooth surface, which means that there must be no rapid variations within the integration step. It is also assumed that the terrain is 2D with no transversal variations and that there is no back-scattering. Under these assumptions the model is exact. The model is very slow, but is often used as a reference for other models. A model using EFIE has been developed at Trinity Collage, Dublin ([Moroney95], [Brennan98]). This model makes the same assumptions about the terrain as the previously mentioned model, but is computationally much more efficient.

IE methods do in general show good performance, the most obvious disadvantage being the complexity, which can become high for high detail terrain profiles.

Other models

There exist a number of other models and variations of the ones mentioned previously. For instance there are models based on the two-dimensional *finite-difference time-domain* (FDTD) in the vertical plane (e.g. [Pahlavan95]). FDTD in the horizontal plane would be considered wideband, as described in the introduction to this subsection. There are also a number of well-known methods that solve the problem of diffraction over multiple knife-edges. An overview of these is given by Parsons in [Parsons92] and includes models by *Vogler* [Vogler82], *Epstein-Peterson* [Epstein53], *Bullington* [Bullington47] and *Deygout* [Deygout66].

3.2.3 Semi-deterministic models

In addition to the statistical and deterministic models described previously, hybrid models exist which combine aspects of the two classes. In one of them Hata's statistical model is combined with a multiple knife-edge diffraction model [Badsberg95].

3.3 Wideband channel models

Wideband channel models describe the *time dispersion* on the link. Certain models also describe the *direction-of-arrival* and the *Doppler spectrum*. Most of the *statistical* wideband channel models are only concerned with the relative dispersion. An additional model (e.g. Okumura-Hata, Walfisch-Ikegami) is needed to estimate the path loss.

Also, as discussed in the following subsection, some statistical models take the directional or even Doppler domains into account. For the time being statistical model cannot take polarisation into account.

3.3.1 Statistical models

In the statistical models, generally the WSSUS assumption (see Subsection 3.2.1) is used, which means that the *scattering function* in the time delay and Doppler frequency domains can be written as

$$S(\tau,\nu) = Q(\tau) \cdot D(\nu) \qquad (eq.\ 42)$$

where Q(τ) is the *power delay profile* and D(ν) is the *Doppler spectrum* [Pahlavan95].

The GSM recommended model

A rather simple model was suggested by COST207 [COST207_89] and was adopted as test channels in the GSM specifications [GSM91]. This model is based on extensive wideband measurements performed in many European countries.

The model uses tapped-delay-lines, which means that the power delay profile is described by a number of discrete taps, which are specified by *relative arrival delay* and *average relative power*. Each tap is also allocated a Doppler spectrum to account for the fading. Models for *rural area*, *typical urban*, *bad urban* and *hilly terrain* are provided. The full details of the GSM models can be found e.g. in [GSM91].

The JTC recommended model for DCS

The American Joint Technical Committee (JTC) has suggested a model for use in PCS (Personal Communications Services). The structure of this model is the same as the GSM models, but it is somewhat more elaborate. There are models for *indoor office*, *indoor residential* and *indoor commercial* areas. For outdoor there are profiles for *urban high-rise*, *urban/suburban low-rise* and *outdoor residential*. For the outdoor environments there are models for both *high* and *low antenna*. The model is fully described for instance in [Pahlavan95].

Frequency domain models, AR modeling

The statistical wideband models mentioned up to now are all time domain models. The channel response can also be modelled in the frequency domain. In [Pahlavan95] a model based on autoregressive (AR)-modeling is described.

Models including *direction-of-arrival (DoA)*

Prediction of the performance of *smart antenna* and *MIMO* systems requires the knowledge of the channel response also in the directional domain. As systems with smart antennas are still under development, channel models including DoA rarely exist. It is however expected that 3rd generation systems will make use of smart antennas, thus requiring advanced directional channel models.

TUV Geometrical model:

Fuhl and Molisch [Fuhl98] at the Technical University of Vienna (TUV) have developed a model that is geometrically based. That means that the channel response is generated based on assumptions about the geometrical position of the scatterers. The complex impulse response (CIR) in *time delay* (τ), *absolute time* (t) and *azimuth angle* (ϕ) at the base station can according to the model be written as

$$h(\tau,t,\phi) = h_{LOS}(\tau,t,\phi) + h_{local}(\tau,t,\phi) + h_{\text{distant}}(\tau,t,\phi) + h_{BS}(\tau,t,\phi) \qquad (eq.\ 43)$$

where h_{LOS} is a line-of-sight component, which may or may not exist. h_{local} consists of reflected components from scatterers in the vicinity of the mobile station, and h_{BS} of components due to scatterers close to the base station. These last components will only exist in cases when the base station is lower than the terrain surrounding it. $h_{distant}$ is due to reflections from scatterers away from both the MS and BS, which can be for instance mountains or very large building structures. The positioning of the scatterers is illustrated in Figure 12. The model defines the scattering areas, the distribution of the scatterers within each scattering area as well as the bistatic radar cross-section of the individual scatterers.

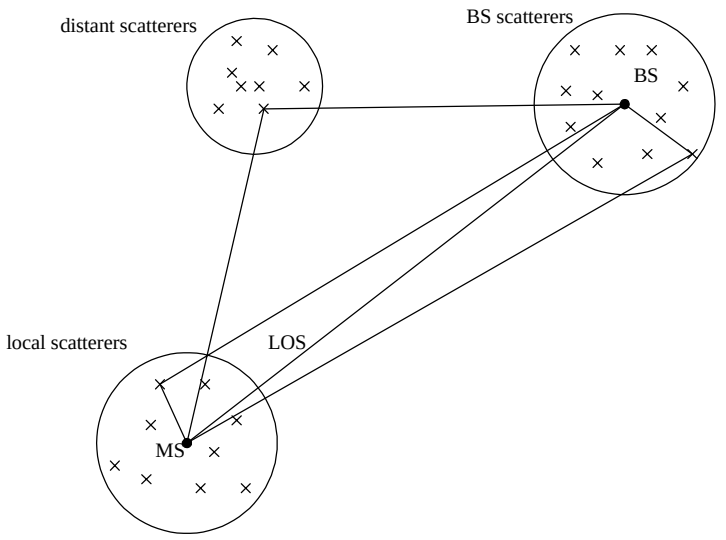

Figure 12. Illustration of the geometry for the TUVl model, the areas in which the scatterers are positioned are divided into local, distant and BS areas

The full details of the model, including assumptions about the number of, and the distribution of, the scatterers, the size of the scattering areas, and the distribution of the scattering power is given in [Fuhl99] for picocells, microcells and macrocells. In a later extension of this model [Molisch99], the probability density function of the scatterers is uniform throughout the whole cell area, but the cross-section of the scatterers is different and may change with time.

Other models

Other tapped-delay-line models than the ones mentioned in this subsection have been suggested. A somewhat more elaborate model was developed by the RACE CODIT project [CODIT95]. The model differs between 15 different types of environments, ranging from picocells to macrocells. The *number of taps*, *time delays of each tap* and *fading* are all decided by statistical distributions rather than fixed values.

A model including DoA has been suggested by Nørklit and Bach Andersen [Nørklit98]. Like the *geometrical model*, this model is also motivated from the geometry of the channel, but assumes a slightly different geometry and is 3 dimensional to be able to account for differences in antenna height at the transmitter and receiver.

A stochastic directional channel model is suggested by Pedersen et.al. in [Pedersen00]. It describes the power azimuth spectrum as being Laplacian distributed and the power delay profile as being gaussian distributed. A 3D stochastic model for indoor channels is described in [Zwick00]. The model takes the Doppler spectrum inherently into account, and can be extended to include outdoor urban areas.

A new approach has been suggested by Franceschetti et.al. in [Francechetti99]. The model assumes optical-ray propagation across a medium of disordered lossless scatterers. The medium is composed of sites organised in a regular two-dimensional lattice. Each site can

either be occupied by a lossless square object or not. Propagation is modelled as a random walk through the lattice.

3.3.2 Deterministic models

The deterministic methods mentioned in this subsection are 3D, or 2D models taking propagation only in the horizontal plane through Tx and Rx into account. As previously explained in Subsection 3.2.2, 2D models taking propagation only in the vertical plane through Tx and Rx into account are assumed to be narrowband, due to the limited time dispersion introduced.

Ray-tracing

When the obstacles in the channel are large compared to the wavelength and when *specular reflections* and *refraction* are the dominant propagation mechanisms, like in indoor environments or regular outdoor urban environments, the propagation can be well estimated by using the theory of *geometrical optics (GO)* and approximating all obstacles to be electro-magnetically large, smooth polygons. This lead to the development of a class of prediction methods called *ray-tracing* [Pahlavan95]. In ray-tracing, all the paths (or *rays*) connecting the transmitter and receiver through multiple reflection, refraction and direct free space propagation are identified. By adding all the significant components at the receiver, the total contribution can be found. Complex ray-tracing algorithms may also include diffraction and sometimes also diffuse scattering [Anderson96], [Kurner93]. In Figure 13 an example illustrating the concept is shown. An example of an implemented Ray-tracing tools is described in e.g. [Wagen94].

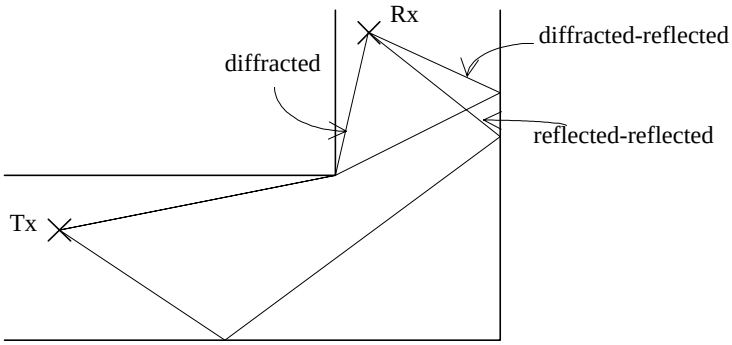

Figure 13. Ray-tracing, illustration of the propagation mechanisms.

There are two main types of ray-tracing algorithms, the *direct methods (or ray launching)* and the *inverse methods (*or *ray tracing)* [Cátedra98]. The direct methods, which include *pincushion* and *shooting-and-bouncing rays*, is based on 'launching' a number of ray tubes in all directions from the transmitter and follow them until they reach the receiver or are attenuated so much that they need not be considered. These methods can become cumbersome when diffraction is to be included, because each diffracting edge must be treated as a new launching source. The *inverse methods* take a somewhat different approach. Given the

geometry of the problem, the algorithm searches for the direct path, reflected paths, diffracted-reflected paths and so forth. For instance to search for (single) reflected paths the algorithm needs to find facets which can be seen without obstruction by both the transmitter and receiver. These algorithms are more complex than the *direct methods*, but are better suited to take diffractions into account. In [Gschwendtner95] the two approaches are compared in terms of performance and complexity.

To keep the complexity and computational requirements at a reasonable level, until recently most ray-tracing algorithms have been two-dimensional, taking into account propagation in the horizontal plane only. This means that floor and ceiling reflections have been ignored in indoor environments, and over-rooftop diffraction have been ignored in outdoor urban environments. However, at the cost of increased computational requirements, also 3D algorithms have been developed (e.g. [Rizk96], [Lee01]). It has been shown that the 3D methods can be considerably speeded up by assuming all the obstructing walls to be vertical [Liang98].

The ray-tracing assumption of surfaces being smooth and large (compared to the wavelength) is a limitation for the method. Discussions of using a more realistic approach to the reflection of walls is done in e.g. [Landron93] and [Anderson96]. Allowing diffuse scattering as well as specular reflection will provide a large increase in complexity.

3D radar models

The type of model referred to as 3D radar models uses bistatic radar theory to predict the channel. These models estimate the path loss in the vertical Tx-Rx plane and take off-axis scattering into account. The path loss is calculated using diffraction theories. Off-axis scattering is taken into account as contributions from surfaces seen by both the transmitter and receiver. Different methods for calculating the radar cross-section of these surfaces have been used, based on models describing the coherent reflection and diffuse scattering from natural surfaces. the models normally only allow first order reflection/scattering. The concept is illustrated in Figure 14. Implementations are described in e.g. [Lebherz92], [Lie97] and [Tameh97]. These models, along with others, are described and compared in more detail in Chapter 4.

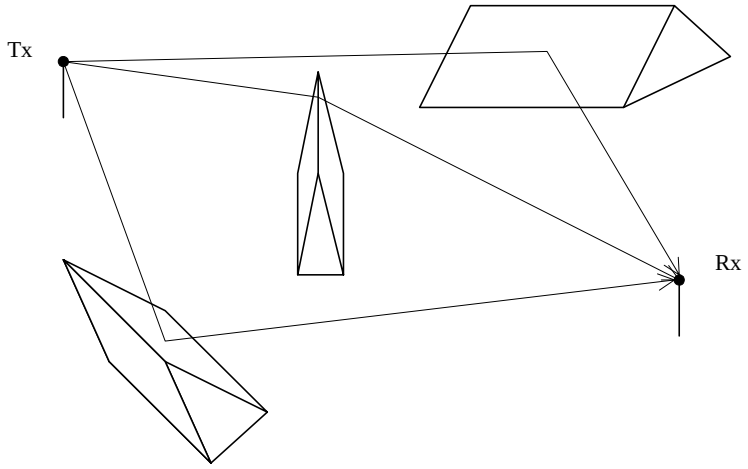

Figure 14. Illustration of models based on bistatic radar theory. First a 2D model in the vertical Tx-Rx-plane is found, then a 3D extension is found by identifying the significant off-axis scatterers.

Full wave solutions

There exist descriptions of a number of models that provide full-wave solutions of the Maxwell equations in 3D or 2D in the horizontal plane. These include an extension of the parabolic equation method described in Subsection 3.2.2 to 3D [Tjelta97]. A comprehensive description of PE techniques for electromagnetic wave propagation is given in [Levy00]. 3D FDTD methods have also been described [Pahlavan95].

The obvious disadvantage of these methods is the complexity when the Tx-Rx-distances become large. No implementations using 3D fullwave solutions intended for radio planning of terrestrial mobile communications have been encountered.

Other techniques

A model suggested by Ericsson [Berg95] applicable for microcellular urban environments is representative of a slightly alternative approach. The method assumes the over-rooftop diffraction to be unimportant, i.e. that the base station antenna is low. The prediction is made by predicting the propagation along street canyons. Propagation from one street into a crossing street is predicted by using empirical formulas. The path loss along streets is predicted using the dual slope behaviour observed for propagation in street canyons[20] [Xia93]. The model is

[20] It has been observed that in a street canyon, close to the base station the received signal follows a free space ($1/R^2$) law, whereas at one point the signal level versus distance curve experiences a change in slope, i.e. it starts to follow a $1/R^4$ law. The point where the slope changes is called the *breakpoint*. This breakpoint can be calculated from the frequency and the geometry by viewing the canyon as a waveguide and finding the point where the first Fresnel zone becomes blocked by buildings. In [Börjeson92] experimental work is done to identify the breakpoint.

computationally efficient as it uses a recursive method to calculate the path loss along an unlimited number of street canyons crossing each other.

3.4 Evaluation

The demands on the channel models will be different depending on whether the usage is *system design* or *radio planning*. The focus in the work described in this report is channel models for radio planning. However, channel models for system design will be discussed briefly in the first subsection of this section. The second subsection discusses channel models for radio planning.

When evaluating the methods described in the previous two subsections a decision has to be taken on the selection criteria. The first criterion must obviously be that the model is able to estimate all the parameters required. Thereafter, there are two basic performance criteria; complexity (time consumption) and accuracy. These requirements are normally competing.

3.4.1 Channel models for system design

For system design purposes statistical channel models or characteristics of physically measured channels are used. Of the types of statistical channel models described in this chapter only the wideband channel models describe the time dispersion of the channel, as required to allow the estimation of the behaviour of high speed, large bandwidth systems. The models from Subsection 3.3.1 fulfil these requirements. Also, if the model is to be used to predict the performance of smart antenna systems, directional information must be included.

Two statistical models that provide all the required channel parameters are presented here. these are the *TUV Geometrical Model* described in [Fuhl97] as well as the model by Nørklit and Bach Andersen described in [Nørklit98]. They are quite similar in that they are both geometrically based, meaning that they are motivated from the geometry of the channel, estimating the channel from assumptions about the position of significant scatterers. They have both shown to compare reasonably well with experimental data, both in terms of time- and space dispersion. The Nørklit model is more complex, being 3 dimensional.

It is suggested that the Nørklit model is appropriate for microcellular, urban scenarios, where the antenna height difference between the transmitter and receiver will be important to the nature of the mobile radio channel. For rural areas, which is the focus of the work described here, the *TUV Geometrical Model* will provide sufficient accuracy. In rural areas, the model should be used without significant scatterers around the base station, but with significant distant scatterers (see Figure 12).

When using statistical models to estimate the system performance there should always be made an effort to make the models as similar to reality as possible, by comparing with experimental data. An alternative to using statistical models, as described above, is to use recorded data from representative scenarios.

3.4.2 Channel models for radio planning

For radio planning deterministic channel models, or possibly statistical models with correction factors, should be used. Only the wideband models will provide information about time and angular dispersion as well as path loss. There are three main candidate categories of models, all described in Subsection 3.3.2; 1) *ray tracing models*, 2) *3D radar models* and 3) *models using fullwave solutions* (called *fullwave models* from now on).

When limiting the scope to rural areas, as described in Chapter 1, the ray tracing models will be least appropriate. This is because of their inherent assumption of all obstacles being smooth, electro-magnetically large polygons. In addition their ability to handle multiple reflections or reflection-diffractions will be much more useful in dense urban or indoor than in rural environments, because of the large number of obstacles in these cases.

Models using 3D fullwave solutions may become applicable for macrocellular rural areas, but are currently not implemented. The large complexity leads to unacceptably high time consumption, even with powerful computers. Thus, presently the 3D radar models seem to be most appropriate for rural areas.

Complexity:

The time consumption in the 3D radar models depends on how the reflection are taken into account. Another factor is the map resolution. The *order* of the reflection modeling signifies how many multiple reflections are used. Due to the loss normally being large, only diffuse scattering of the first order is taken into account. In the simplest implementations diffraction is only taken into account in the vertical plane through transmitter and receiver. Only scattering facets with line of sight to both Tx and Rx are then considered. More advanced implementation will take into account diffractions to and from the scattering facets as well.

Another factor that is important to the complexity is the way the search for the significant scatterers is performed. If no pre-test is performed all facets in the map area must be taken into account. A possible technique to speed up the estimation is to limit the area, at the risk of disregarding significant scatterers from far-off positions. Another techniques to speed up the search for the significant scatterers use a fast, geometrical search for surfaces with line-of-sight to both Tx and Rx. This is discussed in Chapter 4.

Which 2D model to use in the vertical Tx-Rx-plane is another critical factor for the time consumption. Most implementations use quite simple UTD-based models. In [Liebenow95] it was concluded that using a parabolic equation 2D model was too time consuming to be used in practise in planning tools. However, later results showing very fast implementations of fullwave 2D models may make this feasible (e.g. [Brennan98]).

The total time consumption will also be strongly dependant on the digital map resolution. Unfortunately, this aspect is not treated thoroughly in the litterature. Lie and Remvik [Lie97] report an estimation time of approximately 50-100 ms per grid location using a map with resolution 100 m on Pentium 90 over distances up to a few km. In [Becker95] a fast scatterer search method that reportedly decreased computation time by 80% is described, but no actual time reference was given.

Accuracy:

The accuracy of radio planning tools can be evaluated be their ability to predict parameters describing *path loss*, *time dispersion* and *angular dispersion*. Most authors report accuracies for path loss prediction. There have not been a lot of results reported on the ability of wideband channel models to accurately predict the *time* and *angular dispersion*. In [Liebenow96] it was shown that by using a 3D radar model the GSM-specific Q16-parameter[21] could be estimated with an average error of –1.1 dB and a standard deviation for the error of 7.6 dB. In

[21] The Q16 parameter is defined as the amount of signal power within a 16 μs window to the amount outside. The length 16 μs is equal to the length of the channel equalizer window in GSM.

[Davidsen94] the delay spread parameter was estimated, with an accuracy of "approximately ±10%".

The most important estimation parameter in radio planning is path loss, because it has the most direct influence on the positioning of base stations. The most common performance criteria are the mean (systematic) error and the standard deviation of the estimated path loss compared with measurements. Table 1 lists recorded accuracy parameters for various channel models. Also some 2D models are included for comparison. These results give an indication of the performances reported. Care should be taken when comparing results obtained in different environments, as the amount of data, the frequency, the map underlay and the terrain type all will differ between different investigations. When results from several measurement series from the same area are reported, the number given in the Table is the average.

Lacking values indicate missing information in the original paper.

Measurement location	**Model type**	**Frequency (MHz)**	**Area Type**	**Tx-Rx-dist. [km]**	**Mean error (dB)**	**STD error (dB)**
Bristol; UK	3D radar	1823	Rural	1-2		7.7
Florø, Tretten, Røyse; Norway	3D radar	900	Rural, hilly		-3.2	7.6
Garmisch Partenkirchen; Germany	3D radar	919/1873	Mountain-ous	approx. 1-18	-1.8	5.0
Aalborg; Denmark	MFIE (2D)	1900	Rural	6-11	5.1	8.7
Aalborg; Denmark	IFIE (2D)	1900	Rural	6-11		8.2
Aalborg; Denmark	Mult. half-screen	1900	Rural	6-11	3.0	7.6
Aalborg; Denmark	PE (2D)	1900	Rural	6-11	6.7	8.3
Aalborg; Denmark	UTD	1900	Rural	6-11	3.4	10.2
Aalborg; Denmark	Neural Network	970	Rural	6-11	2.9	5.7
Aalborg; Denmark	Hata	1900	Rural	6-11	4.0	10.3
Aalborg; Denmark	Forward scattering	1900	Rural	6-11	5.3	6.8

Table 1. Path loss prediction comparison, using different types of channel prediction methods

The first three models are 3D radar models, developed by the University of Bristol, SINTEF, Trondheim and Deutsche Telekom, respectively. They are all discussed in more detail in Chapter 4. The fourth and fifth model are Integral Equation methods as discussed in this chapter, the EFIE model as developed in Aalborg, Denmark [Hviid95], and the MFIE model as

developed in Dublin, Ireland [Moroney95]. The multiple half-screen model is based on replacing the terrain with absorbing half-screens ([Walfisch88], [Berg94]) with a solution using theory of diffraction. The parabolic equation model follows the technique described in Subsection 3.2.2 and is developed by Ericsson [Berg94_2]. The UTD method is the implementation described in Subsection 3.2.2 developed at the University of Karlsruhe. The ninth method is one based on neural network training as discussed in Subsection 3.2.1 developed by Alcatel and the University of Stuttgart. The Hata implementation is a semi-empirical approach following the technique suggested in [Badsberg95] using knife-edge diffraction in combination with Okumura-Hata. The (fast) forward scattering technique is based on empirical propagation curves and geometrical diffraction [Kuhlmann95].

It should be noted that a large number of the results listed are based on the same measurement data from rural area in Aalborg, Denmark. This is because the measurement data were made freely available, and it was recommended to use these data to compare with predictions so that model performances could be compared.

The Table shows that the 3D models have better performance on average than the 2D models, but the difference is perhaps smaller than expected. It should however be noted that the test area in Denmark was chosen to have limited transversal height variation, making it suitable for 2D prediction. In [Lie97] it was shown that on the most extreme test route the standard deviation for the error was reduced from 21 dB to 7 dB by going from 2D to 3D.

As expected the semi-empirical Hata-implementation had the poorest performance. However, its performance was probably surprisingly good, indicating that by using appropriate correction factors, semi-empirical approaches may provide acceptable results, at least for uncomplicated scenarios.

A comment should be given about the good performances of the neural network model and the Deutsche Telekom 3D model. As discussed in Subsection 3.2.1 the inherent disadvantages of the neural network approach are that they are not physically based, and that the performance is very specific to the area in which the training was performed. In this case it is suspected, although not explicitly stated, that the training was performed for data from the same area as the experiments were performed. As described in Chapter 4, the Deutsche Telecom model uses a very simple description for the scattering, needing only one parameter. This scattering parameter is found from optimisation from experiments. It may be questioned if the results presented are slightly optimistic since the parameter optimisation is performed based on the same measurement campaign as the actual experimental data used.

Results from predictions made in urban area environments have also been inspected, although that is not the focus of this investigation. The results in terms of error is in the same order of magnitude as the results given in Table 1. The standard deviation of the error ranges from approximately 6 dB up to 14 dB. Ray-tracing techniques have varying performance. For scenarios where the base station is above or close to the average rooftop height the ray-tracing should be 3D, taking into account over rooftop diffraction. The best performances were found on a ray-tracing tool developed at the University of Stuttgart [Hoppe98] and a simple recursive model based on propagation along street canyons [Berg95]. Also in urban areas neural network approaches were shown to work very well.

Conclusion:

Based on the results and discussions in this chapter and considering the requirements from Chapter 1 it has been concluded that the 3D radar models are most appropriate for rural area radio planning purposes. The main reasons are that

- the model provides all the necessary parameters according to the requirements identified,

- the model provides good accuracy with respect to channel estimation, and
- the model has a reasonable complexity, making it applicable for implementation into radio planning tools.

More detailed suggestions about the implementation, as well as results from an implemented test-case are described in Chapter 7.

4 Scattering and diffraction theory applied to mobile radio channels

This chapter gives an overview of scattering and diffraction applied to mobile radio channels. Section 4.1 gives a brief overview of the main theories for scattering from rough surfaces with a focus on models currently used in 3D radar models. Section 4.2 contains a review of existing radio channel models using rough surface scattering. Section 4.3 discusses the requirements for the types of models discussed in the previous section, and identifies possible extensions and improvements. In this section the inherent limitations of the models, due to for instance weather and seasonal changes, are also discussed. Section 4.4 provides suggestions for improving the performance of 3D radar models, and identifies work items that have been carried out and are described in the remainder of this report.

4.1 Theory of scattering from rough surfaces

4.1.1 Statistical description of rough surfaces

A surface can be regarded as *rough* (as opposed to *smooth*) when irregularities in the surface lead the reflected wave from the surface to differ *significantly* from a specular reflection. The *roughness* is due to the phase differences experienced by rays reflected from different parts of the surface. An often-used criterion to distinguish between *rough* and *smooth* surfaces was suggested by Rayleigh. The criterion states that the surface can be considered rough if the phase difference of reflected components exceeds $\pi/2$. Figure 15 illustrates the concept [Boithias87].

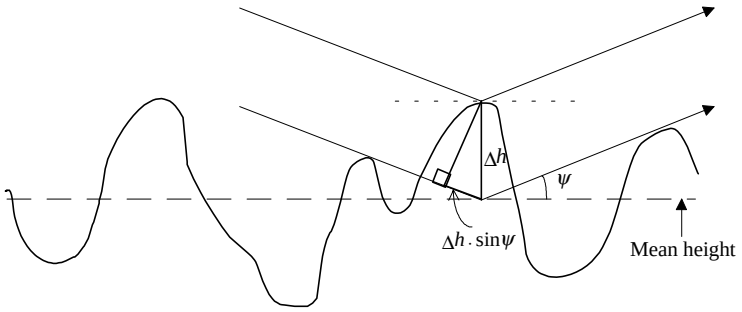

Figure 15. Reflections from a rough surface [Boithias87].

The phase difference between the components shown is $2 \cdot \frac{2\pi}{\lambda} \cdot \Delta h \cdot \sin\psi$. Using the Rayleigh criterion a surface can therefore be regarded as rough if

$$\Delta h \geq \frac{\lambda}{8\sin\psi} \qquad \textit{(eq. 44)}$$

Note that surfaces that are rough at one angle of incidence can be smooth at another. Rayleigh's criterion looks rather arbitrary, but has proven to be satisfactory for rough surface classification. In a real environment all degrees of roughness ranging from perfectly smooth to completely rough will be present. Figure 16 illustrates schematically what happens with the scattered energy from a surface with increasing degree of roughness. In a) the surface is *smooth*, whereas in b) it is *slightly rough*, leading part of the coherent energy to be scattered randomly into a diffuse field. In c) the surface is *very rough*, leading the diffuse field to dominate and the coherent field to be neglectible.

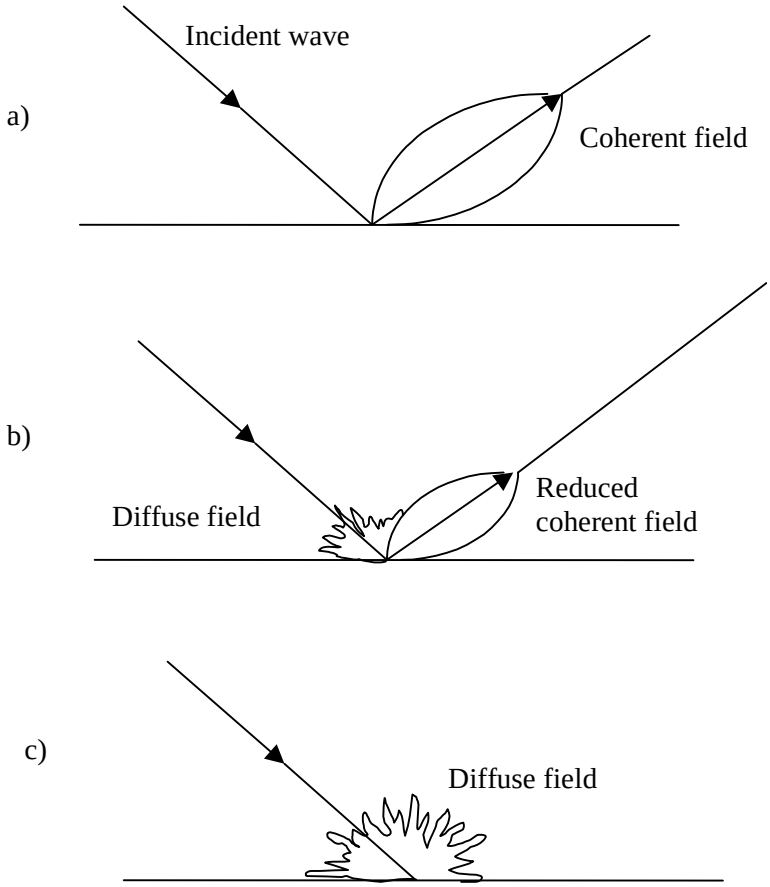

Figure 16. Schematic of scattered energy from a surface which is a) smooth, b) slighly rough and c) very rough. Taken from [Ogilvy91]

A deterministic description of an individual rough surface would not be appropriate for the purpose of mobile radio channel prediction. Therefore only statistical solutions are sought in this case[22]. The statistics of the surface must be used for such a solution to be found. The surface will normally be described by its deviation from a smooth, reference surface. The height variations can be seen as a continuous, random process, where the height in a given

[22] Solutions to deterministic rough surfaces include IE methods (i.e. [West99]).

position **r** is $h(\mathbf{r})$. The height distribution is $p(h)$. Often the height distribution is assumed to be Gaussian, which means that it can be written as

$$p(h) = \frac{1}{\sigma\sqrt{2\pi}} \cdot e^{\left(-\frac{h^2}{2\sigma^2} \right)} \qquad \textit{(eq. 45)}$$

where σ is the standard deviation of the height variation.

The surface can also be described by its correlation function, that assumes that the statistical properties are independent of **r**. The correlation function provides a measure for the *rate of change* on the surface. It is written [Ogilvy91]

$$C(\mathbf{R}) = \frac{\left\langle h(\mathbf{r}) \cdot h(\mathbf{r}+\mathbf{R}) \right\rangle_s}{\sigma^2} \qquad \textit{(eq. 46)}$$

where $\langle ... \rangle_s$ denotes spatial averaging. Most surfaces will have correlation functions in which $C(R)$ decay to zero as the value of R increases. Quite often the correlation functions suggested are of Gaussian shape, written as

$$C(R) = e^{\left(-\frac{R^2}{{L_0}^2} \right)} \qquad \textit{(eq. 47)}$$

where L_0 is the surface correlation length. The mathematical functions are chosen to allow analytical solutions. In addition to the statistics of the height distribution, the electromagnetic properties of the surface must be known for a solution to be possible.

A surface is referred to as *homogeneous* if the electromagnetic properties (permitivity, permeability, and conductivity) are constant over the surface [Ulaby89]. The surface is *statistically homogeneous* if the electromagnetic properties are not necessarily constant, but that the statistical parameters are the same over the surface. If a surface is statistically homogeneous, and in addition the surface height distribution is the same over the area, the surface is referred to as *statistically uniform*. A very useful property of statistically uniform surfaces is that the radar cross-section is the same no matter which part of the surface is inspected.

The surface is *isotropic* if the statistics of the statistics of the surface is independent of direction along the surface. This is almost always assumed for practical purposes, but as shown in Chapter 5 is not always the case in practise. A *stationary* surface is assumed to have the same statistics independent on position. If a surface is *ergodic* the statistics of the surface can be found either from many realisations (ensamble averaging) or equivalently from many different part of one realisation (spatial averaging). This latter property is necessary if surface statistics are to be obtained from inspection of the surface.

Solutions to scattering problems are always sought in the form

$$a(\mathbf{r}) = a_i(\mathbf{r}) + a_S(\mathbf{r}) \qquad \textit{(eq. 48)}$$

where a is the total fieldstrength in the position given by the vector $\mathbf{r}$, a_i is the incident wave and a_S is the sought scattered fieldstrength. The solution is normally found by applying the appropriate boundary conditions on the surface.

4.1.2 Perturbation theories

The perturbation theories are solutions that exist given that the surface is only *slightly rough*.

Perturbation theory:

This technique uses the following two requirements on the height function [Ogilvy91]

$$\begin{aligned} k\left|h(x,y)\right| &<< 1 \\ \left|\nabla h(x,y)\right| &<< 1 \end{aligned} \qquad \textit{(eq. 49)}$$

where k is the propagation constant. When a Taylor series expansion of the fieldstrength function on the surface is used, these requirements lead the series to be convergent, allowing a limited number of elements in the series. The *order* of the solution refers to the number of elements used. First order solutions take only the first two terms into account and the fieldstrength on the surface can be written

$$a(\mathbf{r})\Big|_{z=h} = a(\mathbf{r})\Big|_{z=0} + h \cdot \frac{\partial a(\mathbf{r})}{\partial z}\Big|_{z=0} \qquad \textit{(eq. 50)}$$

whereas for second order solutions the fieldstrength is written

$$a(\mathbf{r})\Big|_{z=h} = a(\mathbf{r})\Big|_{z=0} + h \cdot \frac{\partial a(\mathbf{r})}{\partial z}\Big|_{z=0} + \frac{h^2}{2} \cdot \frac{\partial^2 a(\mathbf{r})}{\partial z^2}\Big|_{z=0} \qquad \textit{(eq. 51)}$$

The solution can be found by applying the appropriate boundary conditions to the Helmholz scattering integral equation, which can be written [23]

$$a_S(\mathbf{r}) = \int_S \left[a(\mathbf{r_0}) \frac{\partial G(\mathbf{r}, \mathbf{r_0})}{\partial n_0} - G(\mathbf{r}, \mathbf{r}_0) \frac{\partial a(\mathbf{r})}{\partial n_0} \right] dS(\mathbf{r_0}) \qquad \textit{(eq. 52)}$$

In this equation $\mathbf{r_0}$ is a point on the surface and $\mathbf{n_0}$ is the unit normal vector on the surface. G is the Green's function

[23] This equation can be found by using that the total field is a harmonic solution to the wave equation and use the divergence theorem and Green's first and second theorem, see e.g. [Beckman63].

$$G(\mathbf{r},\mathbf{r_0}) = \frac{e^{jk|\mathbf{r}-\mathbf{r_0}|}}{4\pi \cdot |\mathbf{r}-\mathbf{r_0}|}. \qquad \textit{(eq. 53)}$$

The form of the solution is dependent on the type of boundary condition used. The solutions can most easily be found in the case of a *Dirichlet boundary condition*, which can be written

$$a(\mathbf{r})|_{z=h} = 0 \qquad \textit{(eq. 54)}$$

In this case it can be shown that the first order solution is the sum of a coherent field and a diffuse field where the coherent field is the same as that produced by a smooth surface, $a_s = a_{coh} + a_{diff}$. Therefore the first order perturbation theory does not conserve energy.

For an incident plane wave with elevation angle θ_i, the resulting diffuse power $P_{diff} = a_{diff} \cdot a_{diff}^{*} = |a_{diff}|^2$ in the far field in scattering elevation angle θ_s and relative azimuth angle $\Delta\phi$ is shown to be

$$P_{diff} = \frac{4k^4 \cos^2\theta_i \cos^2\theta_s}{r^2} \cdot A_M \cdot P(kA, kB) \qquad \textit{(eq. 55)}$$

where A_M is the area of the surface and *r* is the distance from the surface. $P(s_1, s_2)$ is the two-dimensional power spectrum of the surface, found by a Fourier transform of the correlation function $C(x, y)$. In addition

$$\begin{aligned} A &= \sin\theta_i - \sin\theta_s \cos\Delta\phi \\ B &= -\sin\theta_s \sin\Delta\phi \end{aligned} \qquad \textit{(eq. 56)}$$

Different types of boundary conditions give slightly different results. The solution for second order perturbation theory is of similar form and can be shown to be

$$P_{diff} = \frac{4k^4 (1+V)(1+V^{*}) \cos^2\theta_i \cos^2\theta_s}{r^2} \cdot A_M \cdot P(kA, kB) \qquad \textit{(eq. 57)}$$

where V is the surface mean field reflection coefficient which can be approximated as

$$V = 1 - 2k^2\sigma^2 \cos^2\theta_i \qquad \textit{(eq. 58)}$$

where σ is the root mean square height variation of the surface.

The validity of the perturbation theory is restricted by the requirements in eq. 49. The accuracy will decrease as the angle of incidence decreases. The theory does not take shadowing (parts of

the surface is not illuminated due to the roughness) into account, but multiple scattering is included up to the order of the perturbation solution.

Rayleigh theory:

This method is based on writing the unknown scattered field as a sum of outgoing plane waves and solving for the unknown coefficients by satisfying the boundary conditions. The first solution was reported to be first presented by Rayleigh in 1907 and later in 1945 [Ogilvy91], and was for normally incident waves upon a periodic surface. The theory was later extended to random rough surfaces [Rice51] and for arbitrary angles of incidence [LaCascue56]. The method does not take multiple scattering into account, and inherently assumes the surface to be only slightly rough, allowing the series to converge.

Phase perturbation method

The phase perturbation method ([Winebrenner85], [Broschat90]) is a newer approach which has been shown to have a larger range of validity than the classical small perturbation method. The method is based on the extinction theorem, which takes its name from the assumption that within the body of the scatterer the field is zero. By starting with the Helmholz integral equation and using the above condition, the result is an integral equation with the derivative of the total field within the integrand. The perturbation theory is used to write the derivative as a truncated series expansion. The phase perturbation method uses an expansion in the form of a sum of harmonic functions, $\sum_i \frac{(k\varepsilon)^i}{i!} \cdot e^{i\cdot\phi(x)}$, where the unknown function $\phi(x)$ is allowed to have variations only in one dimension, along the x-axis.

4.1.3 Kirchoff theory

The *Kirchoff theory* is based on solving the scattering problem by using the approximation that each point on the scatterer is part of an infinite plane, parallel to the local surface tangent. Therefore the method is also called the *tangent plane method*. The method is widely used in antenna theory. An adoption to natural surfaces is straight-forward, and comparisons with measurements are reasonably good for a certain degree of roughness.

The formulation starts with the Helmholtz scattering formula, which can be written

$$a\ (\mathbf{r}) = a_i(\mathbf{r}) + \int_{S_0} \left[a_s(\mathbf{r_0}) \frac{\partial G(\mathbf{r},\mathbf{r_0})}{\partial n_0} - G(\mathbf{r},\mathbf{r_9}) \frac{\partial a_s(\mathbf{r})}{\partial n_0} \right] d\mathbf{S_0} \qquad \textit{(eq. 59)}$$

where a is the total field, a_i is the incident field and a_s is the scattered field. The integration is over the *closed* surface $\mathbf{S_0}$, and $\mathbf{r}$ is inside the enclosed volume that contains no sources. G is the Green's function as given in eq. 53. A conventional assumption is to extend the surface to be an infinite plane below a half sphere at $|\mathbf{r}| = \infty$, allowing an integration over a closed surface. Since the closed volume contains no sources, one can write

$$\int_{S_0} \left[a_i(\mathbf{r_0}) \frac{\partial G(\mathbf{r},\mathbf{r_0})}{\partial n_0} - G(\mathbf{r},\mathbf{r_9}) \frac{\partial a_i(\mathbf{r})}{\partial n_0} \right] d\mathbf{S_0} = 0 \qquad \textit{(eq. 60)}$$

By comparing with eq. 59 this means that the a_S inside the integral in eq. 59 can be interchanged with the total field a. Then the integral equation can be written

$$a_S(\mathbf{r}) = \int_{S_0} \left[a(\mathbf{r_0}) \frac{\partial G(\mathbf{r}, \mathbf{r_0})}{\partial n_0} - G(\mathbf{r}, \mathbf{r_9}) \frac{\partial a(\mathbf{r})}{\partial n_0} \right] d\mathbf{S_0} \qquad \textit{(eq. 61)}$$

A number of approximation and assumptions is then introduced to solve this equation:

1. The Kirchoff approximation, which states that the field at any point on the surface can be written as

$$a(\mathbf{r_0}) = [1 + \Gamma] \cdot a_i(\mathbf{r_0}) \qquad \textit{(eq. 62)}$$

2. The incident wave is plane and monochromatic.
3. The observation is in the far field, such that $|\mathbf{r}|$ is much larger than the dimensions of the surface.
4. The reflection coefficient Γ is constant over the surface.

It can then be shown [Ogilvy91] that the general solution can be found from

$$a_S(\mathbf{r}) = \frac{-j \cdot k \cdot e^{jkr}}{4 \cdot \pi \cdot r} \cdot 2F(\theta_i, \theta_S, \Delta\phi) \cdot \int_{S_M} e^{jk\varsigma(x_0, y_0)} dx_0 dy_0 + a_e \qquad \textit{(eq. 63)}$$

where the integration is over the mean plane S_M (usually z=0). Also, the phase function ς is defined as

$$\varsigma(x_0, y_0) = Ax_0 + By_0 + Ch(x_0, y_0) \qquad \textit{(eq. 64)}$$

The angular factor F is

$$F(\theta_i, \theta_S, \Delta\phi) = 0.5 \cdot \left(\frac{Aa}{C} + \frac{Bb}{C} + c \right) \qquad \textit{(eq. 65)}$$

The constants A, B, C, a, b and c are defined as

$$\begin{aligned} A &= \sin\theta_i + \sin\theta_S \cos\Delta\phi \\ B &= \sin\theta_S \sin\Delta\phi \\ C &= -(\cos\theta_i + \cos\theta_S) \\ a &= \sin\theta_i (1+\Gamma) - \sin\theta_S \cos\Delta\phi (1-\Gamma) \\ b &= \sin\theta_S \sin\Delta\phi (1+\Gamma) \\ c &= \cos\theta_S (1+\Gamma) - \cos\theta_i (1-\Gamma) \end{aligned} \qquad \textit{(eq. 66)}$$

a_e is a term due to the edge effect. In [Beckman63] it is argued that this term can be disregarded for surfaces much larger than the wavelength.

The *coherent field* is equal to the complex expectation value of the scattered field, and can be found from

$$a_{coh} = \langle a_s \rangle \qquad \textit{(eq. 67)}$$

The *diffuse field* has an expectation value equal to zero, its average power is defined as

$$P_{diff} = \left\langle a_s \cdot a_s^{*} \right\rangle - \langle a_s \rangle \cdot \left\langle a_s^{*} \right\rangle \qquad \textit{(eq. 68)}$$

The solutions take an especially simple form in the case of Gaussian surface statistics. In this case the coherent field is

$$a_{coh} = a_{s0} \cdot e^{-g/2} \qquad \textit{(eq. 69)}$$

where a_{s0} is the field in the case of a plane surface, g is given by

$$g = k^2 \sigma^2 (\cos\theta_i + \cos\theta_s)^2 \qquad \textit{(eq. 70)}$$

and σ is the standard deviation of the height distribution.

The diffuse power can be written

$$P_{diff} = \frac{k^2 F^2 {L_0}^2 e^{-g}}{4\pi r^2} A_M \sum_{n=1}^{\infty} \frac{g^n}{n!\, n} \exp\left(- \frac{k^2 (A^2 + B^2) {L_0}^2}{4n} \right) \qquad \textit{(eq. 71)}$$

where L_0 is the surface height correlation length and A_M is the surface size. This expression can be simplified for the cases of small to medium roughness in which closed form expressions can be found by a truncation of the infinite sum. In the case of *slightly rough* surface the solution is

$$P_{diff} = \frac{k^4 C^2 F^2}{r^2} A_M \, P(kA, kB) \qquad \textit{(eq. 72)}$$

where $P(s_1, s_2)$ is the surface power spectrum as defined in the previous subsection.

In the case of *very rough* surface the series in eq. 71 does not converge. In this case [Beckman63] has shown that the total power, which is almost equal to the diffuse power in the case of very rough surface (no coherent field), can be approximated as

$$P_{tot} = \frac{k^2 F^2 \sigma^2}{r^2} \cdot \frac{1}{g} \cdot A_M \cdot p_{12}\left(\frac{A}{C}, \frac{B}{C}\right) \qquad \textit{(eq. 73)}$$

where $p_{12}(x, y)$ is the single-point joint probability distribution for the x and y surface gradients given as

$$p_{12}(x, y) = \frac{{L_0}^2}{4\pi\sigma^2} \exp\left(-\frac{{L_0}^2 (x^2 + y^2)}{4\sigma^2}\right) \qquad \textit{(eq. 74)}$$

Generally Kirchoff theory is most accurate for medium rough surfaces, and less accurate for very rough surfaces, due to its assumption that requires the surface to be locally plane. A restriction for the applicability of Kirchoff theory is given in [Ogilvy91] as

$$k \cdot r_c \cdot \cos^3 \theta_i >> 1 \qquad \textit{(eq. 75)}$$

where r_c is the minimum radius of curvature for the surface. A discussion of the range of validity for the SPM and the Kirchoff methods is provided in [Khenchaf96].

As Kirchoff is based on similar assumptions as the Small Perturbation method, it does not converge energy.

4.1.4 Depolarisation

The solutions given in the two previous subsections are scalar; in order to study *depolarisation,* which is coupling between polarisations, vector solutions must be used. Appendix A shows the results for the polarisation dependant vector solutions for the perturbation theory and the Kirchoff theory.

4.1.5 Other models

An approach was used by Braun and Dersch in [Braun91]. It was shown that under certain conditions the scattering from random, rough surfaces can be approximated as being Nakagami-m distributed, so that

$$p(a) = \frac{2m^m a^{2m-1}}{\Gamma(m)\Omega^m} e^{-(m/\Omega)\cdot a^2}, \qquad \textit{(eq. 76)}$$

where the parameters m and Ω are physical parameters that can be derived from the surface roughness h_{rms} and the surface correlation length L. This reduces to the Rayleigh distribution for m≈1.

Didascalou et.al. [Didascalou01] has described a method to predict rough surface scattering for use in ray-launching. The method makes a Kirchoff like assumption in that it is based on a tangentially plane approximation. The surface is divided into subsurfaces from which the individual contributions (rays) can be found in a statistical sense using the statistics of the slope

on the surface. Unlike in the Kirchoff formulations, the coherent and diffuse components are predicted at the same time, which will be an advantage for ray-launching techniques taking diffuse scattering as well as coherent reflections into account, making such techniques more plausible. The method was verified using simulations and comparing with predictions from the Kirchoff formulations.

A hybrid model type referred to as a *two-scale model* is described by Khenchaf in [Khenchaf96] and [Khenchaf99]. The model uses both Kirchoff and SPM in the same model to overcome the restrictions in validity for the two models. The model allows different degrees of roughness in the same surface. In [Ro88] a model called the *facet-emsemple method* is described. The model in based on a description of the surface as consisting of piecewise flat, infinitely long strips, so that interior and exterior wedges are formed. The model calculates the field as a superposition of reflections from the facets and diffractions from the wedges using UTD. Only a one-dimensional solution is provided.

4.1.6 Lambertian based methods

Lambert's law (1760) states that the brightness of a rough surface is equal in all viewing directions. This extremely simple assumption has been used to model rough surfaces. In bistatic radar terms the assumption can be written

$$\sigma^0 = \frac{R}{\pi}\cos\theta_i \qquad \textit{(eq. 77)}$$

where σ^0 is the normalised bistatic radar cross section, as described in Chapter 2, R is a constant and the cosine dependence on the incidence angle is due to the amount of energy illuminating the surface.

Oren model:

Oren and Nayar [Oren95] have developed a model describing the scattering from many rough surfaces, each of them having Lambertian scattering. The Oren model was developed for use in *machine vision*, and the verification and rationale behind the model was therefore for visible light frequencies [24]. Brook et. al. [Brook96] applied the model to mobile communication frequencies (1 GHz) and transferred the description to bistatic radar terms.

The model assumes the surface area *dA* to be built up of a large number of smaller facets with area *da*, each of the smaller facets being Lambertian. The smaller facets *da* are large compared to the wavelength, allowing the use of GO. These assumptions can be written as

$$\lambda^2 << da << dA \qquad \textit{(eq. 78)}$$

The facets appear in pairs, forming a V-shape, and the width of each facet is much smaller than its length. The orientation with respect to the global surface normal is given by the angle θ_a. The geometry is illustrated in Figure 17.

[24] An example of a rough surface not being well described by a Lambertian model at light frequencies is the fact that the moon appears like a disc when viewed from afar. If Lambertian scattering had been the case the moon would appear brightest in the middle and dark at the edges.

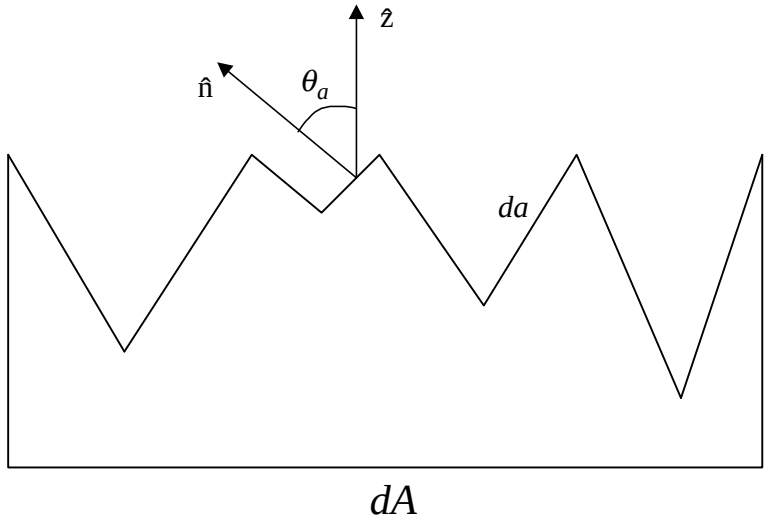

Figure 17. Geometry of the Oren model, the facets are arranged in V-cavities, each oriented with an angle θ_a to the normal direction. Taken from [Oren95]

The angle θ_a is assumed to have a Gaussian distribution with variance σ^2. The model takes into account shadowing (parts of facets are not visible from the transmitter), masking (parts of the facets are not visible from the receiver) as well as first order multiple reflections. It is shown in [Oren95] that the resulting normalised radar cross section can be written in the form

$$\sigma^0(\theta_i,\theta_s,\Delta\phi) = \frac{R}{\pi}\cos\theta_i \cdot (K_1 + K_2) \qquad \textit{(eq. 79)}$$

where K_1 accounts for direct reflection, whereas K_2 accounts for components due to multiple reflection. These factors are defined as

$$K_1 = C_1 + \cos(\Delta\phi)\cdot C_2 \cdot \tan\beta + (1-|\cos(\Delta\phi)|)\cdot C_3 \cdot \tan\left(\frac{\alpha+\beta}{2}\right) \qquad \textit{(eq. 80)}$$

$$K_2 = 0.17\frac{R^2}{\pi}\cdot\frac{\sigma^2}{\sigma^2+0.13}\cdot\left[1-\cos(\Delta\phi)\cdot\left(\frac{2\beta}{\pi}\right)^2\right] \qquad \textit{(eq. 81)}$$

where

$$\begin{aligned}\alpha &= \max[\theta_s,\theta_i]\\ \beta &= \min[\theta_s,\theta_i]\end{aligned} \qquad \textit{(eq. 82)}$$

and

$$C_1 = 1 - 0.5\frac{\sigma^2}{\sigma^2 + 0.33}$$

$$C_2 = \begin{cases} 0.45\dfrac{\sigma^2}{\sigma^2 + 0.09}\cdot \sin\alpha & if\ \cos(\Delta\phi) \geq 0 \\ 0.45\dfrac{\sigma^2}{\sigma^2 + 0.09}\cdot\left(\sin\alpha - \left(\dfrac{2\beta}{\pi}\right)^2\right) & if\ \cos(\Delta\phi) < 0 \end{cases} \qquad \textit{(eq. 83)}$$

$$C_3 = 0.125\frac{\sigma^2}{\sigma^2 + 0.09}\cdot\frac{4\alpha\beta}{\pi^2}$$

Note that for the special case of $\sigma^2 = 0$ the model reduces to the Lambertian model. Note also that the model results in a normalised radar cross section independent of the surface size, which indicates that the model is unsuitable to model plane or only slightly rough surfaces, where the coherent field will be significant.

In Figure 18 an example plot of the estimated normalised radar cross section is shown for the case of σ=36° and θ_i=75°. The plot shows all receiving angles, ranging from $\Delta\phi = 0^\circ$ (back-scatter) to $\Delta\phi = 180^\circ$ (forward scatter) and from $\theta_s = 0^\circ$ (vertical) to $\theta_s = 90^\circ$ (grazing). Note that the maximum is found in directions close to the backscatter direction. The breakpoint when θ_s exceeds θ_i is due to masking.

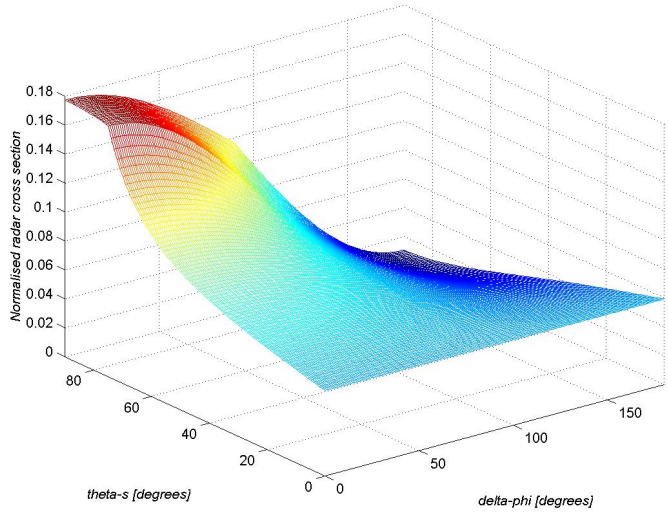

Figure 18. Normalised radar cross section estimation from the Oren model for σ=36°, θ_i=75°.

URN:NBN:no-1290

Other models

A simple radio channel prediction tool for urban areas by Degli-Esposti and Bertoni [DegliEsposti99] has been developed to take diffuse scattering into account. The model assumes the scattering to be Lambertian, characterised by two parameters; the scattering coefficient *S* and the reflection loss factor *R*. The model conserves energy, as all the incident power is either specularly reflected or diffusely scattered by an amount given by the model parameters.

A slightly more elaborate approach was used by Braun and Dersch in [Braun91]. It was shown that under certain conditions the scattering from random, rough surfaces can be approximated as being Nakagami-m distributed, so that

$$p(a) = \frac{2m^m a^{2m-1}}{\Gamma(m)\Omega^m} e^{-(m/\Omega)\cdot a^2}, \qquad \textit{(eq. 84)}$$

where the parameters m and Ω are physical parameters that can be derived from the surface roughness h_{rms} and the surface correlation length *L*. This reduces to the Rayleigh distribution for m≈1.

4.1.7 Plane surface model

Although not really a rough surface scattering model, the plane surface model is included because it is used in a number of prediction tools.

The model is based on the reflection characteristics of a rough surface, described in Subsection 2.2.2.

The received power for each measurement point can in this case be written as

$$\frac{P_r}{P_t} = \tilde{g}_t \cdot \tilde{g}_r \cdot \Gamma^2 \cdot \left(\frac{4\pi\left(\tilde{R}_t + \tilde{R}_r\right)}{\lambda} \right)^2 \qquad \textit{(eq. 85)}$$

where $\tilde{g}_t$ and $\tilde{g}_r$ are the antenna gains in the direction towards the point of reflection.

4.2 Current status of scattering based prediction models

4.2.1 The Karlsruhe model

The first implementation found using the combination of a 2D vertical plane solution and a 3D extension using bistatic radar theory (3D radar model) is the one described in [Lebherz92]. The 2D model is based on UTD and replaces terrain obstructions with equivalent wedges or convex surfaces to obtain a solution. This model is described in Section 3.3. The 3D extensions used is based on *Kirchoff theory* and the *Small Perturbation method*, both described in Section 4.1. The statistics of the height variation of the rough surfaces is assumed to be Gaussian. The model is polarisation dependent, each estimated component being characterised by its direction of polarisation in addition to its phase and amplitude. The implementation described takes only

first order scattering/reflection into account, and only reflections from surfaces with LOS to both transmitter and receiver are taken into account.

The frequency range considered is 70-960 MHz. The map database used has a resolution of 100 m, so that the reflections are calculated for each square surface (pixel) of 100 m 100 m. The land cover is divided into 6 classes, each characterised by its electrical properties, standard deviation of height distribution as well as correlation length. The classes are; *urban, suburban, farmland/field, forest, bush/heathland* and *water*.

The model can calculate the fieldstrength both in a deterministic manner and a statistical manner. In the first case the estimation is simply based on complex summation of all the estimated signal components. In the latter case the summation is performed statistically in that the phase of each of the signal components is assumed to be uniform ($[0,2\pi]$). From this the probability density function (PDF) of the fieldstrength is calculated rather than a single value, and the estimation can be given as a tolerance band with a given confidence. This technique was applied to the demonstration model in Chapter 7. In [Kurner96] a fast, asymptotic method to calculate the mean value only using the Karlsruhe model is shown.

Although experiments were performed, no figures for the accuracy of the model were provided in [Lebherz92]. Complexity and computing time were not discussed for the model.

In a later paper ([Becker95]) algorithms to speed up the Karlsruhe model by using a faster search for the scatterers in the 3D extension were described. One algorithm decreased computation time by 80% with no degradation in performance, whereas another algorithm decreased computation time by 93% with only a slight degradation in performance. Both algorithms use geometrical methods to easily find positions with LOS to both Rx and Tx, therefore this approach will not be useful for models allowing diffracted-scattered, scattered-diffracted or diffracted-scattered-diffracted signal components. In [Kurner96] it was shown that the Karlsruhe model predicted the delay spread parameter within approximately 20% compared with measurements.

4.2.2 The Bristol model

A model similar to the Karlsruhe model has been developed by Tameh et.al. [Tameh97]. However, this model is aimed to be used also in microcells and uses a more accurate map database. Buildings are included as polygons in the database. The resolution is variable; 50 m in rural areas, but increased to 10 m in urban areas.

The 2D part of the model is diffraction based, and can also take the effect of foliage into account. The scattering part of the model included Kirchoff, Small Perturbation and the Oren models (all described in Section 4.1), but since the performances were similar the Oren model was preferred because of its simplicity. The model can take into account scattering from pixels that do not have LOS to Rx and Tx. The implementation described in [Tameh97] is not polarisation dependant, but this has been included in a later version of the model [Tameh00].

A similar type of land cover classification to the one in [Lebherz92] has been used. Although slightly more detailed, the division being into 10 classes rather than 6. The model can be used for a range of frequencies, but experiments were performed only at 1823 MHz (narrowband). An rms error of 7.5 dB for vertical polarisation and 8 dB for horizontal polarisation was found comparing the model with experiments in rural areas.

In a later paper slightly better results were reported, with an rms error of 6.5 dB in a mixture of urban and rural environment [Tameh98]. Different models for foliage loss were used and

different 2D diffraction models were tested. It was concluded that a UTD based model showed better performance than knife-edge diffraction models (e.g. Epstein-Peterson, Section 3.2).

4.2.3 The Trondheim model

Lie and Remvik [Lie97] in Trondheim developed a model based on a similar approach to the Karlsruhe and Bristol models. The model is apparently GSM specific (900 MHz) and the development was partly motivated by the desire to predict problem areas in GSM with a large time dispersion.

A diffraction model is used in the vertical Tx-Rx plane and off-axis reflection/scattering is taken into account like in the other models. The map resolution is 100 m. The model does allow diffraction to and from the reflecting pixels to be taken into account. Only first order reflection/scattering is included. A very simple modeling of the bistatic radar cross section was used, the normalised cross section being

$$\sigma^0 = \gamma(\cos\theta_i \cos\theta_s)^{0.5} \qquad \textit{(eq. 86)}$$

where γ is a terrain dependant parameter. No reference to this model was given, but the form is recognised as similar to the *first order Small perturbation method* if the coherent field is neglected. No details about the land cover or values for γ were given.

GSM measurements were performed in areas with rural, hilly terrain. The measurements included both signal level and signal quality. Comparisons between the estimated time dispersion and signal quality were performed, the conclusion being that the model was able to predict bad signal quality due to time dispersion. For the signal level an rms error ranging from 6.6 to 8.9 dB was measured.

The computational time was also reported. The processing was done on a HP work station 9000/720 (performance similar to a Pentium 90). The speed was slightly dependent on area, the estimation time per grid location (100 m 100 m) ranging from 55.5 ms to 109.3 ms. This added up to 1650 s for a 298 km^2 area and 5660 s for a 518 km^2 area.

4.2.4 Deutsche Telekom model

A fourth model, similar to the ones above, was developed by Deutsche Telekom and is described in [Liebenow94], [Liebenow95] and [Liebenow96]. The main motivation for developing the model was to predict the time dispersion (impulse response) in the radio channel, but it was also shown that the path loss prediction improved compared to 2D measurements as well.

Three different models were tested for the 2D part of the model, a simple Okumura-Hata empirical model, the diffraction based Deygout model and an advanced Parabolic Equation (PE) based method. The best results were achieved using the PE method, but in [Liebenow95] it was concluded that this method was too slow to be used in planning tools. In later work analytical 2D models have been speeded up considerably (e.g. [Brennan98]). In [Liebenow96] it was suggested to use a method based on the Vogler diffraction model [Vogler82].

A very simple approach to the modeling of the rough surface scattering was taken. The model assumed that from each scattering surface a ratio *C* of the power illuminating the surface was scattered in a Lambertian manner. This leads the radar cross section to be written

$$\sigma^0 = 4C \cdot (\cos\theta_i \cdot \cos\theta_s) \qquad \textit{(eq. 87)}$$

The value for *C* was decided by using best fit to wideband measurements, the value used was *C=-10dB* for 900 MHz and *C=-13dB* for 1900 MHz. No distinction was made between land usage classes. Only scattering surfaces with line-of-sight to both Tx and Rx were taken into account.

Wideband measurements in mountainous areas in Garmisch Partenkirchen, Germany were compared to predictions. The impulse response estimation seemed to be accurate, although not quantified. The prediction of the path loss had a mean error of 1.8 dB and a standard deviation of 5.0 dB, which is very accurate, but it should be kept in mind that the value for C was chosen from best fit. It was shown that using only the 2D model gave much poorer performance.

4.2.5 Other models

A 3D prediction tool was also developed by the Faroese Telecom (Faroe Islands) in cooperation with the University of Aalborg, Denmark [Davidsen94|. The motivation for the model was to identify problem areas in GSM due to reflections with excess delay longer than the GSM equalizer length [Eggers92]. The model uses only scattering and reflection, and provides no additional 2D vertical plane solution. It is therefore mostly useful for the prediction of time dispersion. The scattering is assumed to be Lambertian, with the exception of sea reflections, which are allowed to be specular. The model is able to predict the delay spread parameter within approximately ±10%, and the GSM specific Q16 parameter[25] within approximately ±2dB

Although not a fully implemented channel prediction model, similar techniques to the ones described in the previous subsections were used by Brook et.al. [Brook95] to estimate the scattering from surfaces in a mountainside in Canada. By using a virtual antenna array technique and wideband measurements they were able to identify the scattered components from individual facets in a 100 m 100 m grid. By using the Oren scattering model they experienced a correlation of 0.88 between measured and predicted radar cross sections, whereas a Lambertian model gave a correlation of 0.80.

4.3 Requirements for 3D radar models

The models described in the previous section show good agreement with experiments and have a reasonably low complexity compared to fullwave solutions. Unfortunately, the accuracy in predicting time- and angular dispersion has not been reported to a large degree. A few results are mentioned in Chapter 3.

A suggested improvement of the radar models is to do 2D modeling using a state-of-the-art model, like PE or IE. Although more complex, these models have shown better performance than UTD based or knife-edge diffraction models.

None of the models do take higher order reflection/scattering into account. Higher order scattering is recommendable when coherent components exist, in order to take *reflected-scattered* or *scattered-reflected* components into account. In cases where no coherent

[25] The Q16 parameter is defined as the amount of signal power within a 16 μs window to the amount outside. The length 16 μs is equal to the length of the channel equalizer window in GSM.

component exist, the contribution from higher order scattering is neglectable, due to the large loss in each diffuse scattering.

In urban areas, multiple reflections from walls will be an important propagation mechanism. In these cases a different model, such as ray-tracing, should be used.

The models are normally restricted to diffractions in a vertical plane, either the *Tx-Rx vert. plane*, the *Tx-scatterer vert. plane* or the *scatterer-Rx vert. plane*. This is a reasonable restriction in the case of natural terrain. This is illustrated in Figure 19, where an obstruction with significant diffraction components in two planes is constructed in a) and a more typical example is shown in b), with no diffraction component from edge 2 reaching Rx. Remember that according to UTD the diffracted ray will always have the same angle as the incident ray relative to the diffracting edge. Again, the situation for built-up areas is completely different, with around corner diffraction being an important propagation mechanism.

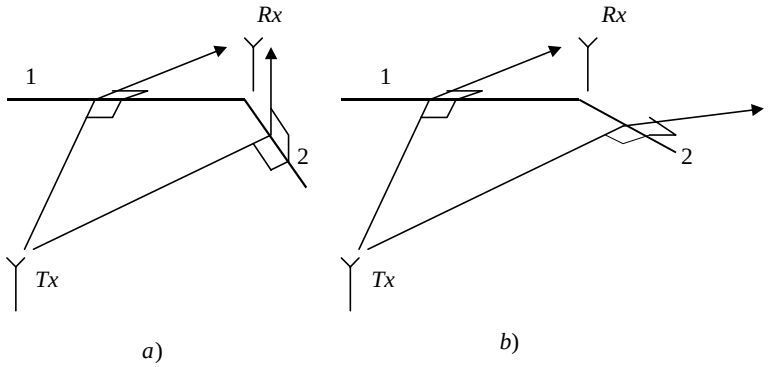

Figure 19. a) Diffraction component from both edge 1 and edge 2 reach Rx due to very steep edge, b) more typical example for natural terrain, the diffraction from edge 2 does not reach Rx.

It is recommended to use alternative methods to estimate the radar cross sections. Results reported show that the models seem to be insensitive to the scattering model used. This observation can be explained by the empirical fitting procedure used to compare measurements with model data. A more detailed analysis should be performed to investigate the influence of various natural surfaces, each of them having a specific surface roughness.

4.4 Improvements to 3D radar models

Based on the discussion in the previous section, the following work items to inspect and improve the accuracy and understanding of 3D radar models were identified.

1. A detailed analysis of the 3D scattering contribution from natural surfaces is the key element for an improvement of 3D channel models. Each surface, e.g. grass, agriculture field, forest, will have a specific contribution, which has to be characterised.

   The characterisation will be performed through a measurement campaign to inspect the scattering from natural surfaces ranging from *slightly rough* to *very rough*. The measurements provide the basis to characterise the surface, either by using existing rough surface scattering models or by creating a new model. The goal is to identify a model that

allows an easy characterisation of the scattering characteristics of a natural surface, to be used in a 3D radio planning tool. The model should be valid for mobile communications frequencies and be valid for surfaces ranging from plane to very rough. This measurement campaign is described in Chapter 5.

2. A subject that has not been much discussed is the influence of weather and seasonal conditions on the radio channel prediction. This is particularly important when models for foliage attenuation are taken into account, as the conditions will significantly change with the season. Also the radar cross section results will change with weather and season, especially in areas with snow in the winter. These types of uncertainties will introduce limits on the achievable accuracy of the model. Some of the experiments described in Chapter 5 are repeated under different weather conditions, and the variations in the results are discussed.

3. A sensitivity analysis for this type of models has to be undertaken. A demonstration model is implemented and in example areas the relative importance of using a 3D model compared to 2D, the dependency of seasonal and weather variations as well as the model sensitivity to parameter variation is inspected. This investigation is described in Chapter 7.

5 Measurements and analysis of the scattering characteristics of natural surfaces

This chapter describes the characterisation of natural rough surfaces, with the aim to provide a suitable description for use in channel modeling. The first section describes a novel approach to model rough surface scattering. The second section describes the measurements of natural surfaces and the derivation of the roughness parameters for the new model. In the third section the results and analysis from the measurement campaign are presented and compared with theory.

5.1 A novel approach to the modeling of scattering off rough surfaces

As discussed in Chapter 4, none of the existing scattering models are able to describe rough surfaces with any degree of roughness. Therefore a novel approach called the amplitude/phase (A/P) model is suggested, the aim being to provide a model that is uniform, simple, and accurate for the surfaces and frequencies in question.

5.1.1 Overview

The A/P model is based on a description of the roughness by estimating the amplitude and phase contribution from individual subsurfaces, and is therefore referred to as an *amplitude/phase model*.

The model is inspired by the method described by Kaplan [Kaplan86] to predict the sidelobe levels for array antennas. The illuminated surface area is treated as a *two-dimensional array* consisting of plane, quadratic surfaces. The received fieldstrength is the complex sum of the contributions from all the squares. As described later the resulting fieldstrength will have a statistical description. The geometry is illustrated in Figure 20. The angles $\tilde{\theta}_i$, $\tilde{\theta}_s$ and $\Delta\tilde{\phi}$ are the scattering angles from transmitter (Tx) via square [m,n] to transmitter (Rx), and $\tilde{R}_t$ and $\tilde{R}_r$ are the distances from square [m,n] to Tx and Rx, respectively.

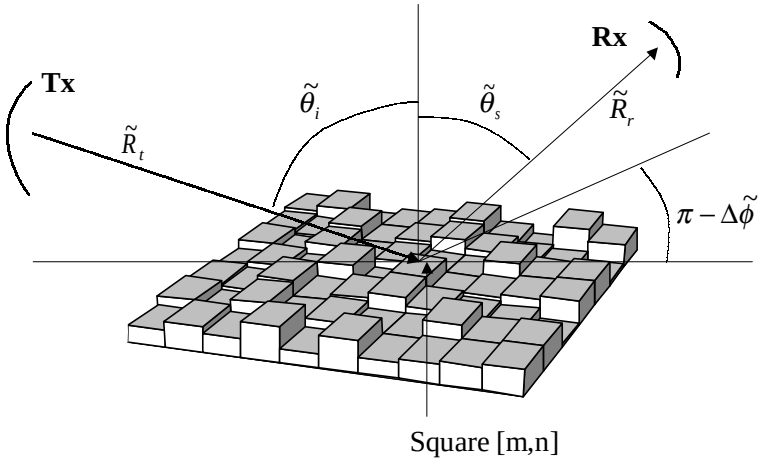

Figure 20. Model geometry, the received fieldstrength is the complex sum of the contributions from all the squares.

The size *da* of each square is much smaller than the wavelength, which again is much smaller than the total surface area *dA*[26]. This can be written

$$da << \lambda^2 << dA \qquad \textit{(eq. 88)}$$

To the scattering from each square a phase shift Φ_{mn} is associated. This phase shift has the purpose of accounting for the height variation in a rough surface. Also, in each scattering there is a power loss of $1-|\Gamma|^2$, where Γ is the reflection coefficient of the individual subsurfaces. The complex transfer function T of the propagation from Tx via square [m,n] to Rx is given as

$$T([m,n]) = \Gamma \cdot e^{j\Phi_{mn}} \cdot \sqrt{\frac{\lambda^2}{(4\pi)^3} \cdot \frac{1}{\tilde{R}_t^{\,2} \tilde{R}_r^{\,2}} \cdot \sigma_{mn}} \qquad \textit{(eq. 89)}$$

where isotropic antennas are assumed and the phase of the mean propagation signal $e^{-jk(\tilde{R}_r+\tilde{R}_t)}$ is normalised to 1. σ_{mn} is the radar cross-section of square [m,n], which is a function of the geometric angles $\tilde{\theta}_i$, $\tilde{\theta}_s$ and $\Delta\tilde{\phi}$. The radar cross-section has a particularly simple form under certain assumptions which will be defined later.

The model requires the Tx and Rx positions to be in the far-field with respect to the individual *da*, but not with respect to the whole surface *dA*. This is an advantage in the analysis of experimental results, as described in Section 5.2.

The resulting complex fieldstrength is a sum of the contributions from each square [m,n], written as

$$a_r = a_t \sum_m \sum_n T([m,n]) \qquad \textit{(eq. 90)}$$

where a_t is the transmitted fieldstrength. This means that the resulting field is a "random walk", where the step length and direction of each step is the amplitude and phase of each T([m,n]). This is illustrated in Figure 21.

[26] This seems reasonable for mobile communications, where the wavelength is in the order of 15-30 cm. The surfaces will normally be at least a few meters and the irregularities in the surfaces will typically be up to a few cm.

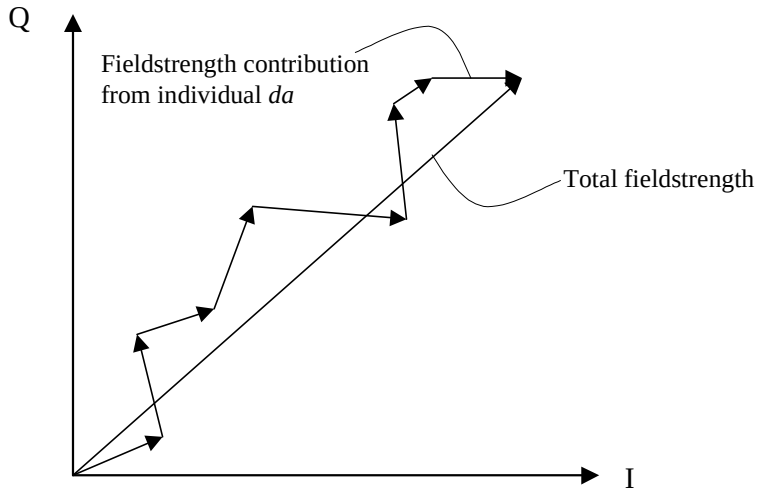

Figure 21. The resulting fieldstrength is a random walk *in the complex plane with contributions from each square da, the amplitude and phase of each T[m,n] being the step length and direction, respectively.*

5.1.2 Model assumptions

To obtain a solution some assumptions about the scattering from each square and the statistics must be made. The assumptions used in the experiments and analysis described in this report are listed below.

1. All the squares are illuminated. The model does not consider shadowing.
2. There is no coupling between squares. The model does not consider mutual interaction between the individual *da*.
3. The radar cross-section of the square *da* is given as

$$\sigma_{mn} = 4\pi \cdot \left(\frac{da}{\lambda}\right)^2 \cdot \left(1+\cos\tilde{\theta}_i\right)^2 \cdot \left(1+\cos\tilde{\theta}_s\right)^2 \qquad \textit{(eq. 91)}$$

4. Γ is uniform over the entire *dA*.
5. The phase factor Φ is uniformly distributed[27] over an interval Φ_0, so that $\Phi \in \left[-\Phi_0/2, \Phi_0/2\right]$. The phase window Φ_0 can only take on values between 0 (smooth) and 2π (maximum roughness).

Assumption 3 stems from the solution to the scattering from an infinitesimal surface with the E and H-field components on the surface given as $E/H = \eta_0$, where η_0 is the free space

[27] A Gaussian distribution was also tested, the results were almost identical as long as the standard deviation was the same.

impedance. This is equivalent to a *Huygen source*[28] (e.g. [Balanis89]). It is further assumed that the surface is an ideal electrical surface with infinite conductivity σ, leading to the circular symmetric solution in eq. 91.

The phase shift Φ_0 in assumption 5 is given as a function of the surface height variation Δh in the following manner

$$\Phi_0 = 2 \cdot \frac{\Delta h \cdot \cos(\theta_i)}{\lambda} \cdot 2\pi \qquad \textit{(eq. 92)}$$

where Δh is the (uniform) height variation of the surface. This is illustrated in Figure 22. Note that the value for Φ_0 can never exceed 2π (maximum roughness), which means that for each θ_i there exists a $\Delta h_{\lim}$ so that for all values for Δh exceeding this the value for Φ_0 is 2π, representing a *saturation* for eq. 92. This is illustrated in Figure 23, which shows Φ_0 as a function of Δh for different values of θ_i (the relation between Δh and the root mean square height variation h_{rms} is $\Delta h = h_{rms} \cdot \sqrt{12}/2$).

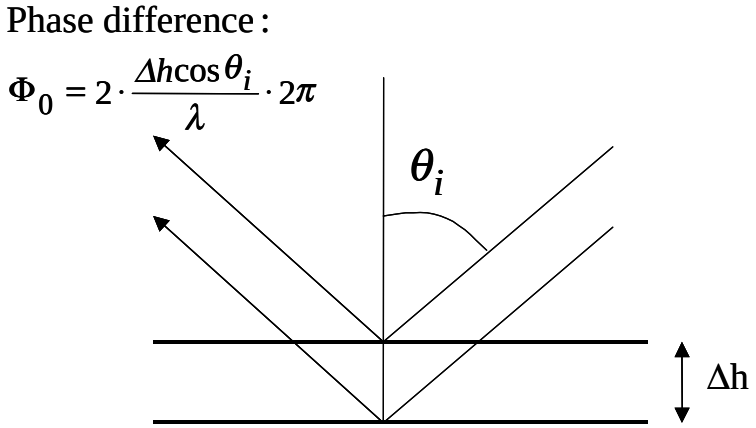

Figure 22. Illustration of the relation between the phase shift and the height variation

[28] A Lambertian $\cos\theta$ variation is sometimes assumed, which is geometrically correct when considering the power illuminating the surface. It was nevertheless considered that a Huygen source assumption was more physically sound. The largest difference between these two implementations will appear at large incidence angles, near grazing.

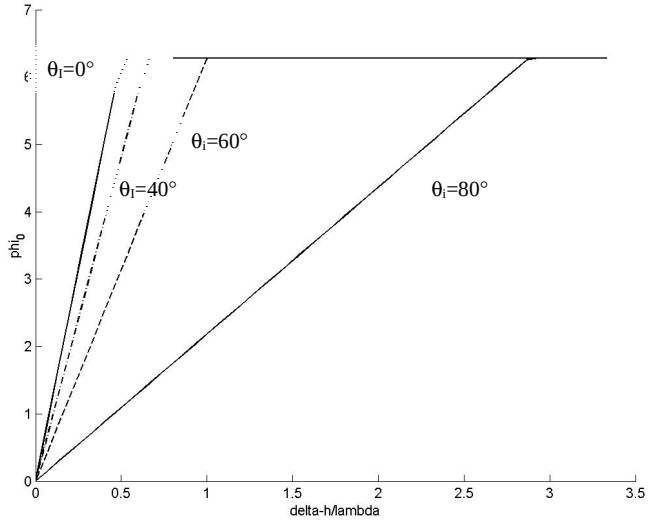

Figure 23. Phase variation as a function of height variation for incidence angle 0° (solid), 40° (dashdot), 60° (dashed) and 80° (solid)

5.1.3 Resulting contribution

The resulting scattered field from the total surface *dA* must be handled statistically using the assumptions from the previous subsection. The detailed mathematical analysis is described in Appendix B, only the results will be presented here. As in the description in Chapter 4, the resulting scattered/reflected field can be divided into a coherent, deterministic field and a diffuse, non-deterministic field. Note that the model conserves energy by subdividing the incident power into three distinct parts; 1) *the coherent reflected part* (P_{coh}), 2) *the diffuse scattered part* (P_{diff}) and 3) *the refraction and loss* (P_{loss}), so that

$$P_{tot} = P_{loss} + P_{coh} + P_{diff} \qquad \textit{(eq. 93)}$$

Figure 24 shows the amount of diffuse power in terms of total illuminating power as a function of the phase shift for different values of Γ. In the case of $\Gamma = 1$, there is no loss (P_{loss}=0) and all the power is reflected/scattered.

URN:NBN:no-1290

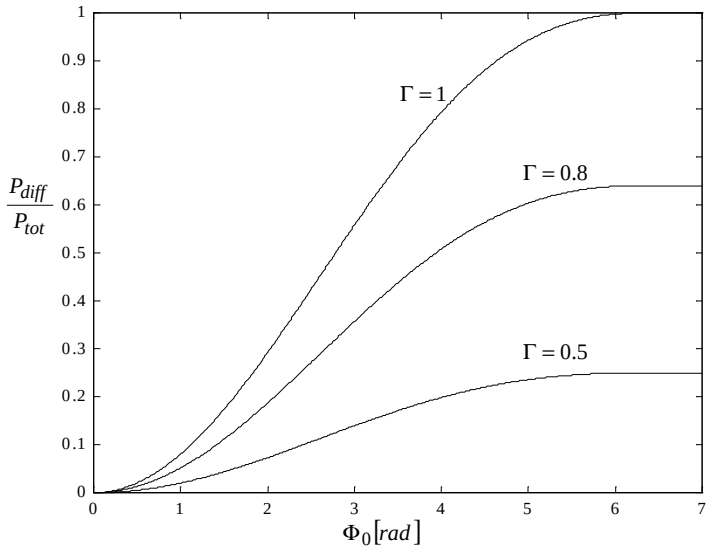

Figure 24. Illustration of the amount of diffuse to total power as a function of the phase window Φ_0

Coherent component

The coherent fieldstrength in any direction is given as (Appendix B)

$$a_{coh} = a_0 \cdot \Gamma \cdot \frac{\sin(\Phi_0/2)}{(\Phi_0/2)} \qquad \textit{(eq. 94)}$$

where a_0 is the fieldstrength in the case of a plane, lossless surface of the same size (dA). Note that if $\Phi_0 = 0$, $a_{coh} = a_0 \cdot \Gamma$, which is the case of a plane surface. For $\Phi_0 = 2\pi$, $a_{coh} = 0$, which is the case of a *completely rough* surface.

The power density S is derived from the fieldstrength *a* by

$$S_{coh} = |a_{coh}|^2 = {a_0}^2 \cdot \Gamma^2 \cdot \left(\frac{\sin(\Phi_0/2)}{(\Phi_0/2)} \right)^2 \qquad \textit{(eq. 95)}$$

In a practical implementation in a prediction tool it is suggested to use the reflection coefficient Γ_{res} to calculate the coherent field. This resulting reflection coefficient is derived from the real plane surface reflection coefficient in the following form

$$\Gamma_{res} = \Gamma \cdot \frac{\sin(\Phi_0/2)}{(\Phi_0/2)} = \mathrm{sinc}(\Phi_0/2) \qquad \textit{(eq. 96)}$$

The coherent contribution can then be estimated by using the resulting Γ and calculating the contribution as from a smooth surface using standard techniques. If the surface is large compared to the wavelength the coherent component will contribute in the specular direction only ($\theta_i = \theta_s, \Delta\phi = \pi$).

Diffuse component

The *average* diffuse signal power density can be written as (Appendix B)

$$S_{diff}(\theta_s) = \frac{3 \cdot P_{tot}}{16\pi {R_r}^2} \cdot \Gamma^2 \cdot \left[1 - \mathrm{sinc}^2(\Phi_0 / 2)\right] \cdot (1 + \cos\theta_s)^2 \qquad \textit{(eq. 97)}$$

where R_r is the observation distance and P_{tot} is the total power illuminating the surface, which can be written

$$P_{tot} = S_{inc} \frac{(1 + \cos\theta_i)^2}{4} \cdot dA \qquad \textit{(eq. 98)}$$

where S_{inc} is the power density of the signal incident on the surface and dA is the area. This follows from assumption 3 in Subsection 5.1.2 and summing up the power from all the subsurfaces.

The average diffuse power in a real implementation is most easily calculated by using a normalised bistatic radar cross-section σ^0, as described in Chapter 2. Comparing eq. 97 and eq. 98 with the definition of the radar cross-section as provided in eq. 91 it is seen that the normalised radar cross-section will have the form

$$\sigma^0{}_{diff} = (1 + \cos\theta_i)^2 \cdot (1 + \cos\theta_s)^2 \cdot \Gamma^2 \left(1 - \mathrm{sinc}^2(\Phi_0 / 2)\right) \cdot \frac{3}{16} \qquad \textit{(eq. 99)}$$

The diffuse fieldstrength in any direction is Rayleigh distributed, and the total fieldstrength in any direction is Rice distributed. As described in Appendix B, the Rice distribution appears from the sum of a deterministic component with amplitude *a* and a Rayleigh distributed random component with power $2{\sigma_0}^2$, where σ_0 is the Rayleigh parameter. The amount of coherent power to the amount of diffuse power is denoted the *K-factor* (e.g. [Parsons92]).

Polarisation dependence

The polarisation dependence is directly derived from the assumption of the scattering from a Huygens source.

In the case of *vertical incident polarisation* the E-field on the surface is in the direction of the plane of incidence. In the case of *horizontal incident polarisation* the E-field on the surface is in the direction perpendicular to the incidence plane. For the scattered field, the notation *co-polar* component will here be used about the θ-component in the case of vertical and about the ϕ-component in the case of horizontal incident field. Similarly, the notation *cross-polar* is used about the ϕ-component in the case of vertically and about the θ-component in the case of

horizontally polarised incident field. The direction of the scattered field from subsurfaces can then be found from

$$E_{co-polar} \sim \cos(\pi - \Delta\phi) \cdot (1 + \cos\theta_s)$$
$$E_{cross-polar} \sim \sin(\pi - \Delta\phi) \cdot (1 + \cos\theta_s) \qquad \textit{(eq. 100)}$$

Note that the total field follows

$$E_{total} \sim (1 + \cos\theta_s) \qquad \textit{(eq. 101)}$$

which is in accordance with theory. Note also that in the E-plane ($\Delta\phi = 90^\circ / 270^\circ$ for horizontal polarisation and $\Delta\phi = 0^\circ / 180^\circ$ for vertical polarisation) the E-field only has θ-component, as expected. In the H-plane ($\Delta\phi = 0^\circ / 180^\circ$ for horizontal polarisation and $\Delta\phi = 90^\circ / 270^\circ$ for vertical polarisation) the E-field only has ϕ-component.

The diffuse field can then be found by using the polarisation dependent radar cross-section $\sigma^0_{diff\_pq}$ where p and q denote the incident and scattered polarisation which can have the values v (vertical) or h (horizontal) for incident, and θ or ϕ for scattered polarisation. If the notations co-polar for vθ and hϕ and cross-polar for vϕ and hθ are used, σ^0_{diff} for the co-polar case is written as

$$\sigma^0_{diff\_pq} = \sigma^0_{diff} \cdot \cos^2(\pi - \Delta\phi) \qquad \textit{(eq. 102)}$$

and for cross-polar scattering

$$\sigma^0_{diff\_pq} = \sigma^0_{diff} \cdot \sin^2(\pi - \Delta\phi) \qquad \textit{(eq. 103)}$$

On the receiver, to obtain the v and h components relative to local ground, a co-ordinate transformation is required. Note that for high scattering elevation angles $E_\theta \approx E_v$ and $E_\phi \approx E_h$.

For the coherent component the polarisation dependent reflection coefficients should be used, with the proportionality for the resulting reflection coefficient as derived in eq. 9.

5.1.4 Example implementations

In Figure 25 a)-c) three examples of the scattering from rough surfaces with increasing degree of roughness are shown. The first example shows the case of a plane surface (completely deterministic), whereas the third example shows the case of a very rough surface (completely random). The example is for a surface of size 2 m 2 m and a frequency of 1625 MHz. The incidence angle is 30°. The plots show an enlarged part of the scattered signal around the main lobe. Figure 26 shows a cross section through Δϕ=180° for the three cases in Figure 25. It is

notable that the main lobe in the case of a slightly rough surface is reduced significantly compared to the smooth surface, whereas in the case of the completely rough surface the main lobe is non-existent, the scattering showing a random pattern.

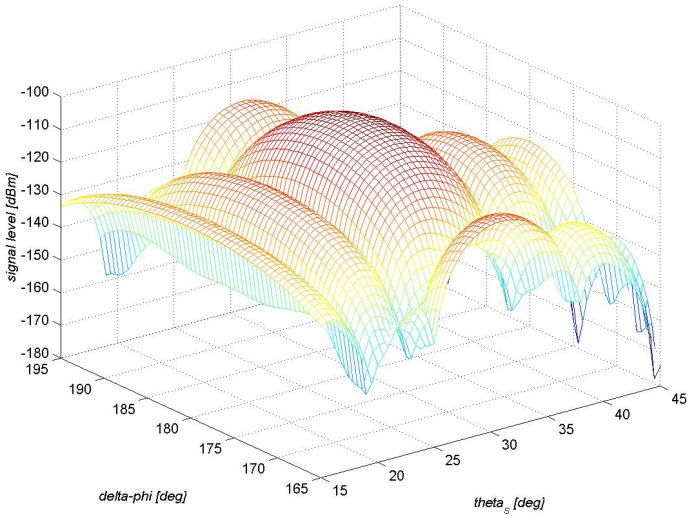

a)

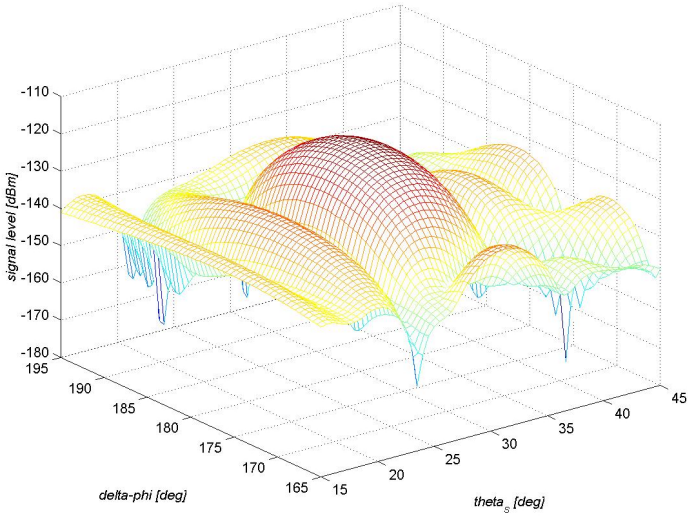

b)

Figure 25. Realisations of scattering from a) plane surface, b) slightly rough surface and c) completely rough surface, using the amplitude/phase model, surface 2 2 m, 1625 MHz, 30º incidence angle

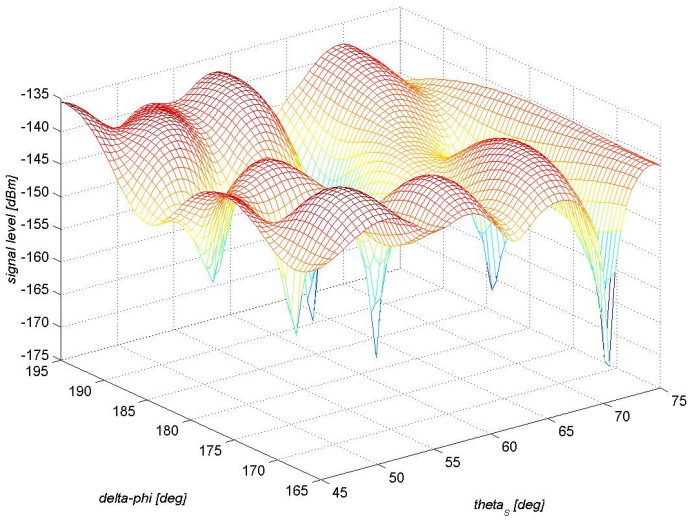

c)

Figure 25. Realisations of scattering from a) plane surface, b) slightly rough surface and c) completely rough surface, using the amplitude/phase model, surface 2 2 m, 1625 MHz, 30º incidence angle

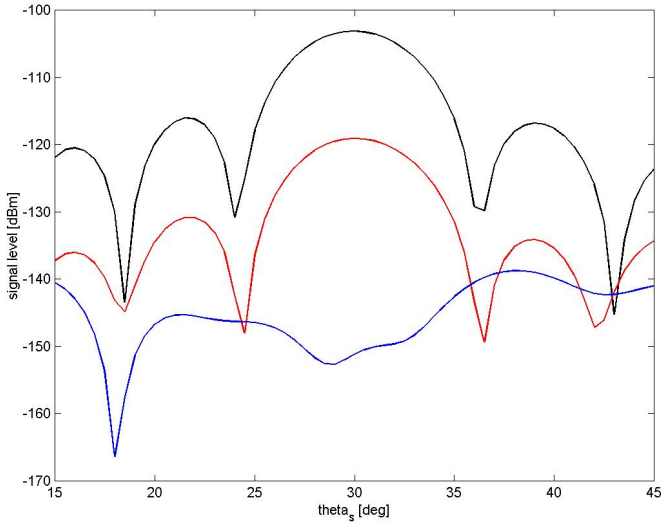

Figure 26. Realisations of scattering from a plane surface (black), slightly rough surface (red) and completely rough surface (blue), using the amplitude/phase model, cross-section through $\Delta\phi$=180°, surface 2 m 2 m, 1625 MHz, 30º incidence angle

5.1.5 Summary

In conclusion the amplitude/phase model estimates the scattering from a surface of any roughness using two parameters: 1) h_{rms}, which is the height variation of the surface, and from which the phase variation Φ_0 can be calculated, 2) Γ, which is the smooth surface reflection coefficient. From these two parameters the total scattered field can be calculated, using a subdivision into diffuse, scattered and coherent reflected components:

1. The diffuse component is found using the normalised radar cross section of the surface (eq. 12). This contribution is always Rayleigh distributed.
2. The coherent component is found using the resulting reflection coefficient (eq. 96) and treating the surface as if it was smooth. This component is non-random.
3. The polarisation dependence is taken into account by using eq. 102 and eq. 103 and provides the diffuse radar cross-sections and using the polarisation dependent reflection coefficients (Chapter 2).

This amplitude/phase model has the following advantages:

- It makes no assumptions about the degree of roughness, and is therefore equally suited to describing plane surfaces as very rough surfaces,
- it needs only two parameters to completely describe scattering from the surface,
- it has a very intuitive, direct physical interpretation,
- it takes the polarisation inherently into account, and
- it provides high performance in terms of closeness to fit for measurement data (as will be apparent in Chapter 6).

Compared to more elaborate methods for analysis of scattering from rough surfaces this method suffers from the following shortcomings:

- It does not take shadowing into account, which may influence results at low elevation angles (close to grazing incidence), and
- it neglects multiple scattering, which also may come into account at lower angles, especially for very rough surfaces

5.2 Experimental approach and method of analysis

Two different measurement set-ups were used to characterise natural surfaces. One set-up for incidence and scattering angles up to approximately 80° and one for very high incidence and scattering angles (*grazing*). Experiments of scattering were performed on a number of surfaces, ranging from *slightly rough* to *very rough*. The data analysis and assignment of roughness parameters is based on finding the optimal parameters in the amplitude/phase model using a least square fit.

5.2.1 Measurement set-up

The two measurement set-ups will be referred to as *non-grazing* and *grazing*. The reason for having two set-ups is that measurements at grazing incidence angles set special requirements to set-up and data analysis due to the strong antenna talk-over.

Non-grazing

The *non-grazing* measurement equipment was based on a reflection measurement using high gain antennas at transmit and receive, as illustrated in Figure 27. Both antennas pointed to the same position on the surface. The receiving antenna was mounted flexible to allow positioning in almost any elevation and azimuth angle. The transmitting signal was monochromatic at 1625 MHz. On the receiver side a spectrum analyser and a PC were used to log the signal power. The measurements were performed in terms of *measurement series*, each of them defined as measurements of the received power over the half sphere for both polarisations (*v* and *h*)[29], with fixed elevation and polarisation on the transmitter. Measurement series were performed for both transmitting polarisations, for different incident angles and on the following surfaces: asphalt, grass, agriculture field and forest. A more detailed description of the surfaces is given in the next subsection. The measurement set-up is described in more detail in Appendix C, a picture is shown in Figure 28, demonstrating measurements of the scattering characteristics of an asphalt plane. The radiation patterns for the antennas were accurately measured beforehand, as they were required for the analysis later on. The radiation patterns are shown in Appendix C.

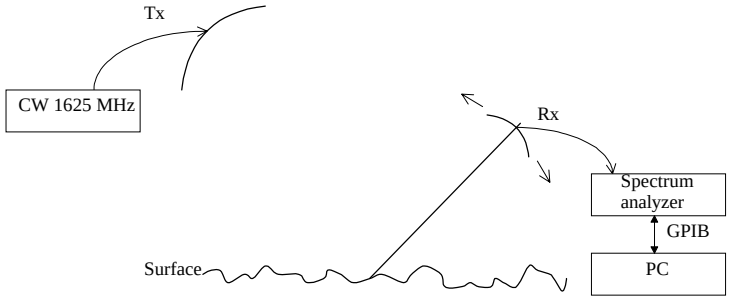

Figure 27. Non-grazing measurement equipment, illustrated schematically

[29] Since the receiver is positioned on a sphere, the directions measured are θ and ϕ, relative to the maximum point of illumination.

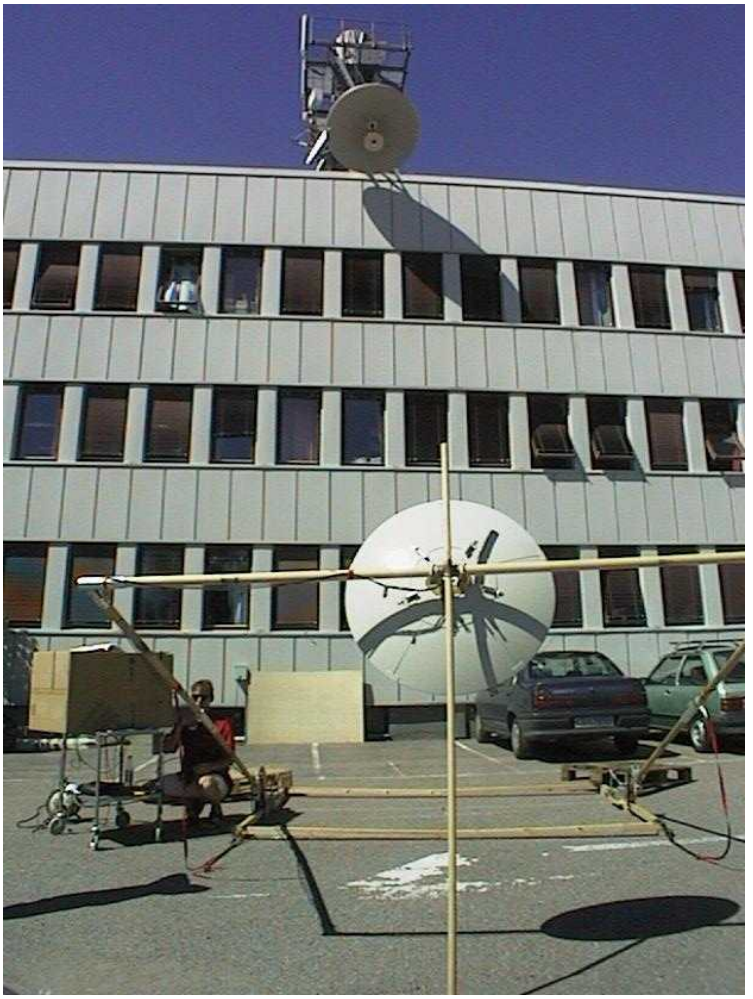

Figure 28. Picture of the non-grazing *measurement set-up. The Tx antenna can be seen in the top of the picture, the Rx antenna can be seen in the foreground.*

Grazing

The measurement set-up described above is not suited to perform measurements for very high incidence and scattering angles *(grazing incidence,* $\theta > 80^o$*)*, due to the direct radiation from the transmitting antenna to the receiving antenna. The talk-over is in this case strong compared with the reflected/scattered signal, thus making analysis of the scattered signal difficult. Contributions from grazing incidence angles are important in mobile radio channels due to the relatively low positions of transmitter and receiver. Therefore a different approach was adopted for these grazing incidence angles.

The set-up is based on equipment used for performing 3-dimensional wideband channel measurements. The set-up consisted of a wideband channel sounder and an 8-element linear array as described by Lehne et.al. [Lehne98]. By positioning the transmitter and receiver over the surface to be inspected, and by using a vertical array orientation, the set-up was able to resolve contributions from ground reflections and the direct component. The concept is

illustrated in Figure 29. Measurements were performed at 2.1 GHz on asphalt, grass and ploughed fields. The measurement equipment is described in more detail in Appendix C. A picture of the antenna array receiver is shown in Figure 30.

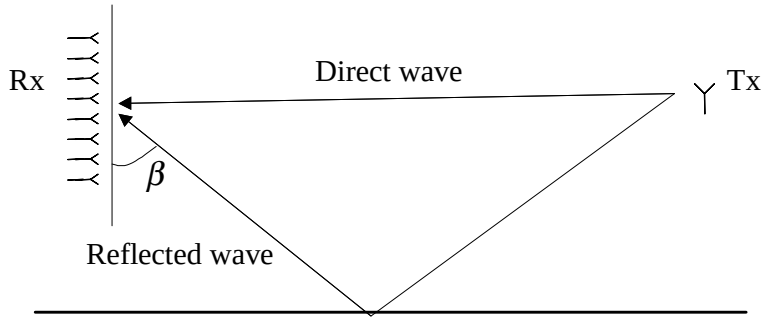

Figure 29. Grazing measurement equipment, illustrated schematically. The antenna array is shown on the left.

Figure 30. Picture of the grazing *measurement set-up receiving side, the antenna array can been seen on the left*

5.2.2 Measurement scenarios

Characterisations of surface parameters were performed on four different types of surfaces; *asphalt*, *grass*, *ploughed field* and *forest*.

Asphalt (dry and wet): The measurements were performed on a parking lot, the asphalt was slightly worn and dusty. The wet asphalt was achieved by pouring water on the same scattering surface.

Grass (dry and wet): The measurements were performed on a lawn, with relatively short, cut grass (approximately 10 cm). Comparisons with wet grass were performed after pouring plenty of water onto the grass until soil moisture saturation was achieved.

Ploughed field (with and without snow): The field consisted of humid clay, ploughed into approximately 15 cm deep tracks. Two measurement series were carried out, one in autumn before snowfall and another one with a layer of approximately 20 cm of new, wet snow on top of the frozen ground underneath.

Forest: The forest measurements were done on a forest with trees in leaf. Due to the complex landscape only a limited measurement series could be taken.

Pictures from all the measurement scenarios are shown in Appendix E. In Table 2 an overview over all the measurement series is given.

Surface	Inc. angle (deg)	Surf. conditions	Inc. polarisation	Set-up
Asphalt	30	Dry	v and h	Non-grazing
	45	Dry	v and h	Non-grazing
	60	Dry	v and h	Non-grazing
	60	Wet	h	Non-grazing
	70	Wet	v and h	Grazing
	80	Dry	v and h	Grazing
	80	*Wet*	*v and h*	*Grazing*
Grass	30	Dry	v and h	Non-grazing
	45	Dry	v and h	Non-grazing
	45	Wet	v and h	Non-grazing
	80	Dry	v and h	Grazing
	80	*Wet*	*v and h*	*Grazing*
Field	50	No snow	v and h	Non-grazing
	50	Snow	v and h	Non-grazing
	80	*No snow*	*v and h*	*Grazing*
Forest	80	Dry, in leaf	h	Non-grazing[30]

Table 2. Overview of all the measurement series performed. Row in italics: Problem with measurement equipment observed for parts of the series

5.2.3 Method of analysis

Non-grazing

In the case of the *non-grazing* measurements the analysis started by first realising that using the amplitude/phase model, the received signal in any direction ($[\theta_S, \Delta\phi]$) is Ricean distributed. This follows from the A/P model assumption of infinitesimal subsurfaces, and is discussed in Appendix B. The Rice distribution is characterised by two parameters; *a*, which is a non-random constant component, and σ_0, which is the Rayleigh parameter that describes the random (diffuse) part of the signal. The analysis is based on first estimating the Rice parameters in all directions, $a(\theta_S, \Delta\phi)$ and $\sigma_0(\theta_S, \Delta\phi)$, and then using these estimates to calculate the desired parameters Γ and Φ_0.

The statistical parameters can be estimated by realising that the parameter *a* is proportional to the amplitude in the plane, perfectly reflecting case, a_0, in all directions and can be written as

[30] Note that in the forest case the non-grazing equipment was used even though the incidence angle was 80°. This was possible by first performing measurements to identify the forest as a completely rough surface and then performing the measurement series itself at scattering angles $\theta_S < 70^\circ$, to avoid antenna talk-over.

$$a(\theta_s, \Delta\phi) = \hat{a} \cdot a_0(\theta_s, \Delta\phi) \qquad \textit{(eq. 104)}$$

where $\hat{a}$ is a constant. Since the surface under inspection is large compared to the wavelength, the shape of a_0 is found using image theory, in all directions

$$\frac{a_0}{a_t} = \sqrt{\tilde{g}_t \cdot \tilde{g}_r \cdot \left(\frac{4\pi(\tilde{R}_t + \tilde{R}_r)}{\lambda} \right)^2} \qquad \textit{(eq. 105)}$$

where a_t is the transmitted fieldstrength, $\tilde{g}_t$ and $\tilde{g}_r$ are the antenna gains in the direction towards the geometric point of reflection, and $\tilde{R}_t$ and $\tilde{R}_r$ are the distances from the Rx and Tx to the point of reflection, respectively. Note that a_0 will have a shape decided by the antenna diagrams and that a_0 will be neglectible at angles far away from the specular direction due to the low antenna gain.

The diffuse power P_{diff} has the same shape as the scattering from the individual subsurfaces in the A/P model. From this (Appendix B) it follows that the shape of the Rayleigh parameter σ_0 as a function of direction can be written as[31]

$$\sigma_0 = \hat{\sigma}_0 \cdot (1 + \cos\theta_s) \qquad \textit{(eq. 106)}$$

where $\hat{\sigma}_0$ is a constant. The diffuse part of the received signal in any direction results from an integral over the illuminated surface of the form

$$P_r = \iint_A \frac{P_t g_t(\theta_i, \phi_i) g_r(\theta_s, \phi_s) \lambda^2}{(4\pi)^3 R_t^2 R_r^2} \cdot \sigma^0 \cdot da \qquad \textit{(eq. 107)}$$

where g_t and g_r are the antenna gains in the direction of each surface point as described in Chapter 2, and σ^0 is the normalised bistatic radar cross-section[32].

The task is thus simplified to estimating the two constants $\hat{a}$ and $\hat{\sigma}_0$. This was done for each measurement series by finding the optimal parameters in the mean square sense in the following manner

$$[\hat{a}, \hat{\sigma}_0]_{opt} = \min_{\hat{a}, \hat{\sigma}_0} \sum_{\theta_s} \sum_{\Delta\phi} \left(\tilde{\rho}(\theta_s, \Delta\phi) - E_\rho(\theta_s, \Delta\phi) \right)^2 \qquad \textit{(eq. 108)}$$

[31] This requires that the variations of θ_s as seen from the Rx antenna are small over the illuminated area, which was shown to be the case for all measurement scenarios.

[32] The normalised bistatic radar cross-section σ^0 in eq. 20 should not be confused with the Rayleigh parameter σ_0 in eq. 19.

where $\tilde{\rho}$ is the measured amplitude in the given direction and E_ρ is the Rice expectation value (Appendix B). The measured amplitude is the sum of the received amplitude in the two polarisation directions. Note that in both eq. 105 and eq. 107 the antenna gains are included, therefore, for an accurate estimate to be possible it is essential to have accurate knowledge of both the Tx and Rx antenna diagrams.

Using these statistical parameters $[\hat{a}, \hat{\sigma}_0]$, in eq. 108, Γ and Φ_0 are estimated using conservation of energy. The details of the estimation are given in Appendix D.

The phase window Φ_0 can be directly translated into a height variation Δh for a given incidence angle θ_i through

$$\Phi_0 = 2 \cdot \frac{\Delta h \cos\theta_i}{\lambda} \cdot 2\pi \qquad \textit{(eq. 109)}$$

This relationship is illustrated earlier in Figure 23 and Figure 22. A height variation Δh will lead to a phase variation $\Delta\Phi$ as shown in Figure 22. Due to the nature of a phase characterisation, a height variation $\Delta h > \Delta h_{\lim}$, resulting in phase $\Phi_0 > 2\pi$ will always be reduced to the $0...2\pi$ range. This also means that $\Delta h_{\lim}$ is the maximum height which can be resolved from the measurements, unless a higher θ_i is used in the experiment.

Grazing

Under grazing incidence angles the main task is to separate direct and reflected parts of the signal, as illustrated in Figure 29. In this analysis the measurements from an antenna array are used together with an ESPRIT based DoA mechanism (Appendix D).

The strongest component will be the direct, free space component, arriving at the relative time delay $\tau = 0$ under an arrival angle of $\beta = 90^\circ$ and with amplitude α_0. The angle β is defined relative to the negative z-axis as shown in Figure 29. For surfaces with a significant coherent component, there will be a dominant second component in the direction of specular reflection, which was about 80° in the set-up used in this work. Most surfaces appear smooth at grazing incidence angles, this second component was significant on all observed surfaces.

The analysis started by identifying the dominant specular reflected component. A reasonable estimate for the resulting reflection coefficient in this case is

$$\hat{\Gamma}_{res} = \frac{|\alpha_{refl}|}{|\alpha_0|} \qquad \textit{(eq. 110)}$$

where α_{refl} is the amplitude of the coherently reflected component and α_0 is the amplitude of the direct free space component, both resulting from the ESPRIT analysis. As surfaces appear smooth for grazing incidence, the phase variation Φ_0 is small, allowing to represent Γ by Γ_{res}.

In order to estimate the diffuse components, the direct and dominant reflected components are removed from the received signal and a different algorithm would be used to estimate the diffuse part. Unfortunately this method did not work satisfactorily due to apparent imperfect estimation of the two strong components, leading the estimated diffuse signal to be slightly

corrupted. Due to this only a reliable estimation of Γ could be found in the grazing incidence measurements. It was however shown using generated test data that the suggested method will indeed work if the estimates for the two strong components are accurate. This is shown in Appendix D, where the method of analysis is discussed in more detail.

Occasional instability was observed for the equipment, leading the results to differ somewhat from series to series on the same surface, and also within measurement series. Therefore, the estimates for the reflection coefficient Γ given in Appendix E are in terms of the mean values taken over a number of measurements.

5.3 Results and analysis

For each of the measurement series in the case of non-grazing equipment, the following parameters were estimated: Reflection coefficient Γ, phase shift window Φ_0 (and rms phase shift Φ_{rms}), the amount of power (%) into *coherent reflection*, *diffuse scattering* and *loss*. Also, from the phase shift window Φ_0 and the incidence angle the equivalent surface height variation Δh was calculated. In the case of the grazing measurements, the reflection coefficient Γ was estimated[33]. In Appendix E the results from all the measurements are tabulated, and also pictures of all the measurement scenarios are shown.

Figure 31 a) and b) presents an example of received power for asphalt in the θ and ϕ polarisation directions, respectively. Close inspection of the main beam in Figure 31 a) shows that it has a beam width of approximately 12 degrees. This is in accordance with theory for a relatively smooth surface, because the received signal in this case is decided by the gain of the two antennas. In the set-up used the receiving antenna illuminates the smallest area and is therefore dominating. Note that the ϕ-component (the *cross-polar* component) is zero in the incidence plane.

[33] As discussed in subsection 5.2.2 and Appendix D the estimation of Φ_0 became uncertain in the grazing measurement case due to imperfections in the DoA-measurements.

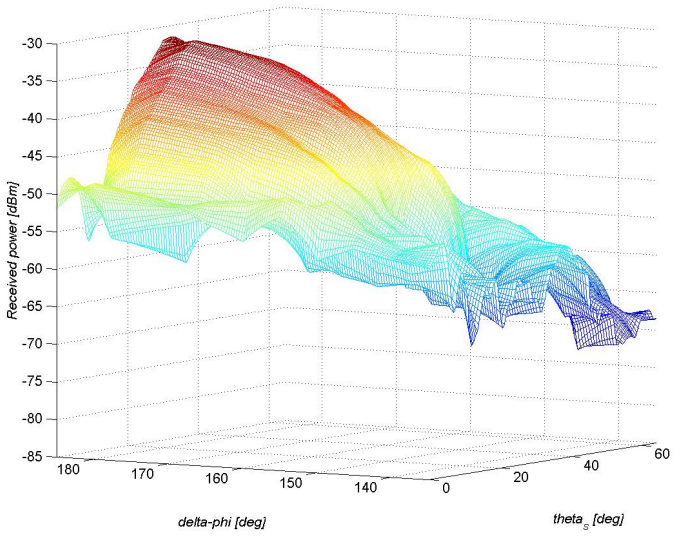

a)

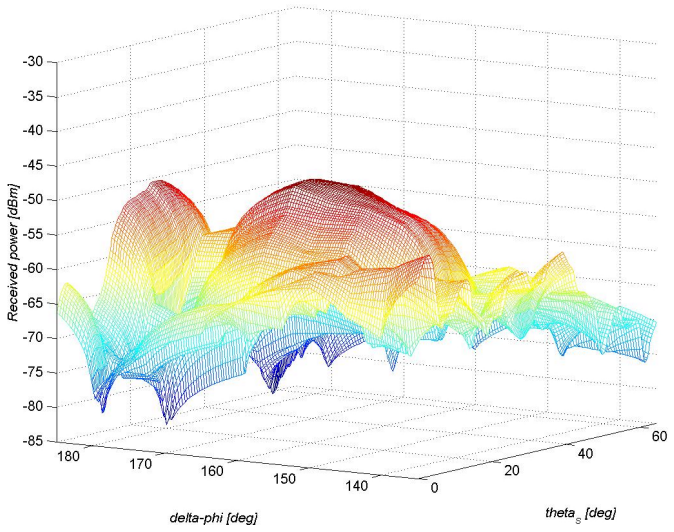

b)

Figure 31. Example of received power in the a) θ and b) ϕ polarisation directions in the case of vertical incident polarisation on asphalt.

5.3.1 Roughness

Figure 32 shows the average height variation, Δh, estimated from the phase shift variations in the analysis. *Asphalt (dry), grass (dry), ploughed field (without snow)* and *forest* provided an

increasing degree of roughness. The typical (uniform) height variations were 10 mm for asphalt, 25 mm for grass, 100 mm for ploughed field and 500 mm for forest[34].

The estimated equivalent height variations for the different surfaces are close to the physical height variations. This analysis confirms the applicability of the new model for these kinds of surfaces. Also, this result indicates that for prediction in a real case when experimental results about the phase variations are not available, the real surface height variations may be measured and used to estimate the phase variations. The exception to this is forest, where the height variation must be considered as a *equivalent* height variation resulting from the complex propagation conditions in a forest.

On asphalt the power in the coherent part was on average 18 dB larger than the diffuse power, on grass the coherent part was 9 dB higher on average, whereas for ploughed field (without snow) the diffuse power was 5 dB higher than the coherent power. In forest, no coherent power was observed. These results are in accordance the theory for rough surface scattering: A strong coherent contribution in the case of smooth surfaces, and a strong diffuse component in the case of very rough surfaces.

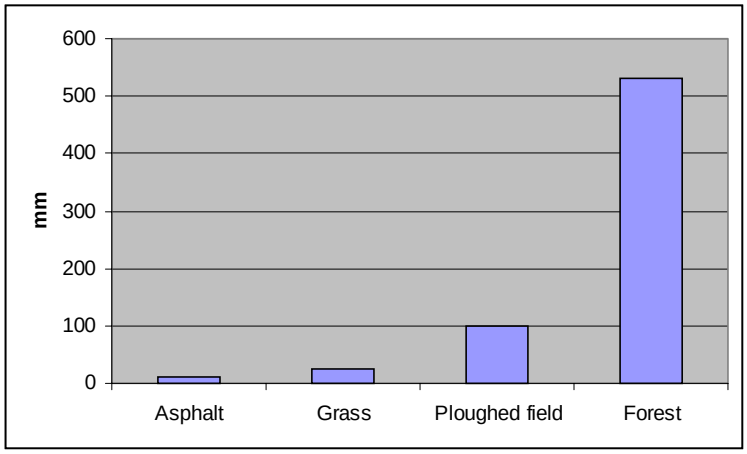

Figure 32. Average height variations, Δh, for different surface types

5.3.2 Reflection coefficients

Figure 33 shows the average values of the reflection coefficient Γ, for the different surfaces. The case *with grazing* includes all measurements, whereas *without grazing* is excluding the measurements using the grazing measurement equipment. The reflection coefficient Γ increased with increasing incidence angle, as expected from theory. Particularly, the grazing measurements provided much higher values of Γ than the non-grazing measurements. The reflection coefficient was considerable lower in the case of forest than for the other surface

[34] In the case of forest, the phase variation is the maximum (2π), therefore ideally higher incidence angles should also have been used, which might have resulted in slightly higher values for Δh. The value estimated is however used in the analysis in Chapter 7, as the results would not change significantly if a higher value for Δh had been used.

types. In the case of forest, due to the layered surface and the strong influence of multiple reflection the loss component P_{loss} dominates the scattering characteristics, leading to low values of Γ. A more accurate description of the scattering in this case may be found by using a *multilayer* description taking into account the refraction in the canopies as well as ground reflection (e.g. [Tamir77]). This will however probably require an unrealistic degree of detail in the map underlay for the type of channel modeling in question [Tameh98].

Due to the limited number of incidence angles tested, it is difficult to draw any firm conclusions on the Γ dependency as a function of the incidence angle. The largest number of incidence angles was measured in the case of asphalt, Figure 34 shows the asphalt reflection coefficient Γ as a function of incidence angle for vertical and horizontal polarisation, as well as indications of the assumed shape of the curves.

The measured curves in Figure 34 are compared to theoretical curves of Γ for very dry, moderately dry and humid soil in the case of vertical and horizontal polarisation, shown in Figure 35 and Figure 36. The minimum value in the case of vertical polarisation is called the *pseudo-Brewster angle* (Chapter 2). The asphalt measurements suggest to have a pseudo-Brewster angle at approximately 65°, which is in good agreement with asphalt seen as a flat, dry surface. The measured points for horizontal polarisation show an increase with incidence angle, which is in good agreement with the theory. The horizontal polarisation measurement at 80° does not fit to the expected curve. The discrepancy may be explained by higher absorption losses in horizontal measurements at grazing incidence angles.

In the case of the other surfaces fewer incidence angles were measured. The grass surface shows a similar tendency as asphalt for vertical polarisation. As roughness increases and absorption and diffuse scattering dominates, comparisons with a reflection coefficient of plane surfaces are no longer applicable.

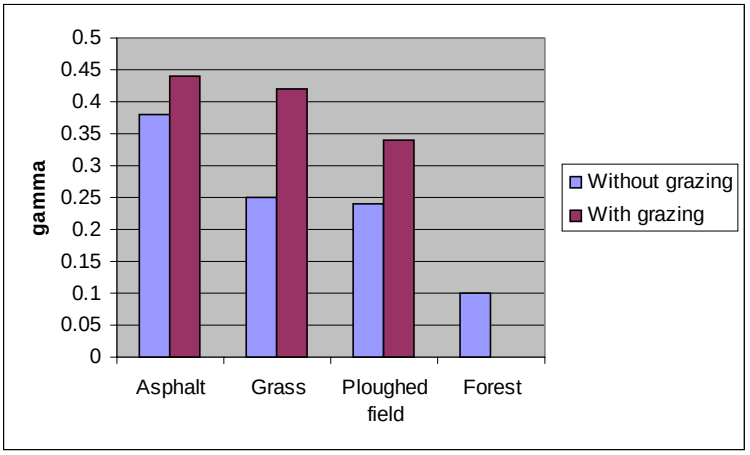

Figure 33. Average values of Γ, with and without the inclusion of the grazing measurements

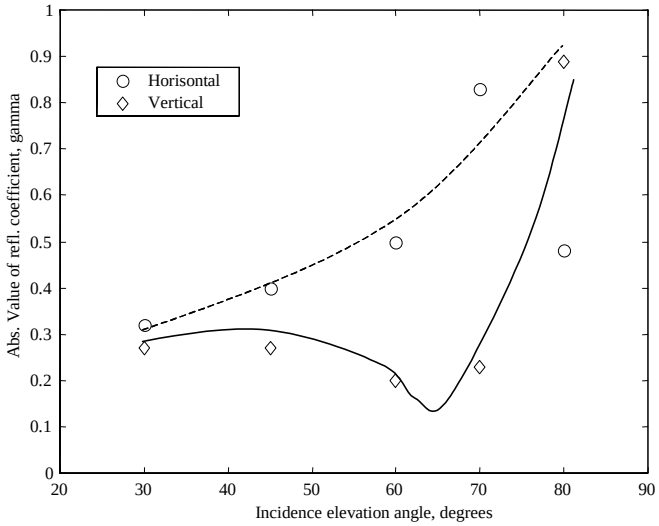

Figure 34. Measured reflection coefficient of asphalt as a function of incidence angle for vertical (diamond) and horizontal (circle) polarisation. The reflection curves are fitted to the measurement values for vertical (solid) and horizontal (dashed) polarisation

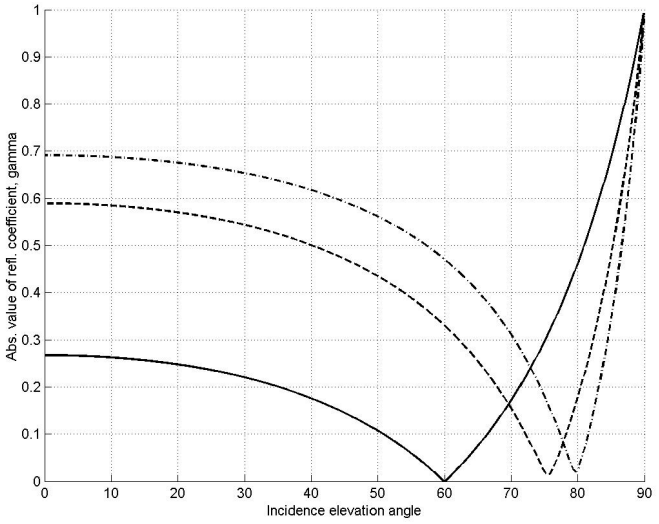

Figure 35. Theoretical reflection coefficient as a function of incidence angle for vertical polarisation in the case of very dry soil (ε_r'=3, σ=0.8e-3, solid), moderately dry soil (ε_r'=15, σ=0.1, dashed) and humid soil (ε_r'=30, σ=0.3, dashdot),

URN:NBN:no-1290

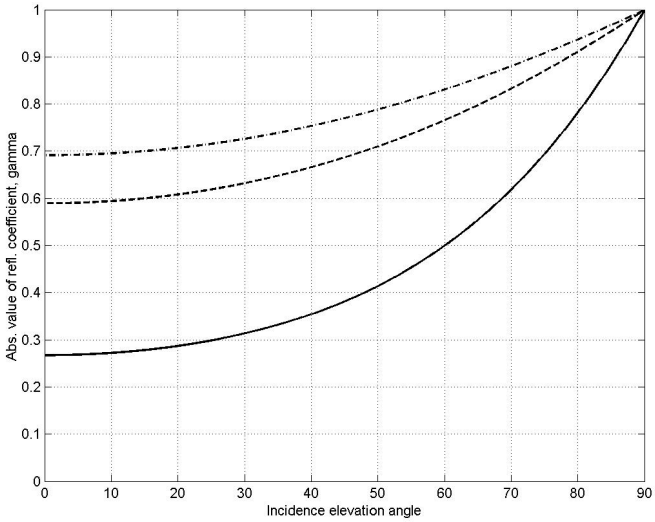

Figure 36. Theoretical reflection coefficient as a function of incidence angle for horizontal polarisation in the case of very dry soil (ε_r'=3, σ=0.8e-3, solid), moderately dry soil (ε_r'=15, σ=0.1, dashed) and humid soil (ε_r'=30, σ=0.3, dashdot)

5.3.3 Seasonal and weather variations

Radio planning tools do not take into account meteorological conditions, for example soil moisture or snow cover. This is justified by their overall limited accuracy. The 3D channel model will allow a better prediction, and meteorological conditions may be of influence. Measurements under different conditions were undertaken to verify and quantify the effect.

Water on the surface did not increase the Γ for asphalt, but did increase the reflection coefficient significantly for grass. For an incidence angle of 45° the increase of the reflection coefficient was from 0.19 to 0.35 for horizontal polarisation and from 0.23 to 0.53 for vertical polarisation. The physical explanation of these measured results is the higher absorption of water on asphalt, whereas in the case of grass the water increases the conductivity of the surface, thus reducing the apparent roughness and increasing reflection.

The measured numbers are compared with the theoretical curves of Figure 35. For vertical polarisation, at an incidence angle of 45°, Γ increases from approximately 0.15 to approximately 0.60 for humid soil compared to very dry soil. Figure 36 shows that for horizontal polarisation an increase from approximately 0.40 to approximately 0.75 for humid soil compared to very dry soil is observed for an incidence angle of 45°.

Snow reduced the apparent roughness of the ploughed field significantly, from a height variation of 100 mm on average without snow to a height variation of 42 mm with wet snow present. The majority of the power was observed in the coherent part with snow on the surface, as opposed to the case without snow. The Γ increased significantly in the case of snow compared with the case of no snow.

URN:NBN:no-1290

These results show that weather and seasonal changes will significantly alter the scattering properties of the surface, providing the need for channel models to take these variations into account. This is discussed further in Chapter 7.

5.3.4 Other considerations

It should be noted that although there was a significant coherent part also for ploughed field, the maximum received power was observed at a lower scattering elevation angle than the specular one, reflecting the *sawtooth* geometry of the surface. This is illustrated in Figure 37, which shows an example of received power in the case of ploughed field without snow, vertical polarisation. Although the incidence angle was 50°, the maximum received power was observed at 30°. This shows that the specific surface is not isotropic (Chapter 4). Measurements performed from other incidence angles provide similar results, i.e. varying scattering angles depending on the direction of observation.

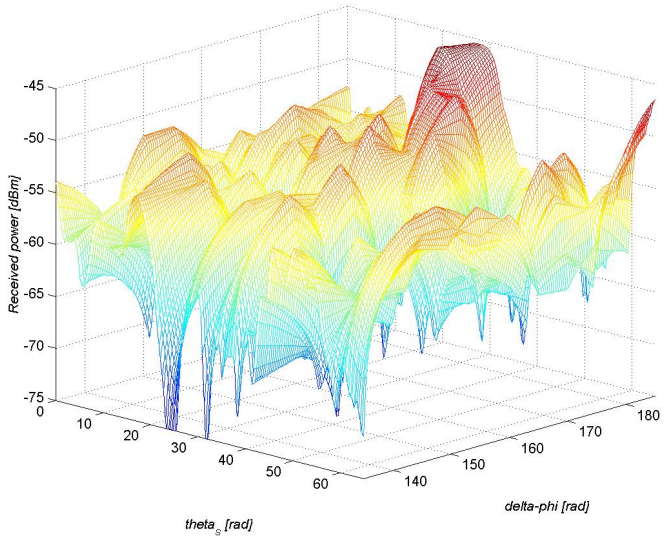

Figure 37. Received power as a function of receiving angles in the case of vertical polarisation, ploughed field, incidence elevation angle 50º. Note that maximum received power is at approximately 30º.

5.3.5 Conclusions

An analysis of the measurement results from rough surface scattering was performed, showing a very good agreement with theoretical considerations. The measurements provide reflection coefficients and equivalent surface height variation for the natural surfaces asphalt, grass, ploughed field and forest. The main results from the analysis were:

- The equivalent surface height variations are typically 10 mm for asphalt, 25 mm for grass, 100 mm for ploughed field and 500 mm for forest.

- The estimated reflection coefficients were in good agreement with the values reported in the literature for dry surfaces.
- Water on asphalt did not change the reflection coefficient significantly, but increased Γ by up to 50 % on grass.
- Snow on the ploughed field reduced the apparent roughness by more than 50 % and increased the reflection coefficient significantly.

6 Evaluation of scattering characteristics for 3D radio channel modeling

In this chapter the measurements described in Chapter 5 are used together with the A/P model for 3D predictions and compared with other models. Four alternative models were tested, they are all currently used in 3D radio channel prediction models and are described in Chapter 4. The first model was the plane surface model, assuming that the surface can be characterised by only one parameter, the reflection coefficient Γ. The second model was the Small perturbation method (SPM), which is able to describe scattering with both coherent and diffuse components. The third model was the Kirchoff model, also able to describe the coherent as well as the diffuse component. The fourth model was the Oren model, which is a rough surface model, assuming that the scattering is completely diffuse. All these performance comparisons were done for asphalt, grass and agriculture field under dry conditions. The results in terms of closeness to fit are given as values in dB relative to the A/P model.

6.1 Plane surface model

This model assumes that the surface is plane and uniform and that scattering can be characterised by using ray optics. Therefore the surface can be characterised by only one parameter, the reflection coefficient Γ, which was assumed to be uniform over the surface.

The optimum Γ for each measurement series was found using a minimum square error optimisation, defined as

$$[\Gamma]_{opt} = \min_{[\Gamma]} \sum_{\theta_S} \sum_{\Delta\phi} \left(\tilde{\rho}(\theta_S, \Delta\phi) - E_\rho(\theta_S, \Delta\phi)\right)^2 \qquad \textit{(eq. 111)}$$

where $\tilde{\rho}$ was the measured amplitude in each direction, and E_ρ was the amplitude resulting from the model assumptions and the current value of Γ.

All the results from the analysis of all the measurement series are tabulated in Appendix F, giving the optimum parameter for each measurement series as well as the mean square error relative to the *amplitude/phase model* analysis, described in Chapter 5.

Figure 38 shows the mean of the mean square errors relative to the A/P model for each surface type. For all the measurements the amplitude/phase model shows a closer fit. However, the plane surface model fit was reasonably good for asphalt, with an error that was only 1.1 dB higher on average. As expected, the fit became progressively worse with the roughness, for ploughed field the average error was in the order of 5-6 dB higher than for the amplitude/phase model.

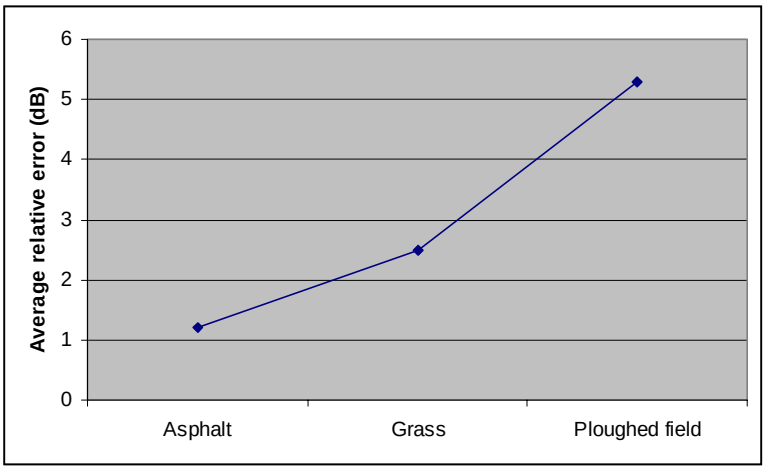

Figure 38. Average error (dB) of the plane surface model relative to amplitude/phase model for different natural surfaces

For asphalt the estimated values of Γ were in very good agreement with Γ derived from the A/P model, the difference being only 0.03 on the average. For grass the value of Γ was considerable underestimated, by 20 % on average, and by more than 50 % underestimated in the case of ploughed field. This confirms that the plane surface model is only usable for smooth surfaces, and in this case only asphalt.

6.2 Small Perturbation method

The Small Perturbation Method (SPM) is described in detail in Chapter 4. In the optimisation first order SPM was used. The coherent field was calculated as described in Chapter 4, and the Fresnel reflection coefficients were assumed constant over the surface. The surface electromagnetic parameters were assumed known, and taken from literature. The values used were ε_r'=8, σ=0.01 for asphalt and ε_r'=8, σ=0.005 for grass and ploughed field (values from [Lebherz92]). The optimisation was performed based on finding the optimum values for *L* and *h* in the least square sense, where *L* and *h* are the surface correlation length and rms height variation (relative to the wavelength), respectively, assuming Gaussian surface statistics. This can be written

$$\begin{bmatrix} L & h \end{bmatrix}_{opt} = \min_{\begin{bmatrix} L & h \end{bmatrix}} \sum_{\theta_s} \sum_{\Delta\phi} \left(\tilde{\rho}(\theta_s, \Delta\phi) - E_\rho(\theta_s, \Delta\phi) \right)^2 \qquad \textit{(eq. 112)}$$

where $\tilde{\rho}$ was the measured amplitude in each direction, and E_ρ was the expectation value of the SPM amplitude given the current values of $\begin{bmatrix} L & h \end{bmatrix}$ and the surface electromagnetic properties.

The full results from the analysis of all the measurement series are tabulated in Appendix F, giving the optimum parameters for each measurement series as well as the mean square error relative to the *amplitude/phase model* analysis, described in Chapter 5. It was seen that the SPM model showed poor performance on all surfaces, ranging from 7 dB on average for

asphalt to 12 dB on average for ploughed field. This was considerable poorer than the other methods, even on the smoothest surfaces. Closer inspection showed that this was due to the electromagnetic parameters used pointing to a higher reflection coefficient than the ones observed. This will give severe errors for SPM due to first order SPM not conserving energy, estimating the coherent component to be equal to the one from a smooth surface with the electromagnetic properties assumed. Therefore the optimisation in the case of SPM was repeated using electromagnetic parameters in line with the values estimated from the optimisation using the A/P model in Chapter 5. The values used in this case were; asphalt: ε_r'=3.1, σ=0.01; grass: ε_r'=1.8, σ=0.05; ploughed field: ε_r'=1.8, σ=0.05. Both the results using the original values and using the refitted values are tabulated in Appendix F.

Figure 39 shows the average error (dB) relative to the amplitude/phase model for different surfaces for the refitted values. The tendency is towards poorer performance with increasing roughness, as expected since the SPM assumptions (Chapter 4) are no longer valid for rough surfaces. Also note that the error in the case of asphalt is approximately the same as that of the plane surface model.

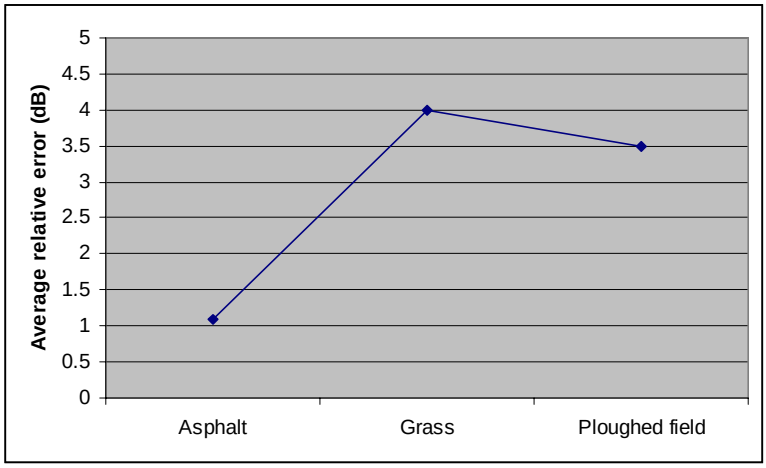

Figure 39. Average error (dB) of the Small Perturbation Method (SPM) relative to amplitude/phase model for different natural surfaces, refitted electromagnetic parameters

The optimisation overestimated the rms height variation for all surfaces, as shown in the results in Appendix F. The variation between series was quite large.

6.3 Kirchoff model

The Kirchoff model is described in detail in Chapter 4. In the optimisation the rough surface expressions are used for the diffuse field. The coherent field was calculated as described in Chapter 4, and the Fresnel reflection coefficients were assumed constant over the surface. The surface electromagnetic parameters were assumed known, and taken from literature. The values used were ε_r'=8, σ=0.01 for asphalt and ε_r'=8, σ=0.005 for grass and ploughed field (values from [Lebherz92]). The optimisation was performed based on a least square fit for the optimum values of *L* and *h*, where *L* and *h* are the surface correlation length and rms height variation

(relative to the wavelength), respectively, assuming Gaussian surface statistics. This can be written

$$\begin{bmatrix} L & h \end{bmatrix}_{opt} = \min_{\begin{bmatrix} L & h \end{bmatrix}} \sum_{\theta_s} \sum_{\Delta\phi} \left(\tilde{\rho}(\theta_s, \Delta\phi) - E_\rho(\theta_s, \Delta\phi) \right)^2 \qquad \textit{(eq. 113)}$$

where $\tilde{\rho}$ was the measured amplitude in each direction, and E_ρ was the expectation value of the Kirchoff amplitude given the current values of $\begin{bmatrix} L & h \end{bmatrix}$ and the surface electromagnetic properties.

The full results from the analysis of all the measurement series are tabulated in Appendix F, giving the optimum parameter for each measurement series as well as the mean square error relative to the *amplitude/phase model* analysis. Figure 40 shows the average error (dB) relative to the amplitude/phase model for different surfaces. It can be noted that the Kirchoff model showed poorer performance on all surfaces. The worst fit was found in the case of ploughed field, which was slightly surprising, since the rough surface description of the Kirchoff model that was used would be expected to perform best for the roughest surface. One reason could be the assumption of an isotropic surface in the Kirchoff model, which is not satisfied for the ploughed field.

The estimation of the correlation length L showed quite large variations, the highest values for L were observed in the case of ploughed field.

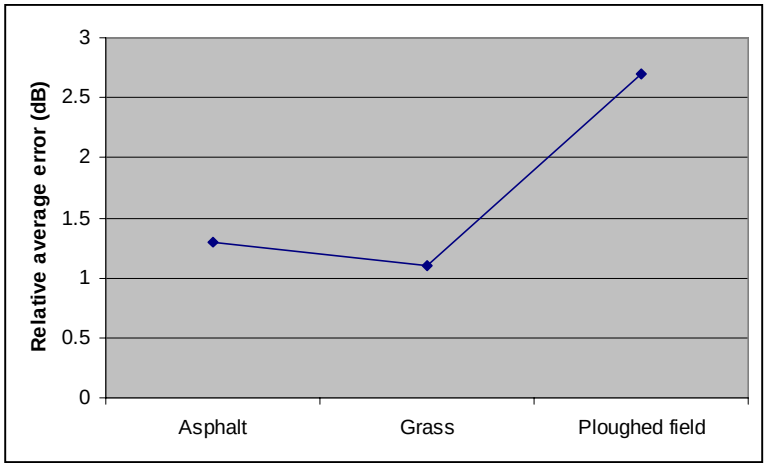

Figure 40. Average error (dB) of the Kirchoff model relative to amplitude/phase model for different natural surfaces

The optimisation seems to overestimate the rms height variation, especially for asphalt where the estimated *h* is 2 cm, which is considerable more than the value from the estimation in Chapter 5. Closer inspection showed that like in the case of SPM this was due to the electromagnetic parameters used pointing to a higher reflection coefficient than the ones observed. This lead the optimisation to compensate by estimating a slightly rougher surface. The lower reflection coefficient indicates that the permittivities of the surfaces were slightly

lower than the ones used in the optimisation. Also for the Kirchoff model the estimation was repeated using values for the electromagnetic parameters in line with the values estimated from the optimisation using the A/P model in Chapter 5. The values used in this case were the same as in the SPM case: asphalt: ε_r'=3.1, σ=0.01; grass: ε_r'=1.8, σ=0.05; ploughed field: ε_r'=1.8, σ=0.05. Both the results using the original values and using the refitted values are tabulated in Appendix F. However, unlike in SMP case, for the Kirchoff model, the refitted values did not show a better fit than the original data. The variations in the values of the parameter estimations were still quite large, and the height variations were still somewhat overestimated.

6.4 Oren model

This model is described in Chapter 4 and is a model that assumes a rough surface and no coherent, reflected component. The output is always a normalised radar cross section σ^0, meaning that the scattering in any direction is scalable with the size of the surface. In the case of the Oren model this normalised radar cross section can be written $\sigma^0(R,\sigma^2,\theta_s,\theta_i,\Delta\phi)$, where the parameters R and σ^2 are defined in Chapter 4 and the other parameters are geometrical properties. As described in Chapter 2 the received power can according to this description be written as

$$P_r = \iint_A \frac{P_t g_t(\theta_i,\phi_i) g_r(\theta_s,\phi_s)\lambda^2}{(4\pi)^3 R_t^2 R_r^2} \cdot \sigma^0 \cdot dA \qquad \textit{(eq. 114)}$$

where the integral is over the entire illuminated area.

In a similar fashion to the method for the other models, the optimisation was performed by finding the optimum values for R and σ^2 in a minimum square sense. This can be written as

$$\begin{bmatrix} R & \sigma^2 \end{bmatrix}_{opt} = \min_{\begin{bmatrix} R & \sigma^2 \end{bmatrix}} \sum_{\theta_s} \sum_{\Delta\phi} \left(\tilde{\rho}(\theta_s,\Delta\phi) - E_\rho(\theta_s,\Delta\phi) \right)^2 \qquad \textit{(eq. 115)}$$

where $\tilde{\rho}$ was the measured amplitude in each direction, and E_ρ was the expectation value of the Oren amplitude given the current values of $\begin{bmatrix} R & \sigma^2 \end{bmatrix}$.

The full results from the analysis of all the measurement series are tabulated in Appendix F giving the optimum parameters for each measurement series as well as the mean square error relative to the *amplitude/phase model* analysis, described in Chapter 5.

Figure 41 shows the mean of the mean square errors relative to the *amplitude/phase model* for each surface type. In the cases of asphalt and grass the Oren model showed a much poorer fit, 8.7 and 5.8 dB on average, respectively. This is as expected since the coherent component was significant in both these cases. In the case of ploughed field the performance was similar to the amplitude/phase model, about 0.4 dB better. This result was slightly surprising, since measurements indicated a coherent component in the scattering from the ploughed field. Closer inspection showed that the slightly poorer result of the A/P model is due to the anisotropic surface structure of the ploughed field, leading to the coherent component appearing at a

different angle than the mirror angle. As described in Chapter 5, the anisotropy leads the optimisation routine for the amplitude/phase model to fail.

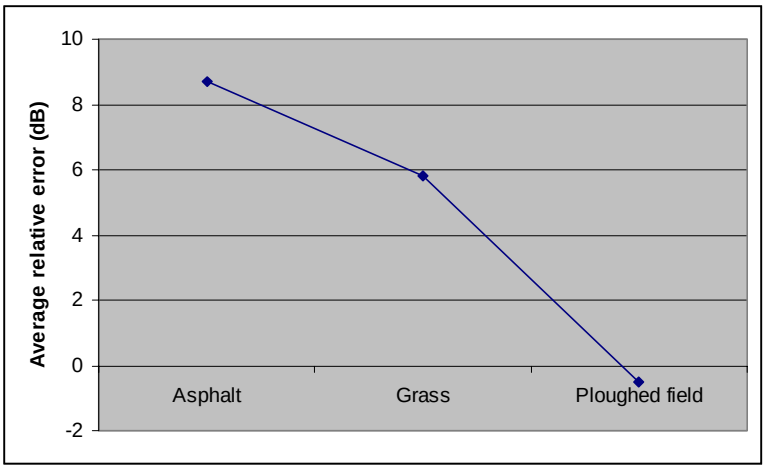

Figure 41. Average error (dB) of the Oren model relative to amplitude/phase model for different natural surfaces

In conclusion the comparison shows that the Oren model is only applicable for very rough surfaces.

6.5 Conclusion

Table 3 shows the average error for the different surfaces and models compared to the amplitude/phase model. The main observations are:

- The amplitude/phase model performs better than the other models on all surfaces,
- the plane surface model performs reasonably good for asphalt, but is not appropriate for rougher surfaces (grass, ploughed field),
- the small perturbation model shows good performance on asphalt, but performed increasingly poorly with roughness,
- the more general Kirchoff model shows an overall better performance, the error being the lowest among the conventional models tested, and
- the rough surface Oren model performs well on ploughed field, but is not applicable for smoother surfaces.

	Asphalt	Grass	Field
Plane surface	1.2	2.5	5.3
SPM[35]	1.1	4.0	3.5
Kirchoff	1.3	1.1	2.7
Oren	8.7	5.8	-0.5

Table 3. Average error (dB) for the different models compared to amplitude/phase model

It could also be noted that although a significant coherent component was observed in the case of ploughed field, the Oren model shows a closer fit to the data than both the amplitude/phase and the Kirchoff model in this case. This is probably due to the anisotropic surface structure of the ploughed field, which caused the Kirchoff and the A/P model to have a wrong estimation of the coherent component.

[35] Values obtained using the measured values for the electromagnetic parameters

7 Applicability and implementation

This chapter describes the implementation and applicability issues regarding 3D channel modeling using the 3D radar model described in Chapter 3. The first section provides a brief discussion about applicability issues. The second section gives an overview of the implementation, including rough surface scattering. In the third section the parameterisation is discussed. Section four describes the enhancements suggested to this type of modeling. Two elements are suggested, the estimation of a prediction interval rather than a single value, and the use of the A/P scattering model as suggested in Chapter 5. The fifth section provides a sensitivity analysis, including variations between area types, land use classes, variations in model parameters as well as weather and seasonal variations. The sixth section provides a discussion about the applicability of the model in comparison with other models. The last section contains suggestions for future work.

7.1 Applicability

The suggested 3D channel model is principally applicable to rural or suburban areas. This is because of an implementation with first order reflection/scattering only, which is reasonable when considering scattering from natural surfaces. In suburban areas reflection/scattering from man-made objects like buildings will provide a significant contribution. In urban areas multiple reflection/scattering from building walls will have a significant contribution to the total received signal, making first order reflections insufficient.

As discussed in Section 7.6, the model can be seen as a *generalized ray-tracing model* if multiple reflection/scattering is taken into acount. This is because the A/P scattering model is not limited to natural rough surfaces, but can equally well be applied to e.g. building walls. It is believed that the inclusion of a more accurate scattering model will have increased importance with increased map accuracy.

7.2 Implementation

7.2.1 Sub-models

As discussed earlier the 3D channel model is based on predicting the sum of a *2D vertical plane component* and a number of *3D scattered components*. The 2D component can be either free space or diffracted. The scattered components can be from surfaces with free space to the transmitter and receiver, or from surfaces visible to transmitter and receiver via a diffraction link only, which leads these components to be *diffracted-scattered*, *scattered-diffracted* or *diffracted-scattered-diffracted*.

With respect to the 3D channel model, three submodels are required; 1) the 2D vertical Tx-Rx-plane model, 2) the diffraction model to and from scattering surfaces, 3) the scattering/reflection model. The discussion in this report is concerned with the scattering/reflection model. The other two submodels require a deterministic or semi-deterministic narrowband model, where suggestions are described in Chapter 3. The third model should be the amplitude/phase model described in Chapter 5.

No details about the implementation of the first two types of models will be provided here. They will either be a two-dimensional fullwave solution or a model based on diffraction theory. Due to complexity, fullwave solutions will normally not be a viable option for model type 2.

Rather a simple diffraction based model will be used or even an *on/off model*[36]. For model type 1 a fullwave solution will normally be preferred due to its superior accuracy.

7.2.2 Scattering/reflection model

This study concentrates on the inclusion of 3D scattering effects, identified as submodel 3. The implementation is described below.

In the algorithm the surface is characterised using three input parameters:

- The smooth surface (Fresnel) reflection coefficient described in Chapter 2, which is incidence angle dependant and can be written as $\Gamma_p(\theta_i, \varepsilon_r)$ where *p* indicate the incidence polarisation (*v* or *h*) and ε_r is the complex relative permittivity (Chapter 2), and θ_i is the incidence elevation angle.
- The root-mean-square height variation of the surface, h_{rms}.
- The physical size of the surface, A.

In addition the algorithm requires the angles θ_i, θ_s and $\Delta\phi$, which define the geometry of the incidence and scattered waves.

In accordance with the discussion in Chapter 5 the output should be divided into two contributions; the *specular reflection* and the *diffuse scattering*:

1. The specular reflection can most conveniently be described by using a *resulting reflection coefficient* which can be written as

$$\Gamma_{res} = c_s \cdot \Gamma \qquad \textit{(eq. 116)}$$

   where Γ is the smooth surface reflection coefficient as described aboved and c_s is a constant between 0 (completely rough surface) and 1 (smooth surface). This is described in Chapter 5.

   This description of a resulting reflection coefficient was also used in e.g. [Landron93] and [DegliEsposti99]. For large surfaces (larger than the first Fresnel zone, Chapter 2), the specular reflection has contribution only in the mirror reflection direction ($[\theta_i = \theta_s, \Delta\phi = \pi]$). This is the assumption that is normally used in Ray-tracing predictions (Chapter 3).

   For surfaces that cannot be assumed large with respect to the wavelength a different method must be used, e.g. *physical optics*. To use this method the shape of the surface as well as the size must be known. For square surfaces examples of solutions are given in Chapter 2. For large, smooth surfaces *physical optics* provides excellent results [Balanis89]. Care should be taken in the use of the size dependant version of the surface reflections in the case of natural surfaces, however. The edge effect inherent in this description must be due to the real size of the surface and not the map resolution. In the latter case the resulting coherent field may be erroneously predicted due to the assumption

[36] The contribution is zero if the surface is not in line-of-sight and is calculated from free-space loss if it is in line-of-sight.

of random phase between neighbouring surfaces. When the surface is a man-made object, like a building wall, the edge effects must be taken into account.

Most surfaces contributing in rural area will appear large from the definition above, therefore only the large surface approximation is currently implemented.

2. The diffuse scattering is described by its normalised bistatic radar cross section as described in Chapter 2.

   Unlike the specular component the diffuse component is always proportional to the surface size, so that the total radar cross-section is

$$\sigma = \sigma^0 \cdot A. \qquad \textit{(eq. 117)}$$

3. If a polarisation dependant description is desired the total contribution in any direction can be decomposed into the co-polar and the cross-polar components using the method described in Chapter 5.

The scattering/reflection algorithm described here makes no assumption about the degree of roughness and is therefore equally suited to describe all surfaces.

7.3 Parameterisation

In a real radio planning scenario the starting point is a digital elevation map as well as a classification with division into land usage classes with corresponding model parameters. The information should cover potential scattering parameters of that surface, i.e. roughness and permittivity. Depending on these parameters the surface has a variable scattering characteristics, and for simplicity reasons only the minimum and maximum values, denoted as *high-scatter case* and *low-scatter case*, are used. This is to account for the seasonal or weather variations. For most natural surfaces dry conditions would be a high-scatter case, whereas wet or snowy conditions would be a low-scatter case, as shown in Chapter 5.

The parameters required for each surface type are the rms height variation h_{rms} and the electromagnetic parameters ε_r‘ and σ, from which the angle dependant Fresnel reflection coefficient Γ can be calculated.

Parameterisation has to do with 1) Division of the surfaces into a number of *land usage classes* and 2) Decision of the parameters for each land usage class.

Division into classes

It is not the ambition of this report to suggest a division into classes, as an optimal division will vary from area to area. However, the two major criteria for deciding the division should be:

1. *Difference in parameters*: Surfaces that have large difference in one or both of the two describing parameters Γ and h_{rms} should be handled differently if possible. From a similar argument it is not critical to make a distinction between land usage classes that have similar describing parameters.
2. *Level of detail in map database*: The underlying map database will have a resolution as well as a land usage division. This is therefore a limitation in the method that is difficult to overcome.

An example of the land usage division used in implemented models is given in e.g. [Lebherz92].

Describing parameters

If, for a particular area the necessary height variation and electromagnetic parameters are not available, some means must be found to get a good estimate of them. In general there are three ways of doing this; 1) by experiments, 2) from literature, 3) performing an *educated guess*.

1. The procedure described in Chapter 5 was developed to estimate the rms height variation h_{rms} and reflection coefficient Γ for a given surface. The algorithm uses power measurement values for different azimuth and elevation scattering angles for a given incident elevation angle θ_i and estimates h_{rms} and $\Gamma(\theta_i)$. h_{rms} is obviously independent of incident angle, whereas Γ is not and therefore only valid for the incident angle measured. However, as discussed in Chapter 2, there is a relationship between Γ, the electromagnetic properties and the incidence angle. Therefore, the electromagnetic properties ε_r' and σ for the surface can be estimated when estimations of Γ for at least two incidence angles are available (preferably more). From these parameters the angle dependant $\Gamma(\theta_i)$,which is necessary for the scattering model, can be calculated.

2. The necessary describing parameters can otherwise be taken from literature. Some sources report figures for electromagnetic parameters for natural surfaces (e.g. [Boithias87]). Bare soil surfaces and their characteristics are covered by radar romote sensing, typically at frequencies 1.2, 5 and 10 GHz [Noll92]. During these campaigns measurements of vegetation covered soil, e.g. grass or potatoes, were taken, but the translation of vegetation parameters into equivalent roughness is barely sound. The discussion on dry and wet grass in Chapter 5 explains the difficulties.

3. When the necessary surface information is not otherwise available, often an *educated guess* would be good enough for 3D channel predictions. In terms of electromagnetic properties, it is advisable to use the value for a similar surface, for which information *is* available. For instance, the experiments described in Chapter 5 show that ploughed field and grass have similar electromagnetic properties, which would be a reasonable assumption in the first place. A different, and probably more difficult evaluation, is the low-scatter and high-scatter division. For instance for *farmland/field* in [Lebherz92] the value for dry conditions is $\varepsilon_r' = 7.0$, which will be the high-scatter case. The low-scatter case will be wet surface or snowy surface, dependent on region. Either of them would have a value for ε_r' somewhere between the value for dry conditions and the value for water ($\varepsilon_r' = 80$). In terms of the height variation an *educated guess* could often be achieved simply by "using a ruler", the experiments in Chapter 5 show that the h_{rms} estimated is similar to the real physical height variations observed on the surface. This is more complicated in the case of layered surfaces, like forest with trees in leaf, which would lead to an *equivalent* h_{rms} for the surface.

7.4 Enhancement to radio planning tools

The enhancements suggested to 3D radio planning are within two areas; 1) the estimation is performed for an interval rather than a single prediction value, and 2) the new A/P scattering model is used. Reasons for using the A/P scattering model are provided earlier (Chapter 5, Chapter 6), and will not be discussed again. This section will concentrate on the suggestion for using a prediction interval.

The idea of performing the propagation prediction in terms of an interval given by knowledge about the probability density function (PDF) was described by Lebherz et.al. in [Lebherz92].

The approach was that the resulting fieldstrength could be seen as the sum of a large number of scattered and diffracted components from which the PDF was known.

As previously discussed, in the model type in question the total predicted fieldstrength can be seen as a sum of complex contributions which can be written

$$\mathbf{E}_{total} = \sum_{i=1}^{N} \mathbf{E}_i \qquad \textit{(eq. 118)}$$

where $\mathbf{E}_i$ are the contributions from the *n* scattered or diffracted components and the vector notation indicate that all contributions are complex. The PDF of the contributions $\mathbf{E}_i$ can be written $f_i(\mathbf{k}_i)$ where $\mathbf{k}_i$ is defined as

$$\mathbf{k}_i = \left[\mathrm{Re}\{\mathbf{E}_i\} \quad \mathrm{Im}\{\mathbf{E}_i\}\right] = \left[k_1 \quad k_2\right] \qquad \textit{(eq. 119)}$$

The characteristic function of the individual signal components is defined as

$$\varphi_i(\mathbf{t}) = \int_{-\infty}^{\infty}\int f_i(\mathbf{x}_i) e^{j\mathbf{tk}} dk_1 dk_2 \qquad \textit{(eq. 120)}$$

where $\mathbf{t} = \left[t_1 \quad t_2\right]$.

The total characteristic function can then be written

$$\varphi_{total}(\mathbf{t}) = \prod_{i=1}^{n} \varphi_i(\mathbf{t}) \qquad \textit{(eq. 121)}$$

and from this the total PDF can be found using inverse Fourier tranform

$$f_{total}(\mathbf{x}) = \int_{-\infty}^{\infty}\int \varphi_{total}(\mathbf{t}) e^{-j\mathbf{tx}} dt_1 dt_2 \qquad \textit{(eq. 122)}$$

In the discussion in Chapter 5 it was shown that the PDF of the scattered components are Rayleigh or Rice dependent on whether there is a significant coherent component or not. The phase can be considered uniformly distributed over 2π.

Examples of PDF plots from one of the test cases described in the next section (Bristol) are shown in Figure 42 for a) a line-of-sight case, b) a case with the 2D component attenuated 20 dB (relative to a)) and c) a case with the 2D component attenuated 40 dB.

Figure 43 shows 2D plots of the same cases as in Figure 42 b) and c). The curve indicates the 3 dB contour in each case. The value σ indicates the width of the distribution. The centre of the curve is in a distance R from the origin in the complex plane. Note that due to the uniform phase the shape of the contour is circular. Also, because the 2D component is assumed non-random, the shape of the curve is solely due to the 3D component and is equal in the two cases.

The ratio R^2/σ^2 is proportional to the Ricean K-factor (Chapter 5). In the case of the 40 dB attenuated 2D component, R is neglectable and therefore not visible in the Figure.

When using the *low scatter* and *high scatter* cases one obtains two separate PDFs, and either one of them or a *combined* PDF should be used. This combined PDF can be found by using the same method described above to find the PDF of the *sum* of the high scatter and low scatter cases. The average is then simply the PDF of the sum divided by two. It is suggested to allow the planning tool to make both the low-scatter and high-scatter predictions, the usage will decide which one should be used. Results from the low-scatter and high-scatter cases can be used in the radio planning tools to obtain *worst case - best case* estimations. Which cases that are worst and best will depend on the parameters in question: High values for the reflected signal components will increase the estimated received signal level, whereas it will also increase the time dispersion, which is often undesirable.

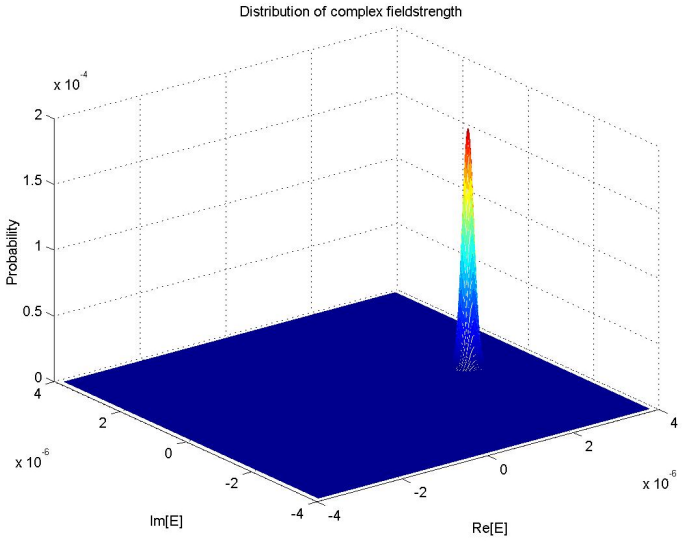

a)

Figure 42. Example complex pdf-s for the received signal from test case Bristol, a) LOS, b) 2D component attenuated 20 dB, c) 2D component attenuated 40 dB.

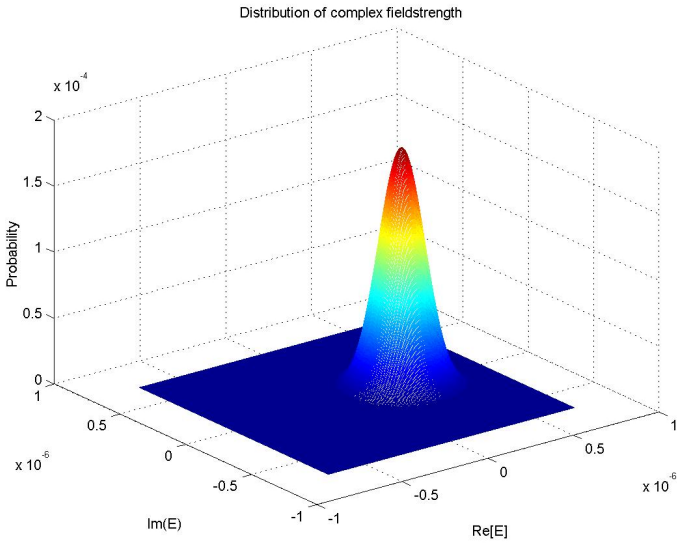

b)

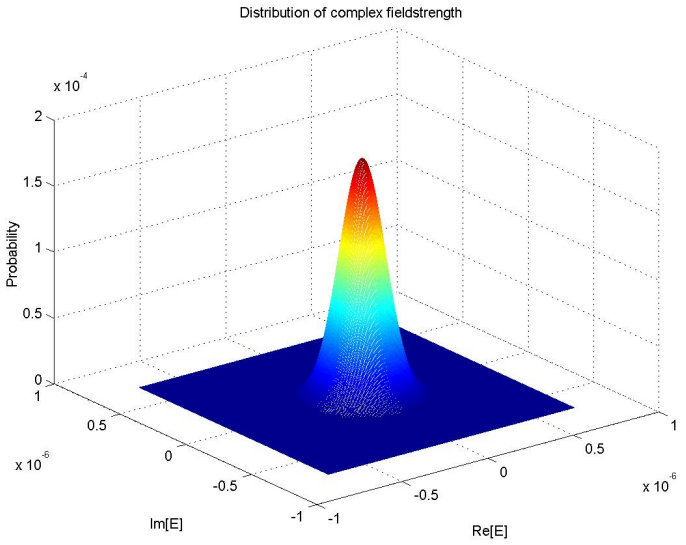

c)

Figure 42. Example complex pdf-s for the received signal from test case Bristol, a) LOS, b) 2D component attenuated 20 dB, c) 2D component attenuated 40 dB.

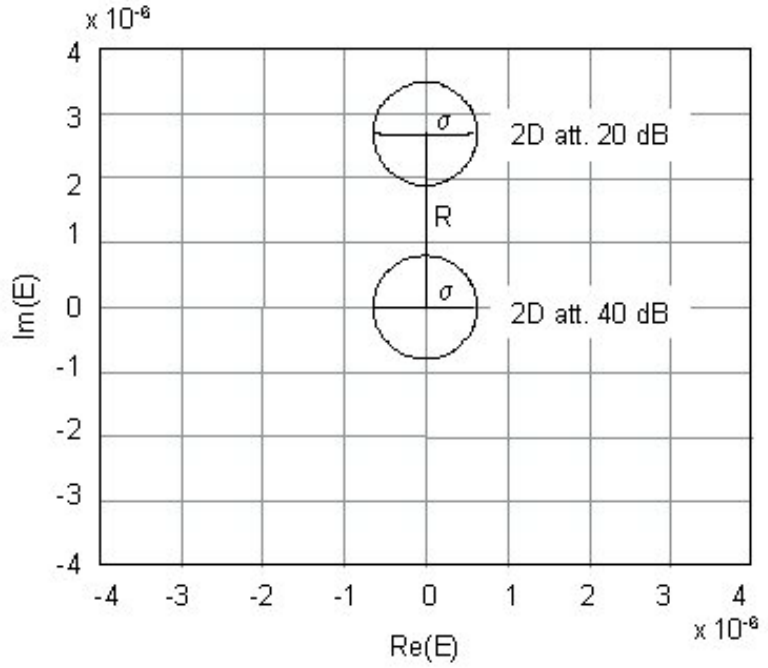

Figure 43. 2D plot showing R, the distance from origin, and the 3 dB contour for the curves plotted in 3D in Figure 42 b) and c)

7.5 Sensitivity analysis

This section performs a sensitivity analysis from a number of example scenarios. They are based on using surface height information from a given area obtained from digital elevation maps. The example scenarios were then chosen by selecting typical mobile and base station positions and calculating the radio channel using the 3D channel model with scattering contributions from the A/P model.

The received signal consisted of two types of components; 1) a 2D vertical plane component that is assumed non-random with any value from the free space value to zero; 2) a 3D component due to the field scattered from terrain surfaces. In the latter component only the terrain surfaces with line-of-sight to both the base station and the mobile station were taken into account.

For clarity the terrain was assumed to be uniform in each run of the calculations. The terrain types considered were forest, field and grass. The parameters used in each case were taken from the experiments described in Chapter 5 and are given in Table 4. The calculations were done for downlink, with the base station transmitting and the mobile station receiving. The calculations were performed for different seasonal and weather conditions. In particular, for field with and without snow, and for wet and dry grass. Lastly, calculations were performed with varying values for the model parameters. Note that the Tx power value is given as an EIRP value, and assumes a Tx power of 10 W (40 dBm) and an antenna gain of 10 dBi on average.

The example DEMs were from Bristol, UK and Lillehammer, Norway. In Bristol the map covered a rural area with undulating terrain. The map from Lillehammer was from a hilly terrain with a steep valley. Surface plots from the two terrain examples are shown in Figure 44 a) and b).

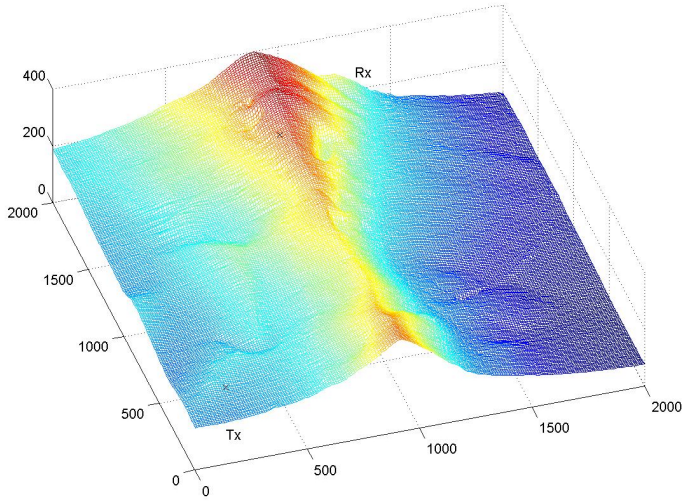

a)

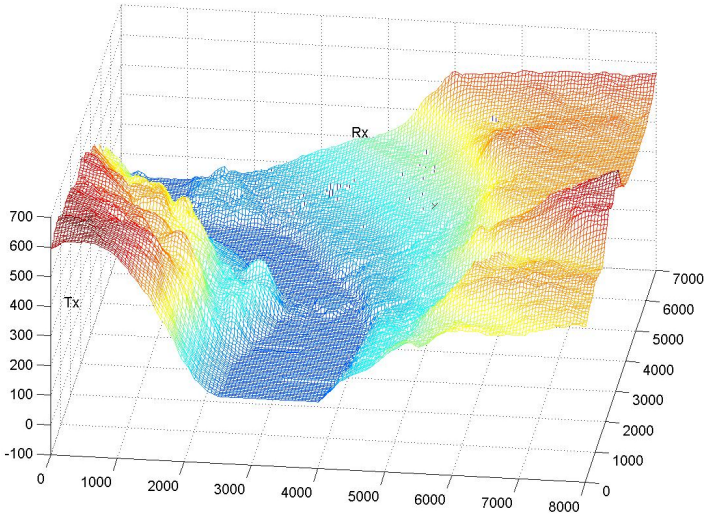

b)

Figure 44. Example surface plots from the test cases in a) Bristol, UK and b) Lillehammer, Norway.

URN:NBN:no-1290

There are distinct differences in the terrain statistics between the two areas. As shown later, in Subsection 7.5.4, the time dispersion is much more severe in the Lillehammer case, due to a number of distant scatterers contributing strongly to the 3D component. Table 5 shows the percentage of the coverage area where the 2D component is line-of-sight, obstructed line-of-sight and blocked, respectively. Two base station antenna heights are used; 20 m (high) and 10 m (low). The division between obstructed and blocked is defined as the *Fresnel-Kirchoff diffraction parameter* v (Chapter 2) exceeding 1.15 for the most severe obstruction on the specific path. This indicates a 2D attenuation of approximately 15 dB compared to free space (knife edge, [Boithias87]). As shown in the next section, for a 2D attenuation of more than 15 dB a 3D model is necessary. The percentage of the area giving a blocked 2D component is significantly higher in the hilly terrain, around 40% compared to approximately 15% in rural undulating.

	Delta height (m)	ε_r	σ
Forest	0.53	1.2	0.001
Field, dry	0.10	7	0.005
Field, snowy	0.042	20	0.010
Grass, dry	0.025	7	0.005
Grass, wet	0.025	20	0.010

Table 4. Parameters used for the different land usage examples in the test cases

2D condition	**Bristol**		**Lillehammer**	
	High Tx	**Low Tx**	**High Tx**	**Low Tx**
LOS	74.1	67.5	50.2	46.4
Obstructed	11.6	13.8	7.9	8.9
Blocked	14.3	18.7	41.9	44.7

Table 5. Percentage of area where the 2D component is line-of-sight, obstructed line-of-sight and blocked for Bristol and Lillehammer

The parameters used in the test cases are listed in Table 6. A *test case* is defined as a combination of 1) Tx- and Rx-positions 2) Value of 2D component and 3) Land usage.

Land Usage	Forest, Field, Grass
Area Type	Rural Undulating (Bristol), Rural Hilly (Lillehammer)
Frequency	2 GHz
Polarisation	Vertical on both Rx and Tx
Tx power (EIRP)	50 dBm
Antenna Diagram	Omnidirectional on both Rx and Tx
Tx-Rx-distance	1500 m (Bristol), 6400 m (Lillehammer)
Tx-height	20 m
Rx-height	2 m

Table 6. List of parameters used in the test cases.

In each test case the complex probability function of the received signal was calculated in the manner described in Section 7.4. From this the cumulative distribution function for the received power is calculated. All results of this section are tabulated in Appendix G. The 1, 5, 10, 50, 90, 95 and 99 percentiles for each case are given along with the mean power and the value of the 2D component. The variations in the received signal level correspond to the short-term fading as described in Chapter 3.

7.5.1 2D versus 3D comparison

As discussed in Chapter 1, in order to predict the time dispersion and angular dispersion in the radio channel a 3D component must be included. In Chapter 3 a number of investigations are described which conclude that in many cases a 3D model provided much higher accuracy for path loss prediction than 2D models in rural areas. Tables 38-43 in Appendix G show the results from the analysis in the case of forest, field and grass for values of the 2D component from 0 dB attenuation (free space) up to 50 dB.

For the line-of-sight cases the inclusion of the 3D model does not provide any significant additional information. The average path loss is not affected by the 3D contribution and even the 1 percentile does not differ significantly from the mean in most cases. The mean value remains relatively constant for values of the 2D component attenuation up to typically 15 dB. In Figure 45 the difference in mean value (dB) between the 2D and 3D predictions are illustrated for the test case Bristol with land use forest for different values of the 2D component. Figure 46 shows a similar curve for Lillehammer with land use grass. In the Lillehammer case the curve increased later, indicating that the 2D prediction is sufficient up to an attenuation of approximately 25 dB in this case. For field and forest these curves for Lillehammer increased earlier, for forest the mean in the 2D and 3D cases remained relatively equal up to approximately 10 dB.

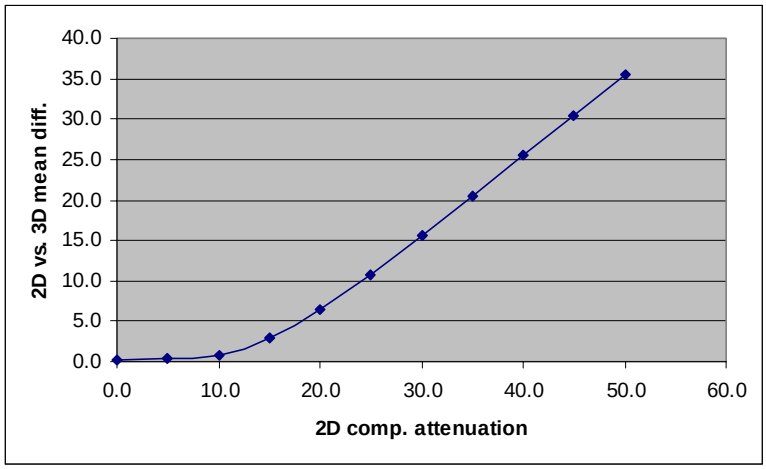

Figure 45. Difference in mean value between the 2D and the 2D+3D prediction for the test case from Bristol, land use forest

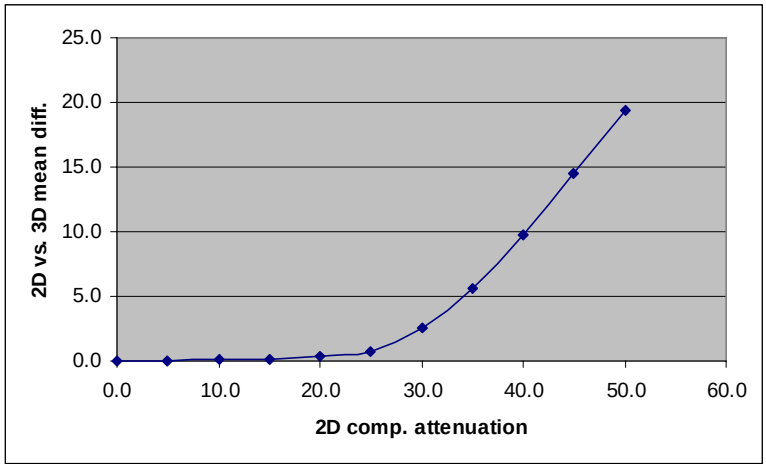

Figure 46. Difference in mean value between the 2D and the 2D+3D prediction for the test case from Lillehammer, land use grass

Although the mean value remained constant, the difference for small percentiles became significant from around 5-10 dB attenuation. For instance, in the case of Bristol with land use forest, the difference between the 50 percentile and the 1 percentile increased from 7 dB for 5 dB attenuation up to 18 dB for 20 dB attenuation. In Figure 47 the cumulative distribution of received signal level for test case Lillehammer with land use grass is shown for 2D component attenuation 0, 10, 20 and 30 dB, normalised to the 50 percentile in each case.

URN:NBN:no-1290

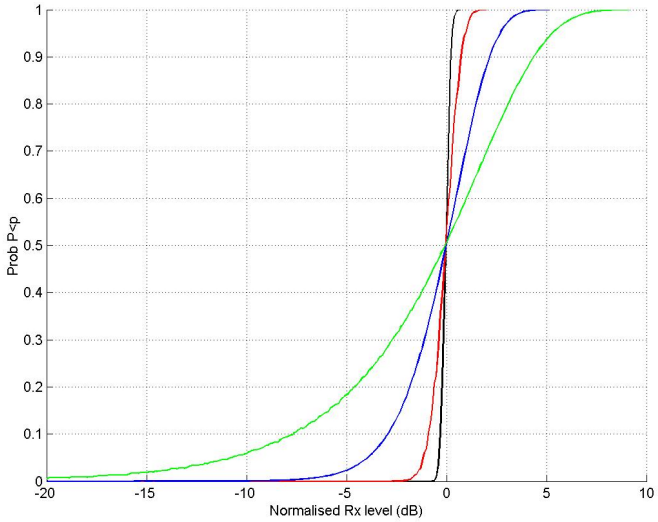

Figure 47. Normalised (to the 50 percentile) cumulative distribution function for test case Lillehammer, land use grass, 2D component attenuation 0 dB (black), 10 dB (red), 20 dB (blue) and 30 dB (green)

The analysis shows further that the 3D scattering dominated the total contribution if the 2D component is attenuated by 20 to 35 dB. In these cases the usage of only a 2D model will give erroneous results.

When comparing the results for the different land use cases, it can be noted that the cases of field and forest provide quite equal results for the test case Bristol. The forest case has the largest number of significant scattering components due to this terrain type having the most severe roughness. However, since the land use field has the highest values for the reflection coefficient this case experienced the highest values for individual scattering contributions. In the case of grass the roughness was lowest, therefore the 3D scattering contribution was less in this case. The mean value for the 3D component was approximately 7 dB lower for grass than for field and forest.

For test case Lillehammer, the difference was much larger between the land use cases, for the 3D component the forest case gave values almost 10 dB higher than a field land usage, which again was about 10 dB higher than grass. This large difference between forest and field can be understood by inspecting Figure 48, which shows radar cross-section for forest (solid) and field (dashed) for different incidence angles. For Lillehammer a large number of distant scatterers relatively far away from both Tx and Rx with grazing incidence and scattering angles have an important impact. Figure 48 shows that for these scatterers forest contribute significantly more due to the difference in roughness. In Bristol a larger part of the contribution came from scatterers relatively close to either Tx or Rx and with lower incidence and scattering angles.

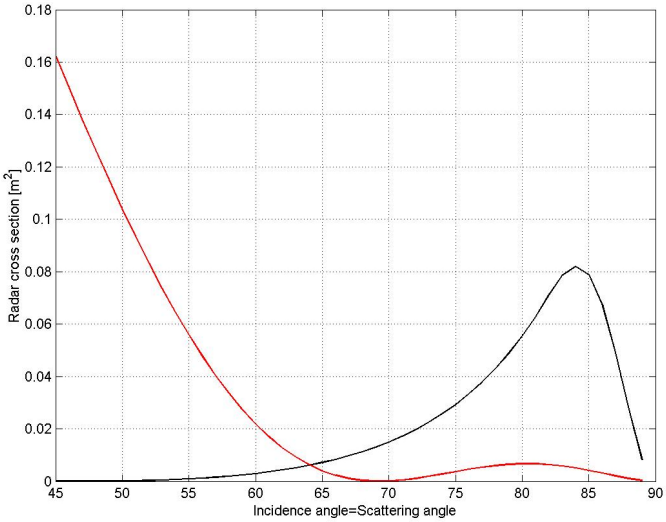

Figure 48. Radar cross-section for a 1 1 m surface of forest (black) and field (red) for incidence angles from 45º to 89º. Scattering angle is assumed equal to incidence angle

Figure 49 shows the cdf for the test case Lillehammer in the case of forest, field and grass, respectively, for the 3D component only. The large difference between the land use cases should be noted. In this example the land cover forest and field would provide sufficient signal level for e.g. GSM to operate satisfactorily, whereas grass would experience problems in approximately 10% of the time[37].

[37] The sensitivity limit for GSM is –102 dBm.

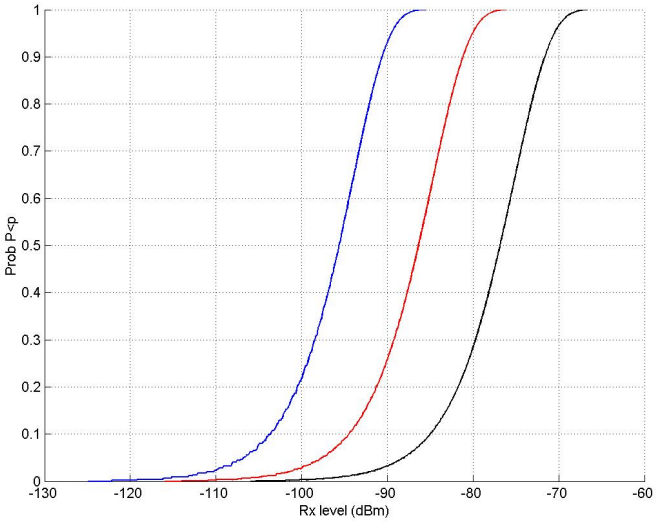

Figure 49. cdf for test case Lillehammer for the 3D component, land use forest (black), field (red) and grass (blue).

In conclusion:

- A 2D component attenuation of more than typically 15 dB requires a 3D model to estimate the signal level accurately,
- a 2D component attenuation above 15 dB occurs in approximately 40 % of the coverage area at Lillehammer and approximately 15 % of the coverage area at Bristol, and
- in a hilly terrain (Lillehammer), the variations due to land usage are much larger than in an undulating terrain (Bristol) due to the difference in the statistics for the incidence and scattering angles. The 3D component for forest was 20 dB higher than that for grass in this case.

7.5.2 Seasonal variations

The analysis in the cases of land use field and grass was repeated with the assumption of snow on the field and water on the grass. The parameters used were in accordance with the estimated values from Chapter 5 and are given in Table 4. Figure 50 shows the mean values of the estimated received signal in the case of field with and without snow for the test case from Lillehammer. The difference in mean value is approximately 3-4 dB for the 3D component, the case with snow providing the highest values. It appears that the lower roughness in the case of snow, leading to fewer significant scatterers, is compensated by the higher reflection coefficient. In the Bristol case the differences between snow and no snow were small for all values for the 2D component, never exceeding 1 dB. In this case snow provided higher values.

URN:NBN:no-1290

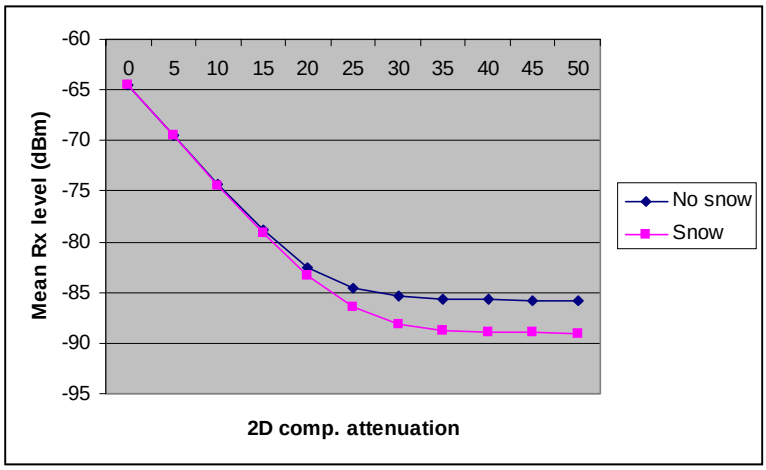

Figure 50. Mean received value (dBm) in the case of field with and without snow, Lillehammer

Figure 51 shows the mean received signal level for test case Bristol in the case of grass, with and without water. For the 3D component the difference between the two cases is approximately 4 dB. This is due to the larger value for the reflection coefficient in the case of a wet surface. For Lillehammer the difference was slightly less. This 3-4 dB difference is consistent with the observations in Chapter 5.

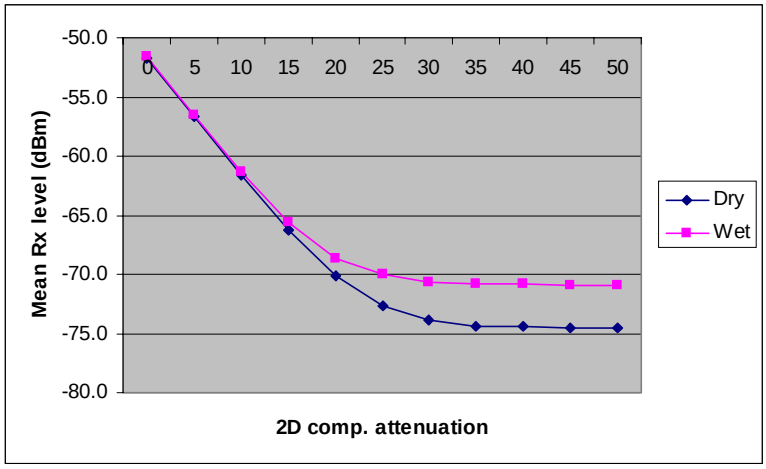

Figure 51. Mean received value (dBm) in the case of grass with and without water, Bristol

In conclusion, the seasonal and weather variations estimated in this analysis gave variations up to 4-5 dB for the mean value of the received signal, indicating that the weather and seasonal variations are indeed significant. The signal level variations resulting from the statistical nature of the estimation due to fading is larger than this, however. It could be noted that the assumption in this analysis of the 2D component being perfectly known is just an approximation, and that in a real case this component will also be subject to weather and

seasonal variations, in particular when the 2D component is diffracted over terrain formations which have electromagnetic properties that change with meteorological conditions.

7.5.3 Parameter variation

To inspect the dependency of parameter variations on the model prediction a series of analysis with varying input parameters were run. In Figure 52 the mean received signal level for test case Bristol with land use field is shown as a function of the (real part of) the relative permittivity, where values from 1.2 up to 20 are used. The case of the 2D component attenuated by 10 dB as well as the case of 3D component only are shown in the figure. The figure shows that the variations in the case of 10 dB 2D attenuation are quite small, as expected. This is due to the 2D component having an important impact in this case. In the case of only 3D component the variations are much larger, approximately 12 dB over the range of permittivity values. The mean Rx-level is increasing with increasing permittivity, this is due to the increasing values for the reflection coefficients leading to a larger amount of the power being scattered from the surfaces. For the test case Lillehammer the variations were slightly smaller, and not uniformly increasing. The results are tabulated in Appendix G.

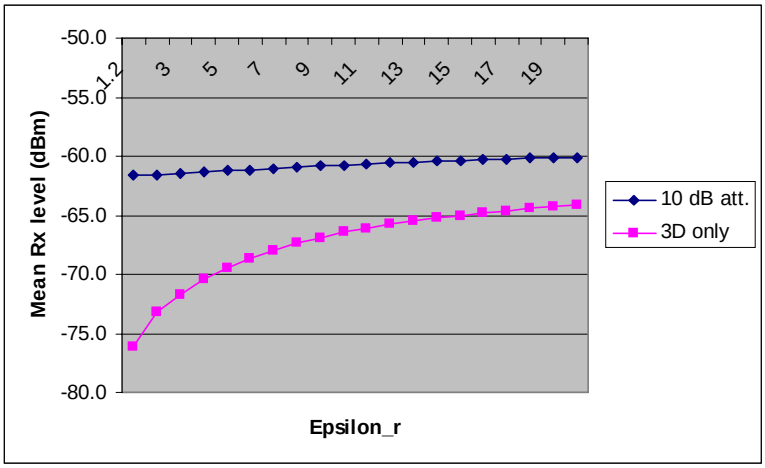

Figure 52. Variation in mean predicted Rx level as a function of relative permittivity, test case Bristol, land use field.

In Figure 53 the mean received signal level for the test case Bristol with land use field is shown as a function of the surface height variation, Δh, where values from 4 mm up to 40 cm are used. As in the case of permittivity variations, a 10 dB 2D attenuation as well as the 3D only case are shown. The 3D case shows variations of more than 20 dB over the range of values. The curve is very steep for values of Δh up to approximately 6-8 cm, but flattens for higher values. This is probably due to the height variation at this value exceeding half a wavelength. For height variations exceeding λ/2, the low incidence angle cases will already be *completely rough*, and any increase in the roughness will not alter the scattering contribution from these surfaces. Figure 54 shows the mean received Rx-level for the test case Lillehammer, for values of the 2D component attenuation of 10 dB as well as the 3D case only. The curves are similar to the ones from Bristol, in the case of only 3D the variations are up to 30 dB, from the lowest height variations to the highest.

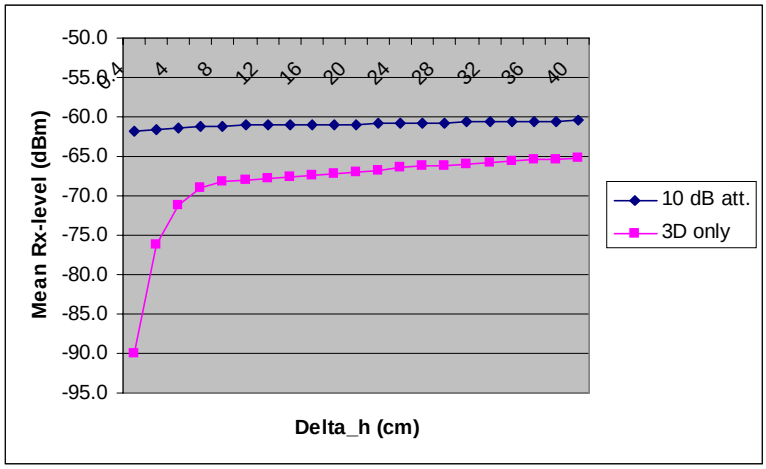

Figure 53. Variation in mean predicted Rx level as a function of height variation, test case Bristol, land use field (wavelength 15 cm).

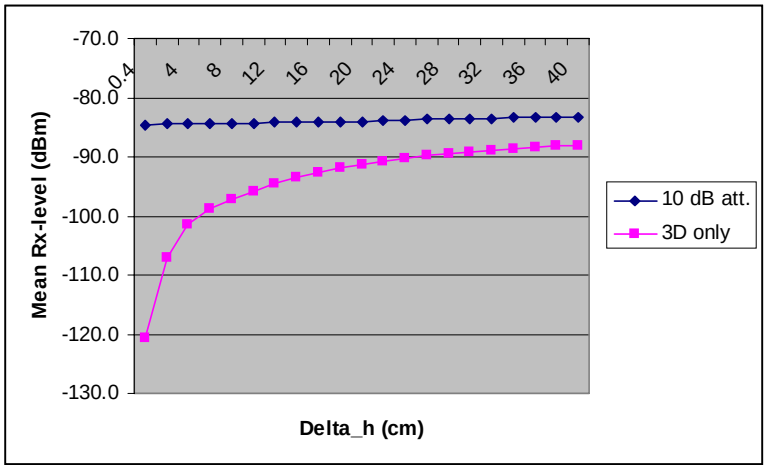

Figure 54. Variation in mean predicted Rx level as a function of height variation, test case Lillehammer, land use field (wavelength 15 cm).

A sensitivity analysis with respect to the conductivity of the ground was also carries out. The variations were however very small for realistic values of conductivity. The values used were from σ=0 to σ=0.3. The results are given in Appendix G. For other surfaces, like sea water, the conductivity may have a much stronger influence.

In conclusion,

- the 3D model sensitivity to parameter variations are small when the 2D component has a strong contribution,
- for the 3D component the variations are large, up to 20 dB,

- an erroneous assumption with respect to roughness or permittivity with a factor of two may alter the mean predicted value by up to 10 dB, and
- the variations with respect to surface height variations are highest for values of height variations below λ/2 (approximately 6-8 cm for UMTS).

7.5.4 Other considerations

Terrain variations

The method used in the previous section was that of attenuating the 2D component while the scattering conditions (3D component) remained constant. In practical cases there will be a correlation between the presence of a strong 2D component and the scattering conditions. Therefore a case for each area type with severe non-line-of-sight conditions was inspected as well. There was no significant 2D component in any of these cases. The 3D terrain plots in the two cases are shown in Figure 55. The plots also show the contributing scattering surfaces in black as well as typical signal paths as red arrows. It is evident that a much larger number of scatterers are contributing in the hilly terrain case. Figure 56 shows the cumulative distribution functions of the received signal level in these two cases, for land use forest. There is a significantly higher signal level for Lillehammer, which is due to the difference in terrain statistics. If a system link budget is considered, the Lillehammer case will provide significant signal level to maintain a connection for approximately 95% of the time for e.g. GSM[38], whereas the Bristol case will fail in 25% of the time.

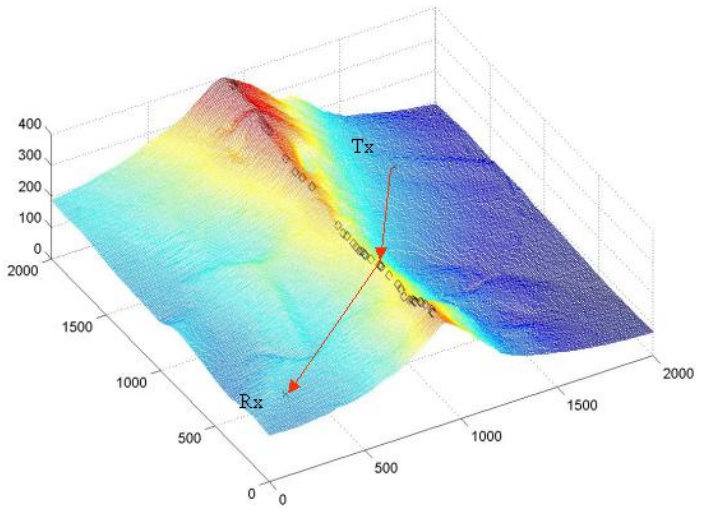

a)

Figure 55. 3D terrain plots non-line-of-sight cases for a) Bristol and b) Lillehammer. Scattering surfaces are shown in black, typical signal paths are show as red arrows.

[38] The sensitivity limit for GSM is –102 dBm.

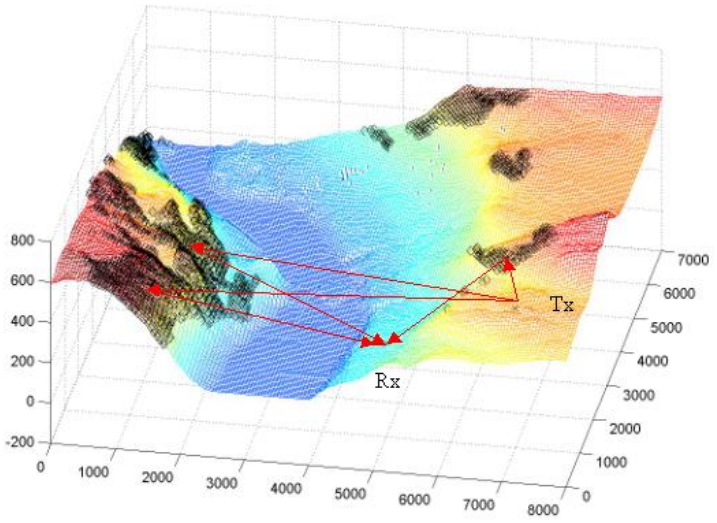

b)

Figure 55. 3D terrain plots non-line-of-sight cases for a) Bristol and b) Lillehammer. Scattering surfaces are shown in black, typical signal paths are show as red arrows.

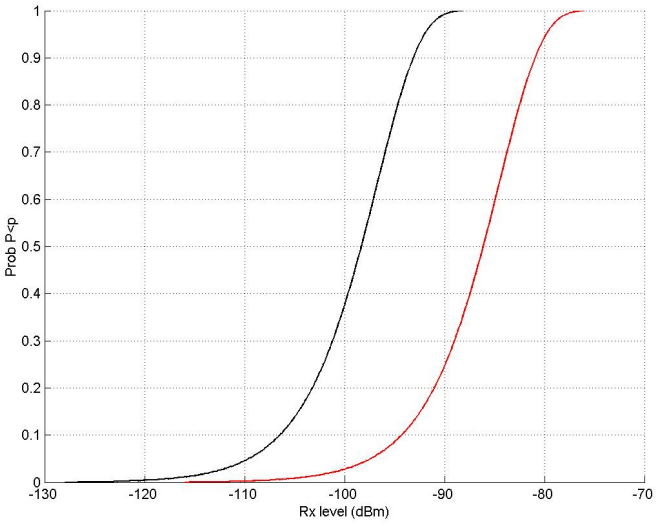

Figure 56. Cumulative distribution of received signal level for the severe non-line-of-sight cases for Bristol (black) and Lillehammer (red), land use forest

URN:NBN:no-1290

Wideband considerations

The discussion so far has been concerned with signal level only, making a narrowband assumption. If a wideband model is desired the time domain must be taken into account. For the case of signal level the statistics must then be calculated for each *time bin* individually, where the length of the time bin is inversely proportional to the signal bandwidth. The model provides the time and angular dispersion of the channel inherently. In Figure 57 examples of power delay profiles from the test cases at Lillehammer are shown[39], for land use forest. Figure 57 a) shows the original test case, whereas Figure 57 b) shows the non-line-of-sight example discussed above. In the non-line-of-sight case the contributions from distant scatterers are more evident, and the profile extends over a longer time range.

Table 7 shows values of delay spread (DS, Chapter 3) for the different test cases, assuming a strongly attenuated 2D component. It is evident that the Lillehammer case has significantly higher values for DS than the Bristol case. Also, for Lillehammer the non-line-of-sight case has the highest value because of the increased significance of the distant scatterers. In the Bristol scenario almost no scatterers contribute in the non-line-of-sight case.

Figure 58 shows the power azimuth spectra (Chapter 2) for the same two cases as in Figure 57[40]. The azimuth spread (AS) is in the same order of magnitude in the two cases. The directions are defined clockwise, relative to the Tx-Rx-direction. In Figure 58 b) a significant amount of the signal power is arriving from back-scattered components (≈180°). In Figure 58 a) the azimuthal distribution is more uniform over the spectrum, but with the most significant components arriving close to the direction of the link (≈0°).

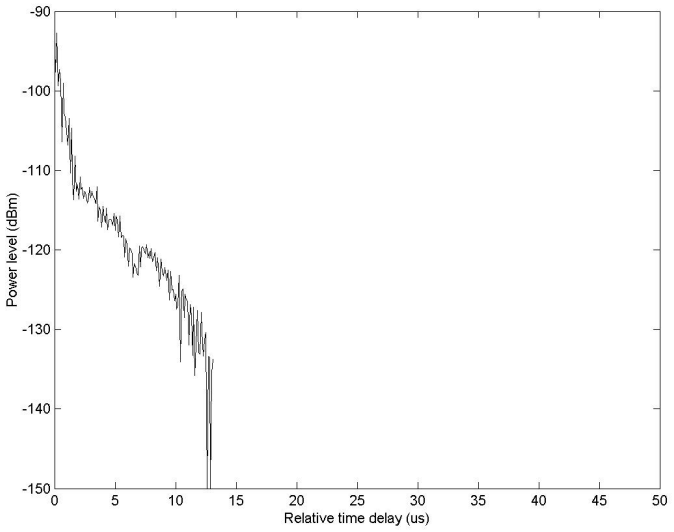

a)

Figure 57. Power delay profile for Lillehammer, a) line-of-sight case and b) non-line-of-sight, land use forest

[39] In the power delay profile, a time resolution of 25 ns is used.

[40] In the power azimuth spectrum, an angular resolution of 2 degrees is used.

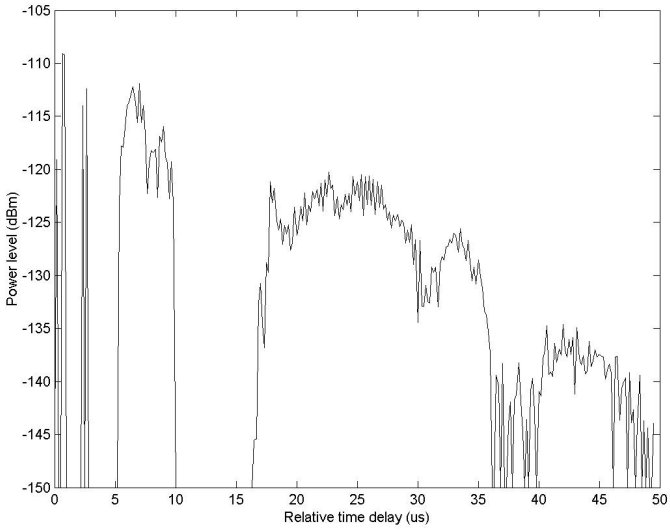

b)

Figure 57. Power delay profile for Lillehammer, a) line-of-sight case and b) non-line-of-sight, land use forest

Test case	**Delay Spread (μs)**
Line-of-sight Lillehammer	1.28
Non-line-of-sigth Lillehammer	9.76
Line-of-sight Bristol	0.27
Non-line-of-sight Bristol	0.019

Table 7. Delay Spread values for different test cases, land use forest

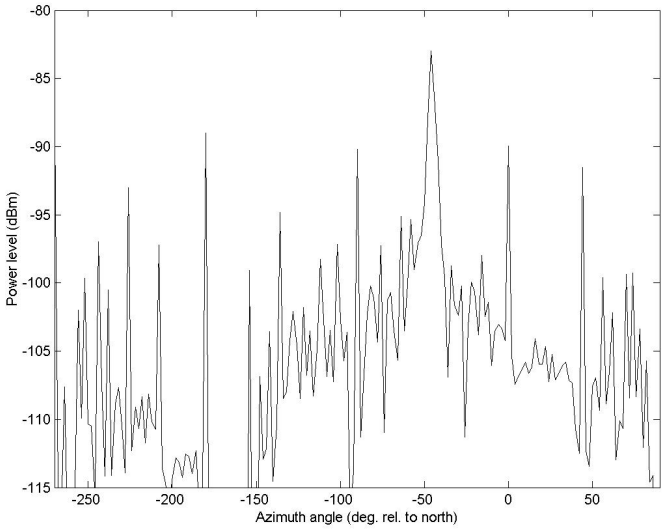

a)

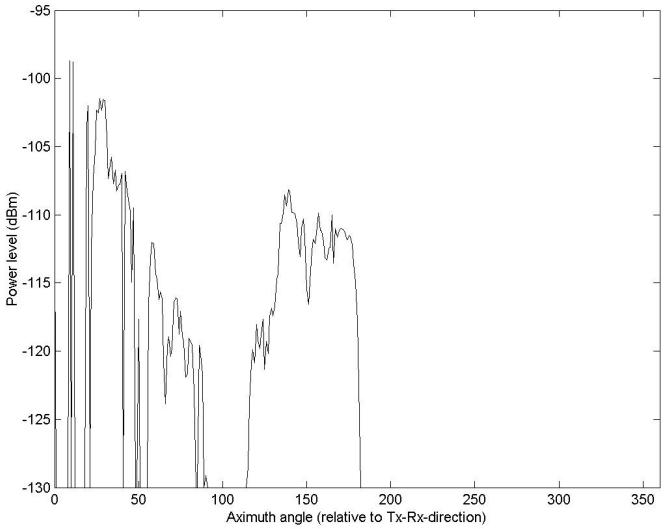

b)

Figure 58. Power azimuth spectrum, Lillehammer, a) line-of-sight case, b) non-line-of-sight, land use forest

7.6 Discussion

The discussion in this report has been limited to channel prediction models for rural areas. Even though the discussion concentrated on the rural case, the description of the 3D radar

model is equally applicable to man-made objects like building walls. This means that the scattering model can also be used in indoor and urban area models when a more realistic assumption than the smooth/large object assumption is desired.

In future advanced Ray-tracing algorithms the single ray will be replaced by a *bundle* of *rays* that is scattered and diffracted from surfaces. The surface description used in such a method can be taken from the method described here. A preliminary step into such a model is presented for indoor environments by Ascom [Liebendörfer99]. In the case of building walls, refraction through the walls as well as diffraction from building edges will be taken into account.

This means that the approach used in the 3D radar model described here and advanced indoor and urban area models will converge. This would also mean that the difference between a rural area approach and an urban area approach would consist of different input parameters, like the scattering parameters and the order of the reflection/scattering to be taken into acount.

7.7 Future work

This study has provided significant input for the development of 3D channel prediction models, especially in the areas of:

- Rough surface scattering, where the new A/P model was introduced.
- Measurements of natural surfaces, where the roughness parameters of typical land use classes were estimated.
- 2D versus 3D channel modeling, where detailed recommendations were given.
- Meteorological variations, where the impact of snow and rain was evaluated.

However, some areas are not covered in detail, and remain subject to future work.

7.7.1 Implementation issues

The demonstration model implementation can be extended into a fully operational 3D channel model to be implemented into a network-planning tool. Using this implementation the predictions should be compared to radio channel measurements to validate the model implementation and tune the model parameters. The validation of the predictions should be performed with respect to the path loss as well as the temporal and angular dispersion.

The implementation should allow shadowing due to foliage to be taken into account, and allow reflection and scattering from man-made objects like building walls. Also the model should allow diffracted-scattered-diffracted signal components.

7.7.2 Propagation issues

The propagation study undertaken can be extended so that a complete catalogue of surface parameters is made available for model implementation. Of particular interest could be the characterisation of the roughness and reflectivity from man-made objects, like building walls. Also, it is of interest to perform more measurement at angles close to grazing, as discussed in Subsection 7.5.4. The angular dependency for the diffuse component can have a relatively large impact on the 3D prediction.

Also, the propagation study can be extended into new frequency bands, to inspect the frequency dependence on the results and conclusions.

7.7.3 Urban areas

The type of sensitivity analysis performed in this chapter can be performed also for urban area models. It is also of interest to pursue the idea of using a general scattering/reflection model like the amplitude/phase-model also in a rural area implementation like ray-tracing. It can then be evaluated whether a merger of the 3D radar approach and the ray-tracing approach into a more generalized way of doing 3D modeling as described in the previous section is plausible.

8 Conclusions

8.1 Motivation and main results

The motivation behind the work was the need for more accurate radio channel prediction models to allow efficient radio planning. The channel models should be able to provide an accurate estimation of the path loss (signal level), and also be able to estimate time dispersion and angular dispersion, taking into account 3-dimensional contributions. The focus was on rural areas, because radio coverage of rural areas is more costly when using higher frequencies, which is the case for UMTS compared to GSM. In addition seasonal and environmental variations are strongest here. Radio frequencies around 2 GHz were selected, as these are the most important frequency bands for mobile systems for wide area coverage, even though the envisaged approach also supports radio planning for GSM 900 and WLAN systems.

The main achievements of the work can be summarised in the following points:

1. **The development of a novel approach, the Amplitude/Phase model, to the modeling of scattering from random rough surfaces** *for 3D channel modeling. The model is simple and accurate, compared to conventional models. It makes no inherent assumption about the degree of roughness, making it suited to model all surfaces. A performance comparison with conventional models was carried out.*

2. **The development of an experimental methodology to characterise random rough surfaces**. *The work characterised natural surfaces such as asphalt, grass, farmland, and forest, each of them having a different degree of roughness. In the analysis each surface type was characterised by its surface height variation and its reflection coefficient. Variations due to weather and seasonal changes were taken into account.*

3. **An analysis of the implications of the results on 3D channel modeling** *using a demonstration model. The analysis included a comparison between 2D and 3D model prediction for different area types and land use classes. Also the prediction sensitivity to seasonal and weather variations as well as model parameter variations were inspected.*

8.2 Amplitude/phase model development

An analysis of channel models used for radio network planning was performed. The analysis concluded that for rural areas a type of models referred to as *3D radar models* was preferable. These models estimate the path loss in the vertical Tx-Rx plane and take off-axis scattering into account. The path loss is calculated using diffraction theories. Contributions from off-axis scattering are taken into account from surfaces seen by both the transmitter and receiver. The 3D radar models inherently estimate the parameters describing path loss, time dispersion and angular dispersion, they provide high accuracy, and have a reasonable complexity allowing efficient propagation modeling.

To improve the accuracy in the 3D radar models a novel approach to estimating the scattering from random rough surfaces was developed. The model is referred to as the *amplitude/phase (A/P) model*. The A/P model uses a simple physical representation of the surface as a *chessboard* of small, plane surfaces. Scattering from the surfaces is described using closed form expressions for the diffuse scattering and coherent reflection from the surface. The model represents the surface using two parameters; the equivalent surface height variation Δh and the plane surface reflection coefficient Γ. The model makes no explicit assumptions about the

degree of roughness and is therefore suited to describe the scattering from all types of rough surfaces.

8.3 Estimation of roughness parameters from natural surfaces

Measurements of scattering from natural surfaces such as plane asphalt, grass, farmland and forest were performed. The surfaces have different degrees of roughness. A parameter fit of Γ and Δh was performed for the A/P model, and results were compared to other well-known rough surface scattering methods that are currently used for channel prediction. These models were; the *Plane surface model*, the *Oren model*, the *Kirchoff model* and the *Small Perturbation method*. For all the surfaces the A/P model performed best. The other models were approximately 1.5 dB to 10 dB inferior to the A/P model. The Kirchoff model had the best performance of the conventional models.

Measurements of the surface parameters Γ and Δh were performed using two measurement set-ups. For non-grazing incidence angles, directive antennas pointing to the same position on the ground were used. The roughness parameters were extracted from power measurements for different pointing directions. The receiving antenna was mounted flexibly to allow positioning in from 0° to 70° in elevation and from -5° to 45° in relative azimuth angle. The optimal parameters were then found in the least square sense for each measurement series. A different approach was used in the case of *grazing incidence*, where a method using a receiving array antenna and super-resolution direction finding using ESPRIT was developed.

Typical estimated equivalent surface height variations estimated are summarised in Table 8. The reflection coefficients for each of the dry surfaces were similar to the ones reported in the literature.

	Asphalt	**Grass**	**Field**	**Forest**
Δh	10 mm	25 mm	100 mm	500 mm

Table 8. Typical estimated height variations Δh on dry surfaces with varying degree of roughness

The measurements were also repeated under different weather and seasonal conditions. Water on asphalt did not change the reflection coefficient significantly, but increased the value of Γ by up to 50 % on grass. Snow on the ploughed field reduced the apparent roughness by more than 50 % and increased the reflection coefficient significantly.

8.4 3D prediction model implementation

The work provides an analysis of the applicability of the A/P model for advanced radio channel modeling. An implementation guide for the A/P model in 3D radar channel prediction models is provided. The guidelines suggest in particular a prediction in terms of a confidence interval using the probability density function of the received signal components. Also, it is suggested to make a distinction between the *low-scatter* and *high-scatter* cases, to allow the estimation to predict variations due to seasonal and weather changes.

A demonstration 3D prediction model was implemented, and sample scenarios were tested using digital elevation maps. One area was an undulating terrain in Bristol, UK, and another was a hilly terrain in Lillehammer, Norway. It was shown that the two areas have significantly

different terrain statistics. In the hilly terrain more than 40 % of the coverage area was in a *blocked state* for the base station positions used. In the undulating terrain approximately 15 % of the coverage area was in a *blocked state*. A blocked state is defined as when the 2D vertical plane attenuation exceeds the free space attenuation by more than 15 dB, which is the value where 3D contributions should be taken into account. In the sample scenarios typical base station and mobile station positions were used. The received signal consisted of a non-random 2D component in the vertical Tx-Rx-plane in addition to a 3D component consisting of contributions from random, scattered components from off-axis surfaces. In the sample cases the value of the 2D component was set to different values to inspect varying degrees of line-of-sight, ranging from free space to a non-existent 2D component. Different land use classes were investigated, namely forest, ploughed field and grass.

It was shown that the use of a 3D model is essential when the 2D component was attenuated more than typically 15 dB compared to free space, somewhat dependant on area type and land use. 3D scattering components appear to be important for the total received signal. For the hilly terrain, more than 40 % of the coverage area is in “a blocked state”, leading to the conclusion that in this area traditional 2D models are not sufficient.

The 3D component has a Rayleigh shape distribution, with a typical difference between the 5 and 95 percentiles in the distribution of more than 10 dB. A 3D channel model is essential to predict the time and angular dispersion, regardless of the level of the 2D component.

The hilly terrain of Lillehammer gives a larger number of contributing distant scatterers, resulting in a higher influence of terrain coverage (land use class). In Lillehammer, land use forest gave 20 dB stronger received 3D signal component compared to grass coverage.

Variations in the predictions due to seasonal and weather conditions were up to 4-5 dB for the average values. For radio prediction for mobile systems, there is a natural variability in the environmental parameters due to seasonal and weather conditions. This points to an inherent limitation in the possible accuracy in rural areas. A sensitivity analysis with respect to the model parameters showed that an erroneous assumption about the permittivity or surface roughness by a factor of two could change the mean of the received radio signal by up to 10 dB. This demonstrates the importance of accurate knowledge of the surface parameters.

An inspection of the time dispersion for the two test areas showed significant differences. In the hilly terrain in Lillehammer the time dispersion was much more severe due to the different terrain statistics and the presence of distant scatterers. The delay spread parameter was approximately 10 μs at Lillehammer compared to approximately 1 μs at Bristol for otherwise equal conditions. In severe non-line-of-sight conditions the difference in delay spread was even larger. 3D modeling takes into account the contributions from distant 3D scatterers, and gives a prediction that allows a connection for mobile communication systems in the hilly terrain. In the undulating rural terrain the 3D scatterers are less dominant, and their contributions are of minor importance.

The work has shown that 3D radio prediction is important in rural areas with hilly terrain, where as much as 40 % of the coverage area is in a blocked state to the transmit antenna. The effect is less dominant in undulating terrain. An accurate knowledge of the surface parameters, both in term of reflectivity and equivalent surface height variation, is essential for the prediction. The suggested A/P model provides an easy tool for the inclusion of natural rough surfaces, and the accompanied measurements provide equivalent roughness heights for the surfaces being most present in rural areas: Grass, farmland and forest.

Literature list

[Aanvik97] Aanvik, F, et.al. 1997. A measurement setup for wideband radio channel measurements in the angular domain. Kjeller, Norway, Telenor R&D. (Telenor R&D Report R 48/97)

[Aas92] Aas, J A. 1992. *Antenneteknikk* (in Norwegian). Trondheim, Norway, Norwegian Institute of Technology.

[Anderson96] Anderson, H R. 1996. A second generation 3-D ray-tracing model using rough surface scattering. In: *Proceedings of IEEE 46th Vehicular Technology Conference-VTC'96*. Atlanta, USA, IEEE, 46-50

[Aulin79] Aulin, T. 1979. A modified Model for the fading signal at a mobile radio channel. *IEEE Trans. on Vehicular Technology*, VT-28 (3), 182-203

[BachAndersen00] Bach Andersen, J. 2000. Antenna arrays in mobile communications: Gain, diversity and channel capacity. *IEEE Antennas and Propagation Magazine*, 42 (2), 12-16

[Badsberg95] Badsberg, M, Andersen, J B, Mogensen, P. 1995. *Exploitation of the terrain profile in the Hata model*, Aalborg, Denmark, COST231, (COST 231 TD(95)9)

[Balanis89] Balanis, C A. 1989. *Advanced Engineering Electromagnetics*. New York, USA, John Wiley & Sons. ISBN 0-471-50316-9

[Becker95] Becker, T C, Kürner, T, Cichon, C J. 1995. *Fast scatterer search algorithms for 3D wave propagation*. Bern, Switzerland, COST231, (COST231 TD(95)010)

[Beckman87] Beckman, P, Spizzichino, A. 1987. *The scattering of electromagnetic waves from rough surfaces*. Norwood, MA, USA, Artech House. ISBN 0-89006-238-2

[Bello63] Bello, P A. 1963. Characterization of randomly time-variant linear channels. *IEEE Trans. on Communications Systems*. CS-11 (4), 360-393

[Berg94] Berg, J-E, Holmquist, H. 1994. An FFT multiple half-screen diffraction model. In*: Proceedings of the 44th IEEE Vehicular Technology Conference - VTC'94*, Stockholm, Sweden, IEEE, 195-199

[Berg94_2] Berg, J-E. 1994. A macrocell model based on the parabolic differential equation. In: *Proceedings of Virginia Tech's Fourth Symposium on Wireless Personal Communications*, Virginia, USA, Virginia Tech, 9.1-9.10

[Berg95] Berg, J-E. 1995. A recursive method for street microcell path loss calculation. In*: Proceedings of the Fifth IEEE International Symposium on Personal, Indoor and Mobile Radio Communications - PIMRC'95*, Toronto, Canada, IEEE, 140-143

[Bertoni94] Bertoni, H L, Honcharenko, W, Maciel, L R. 1994. UHF propagation prediction for wireless personal communications. *Proceedings of the IEEE,* 82 (9), 1333-1359

[Boithias87] Boithias, L. 1987. *Radio Wave Propagation*. London, UK, North Oxford Academic. ISBN 0-946536-06-6

[Börjeson92] Börjeson, H, Bergljung, C, Olsson, L G. 1992. Outdoor microcell measurements at 1700 MHz. In*: Proceedings of the 42nd IEEE Vehicular Technology Conferences - VTC'92*, Denver, USA, IEEE, 927-931

[Braun91] Braun, W R, Dersch, U. A physical mobile radio channel model. *IEEE Trans. on Vehicular Technology*. 40 (2), 472-482

[Bråten98] Conversation with research scientist *Lars Bråten*, 1998. Telenor R&D, Kjeller, Norway

[Brennan98] Brennan, C, Cullan, P J. 1998. Tabulated interaction method for UHF terrain propagation problems. *IEEE Trans. on Antennas and Propagation*. 46 (5), 738-739

[Brook95] Brook, T, Driessen, P F, Kirlin, R L. 1995. Propagation measurements using synthetic aperture radar techniques, In*: Proceedings of the 45th IEEE Vehicular Technology Conferences - VTC'95*, Chicago, USA, IEEE, 1633-1637

[Broschat90] Brochat, E. 1990. A heuristic algorithm for the bistatic radar cross section for random rough surface scattering. *IEEE Trans. on Geoscience and Remote Sensing*. 28 (2), 202-206

[Bullington47] Bullington, K. 1947. Radio propagation at frequencies about 30 Mc. In: *Proceedings of IRE*, 35 (10), 1122-1136

[Cátedra98] Cátedra, M F, et. al. 1998. Efficient ray-tracing techniques for three-dimensional analyses of propagation in mobile communications: Application to picocell and microcell Scenarios. *IEEE Trans. on Antennas and Propagation*. 40 (2), 15-28

[Clarke68] Clarke, R H. 1968. A statistical theory of mobile radio reception. *Bell Systems Technical Journal*, 47 (6), 957-1000

[CODIT95] UMTS Code Division Testbed (CODIT) project. 1995. *CODIT final review report*, Brussels, Belgium, The Commission of the European Communities (ACTS project CODIT final report)

[COST207_89] COST207. 1989. *Digital land mobile radio communications*. Luxembourg, The Commission of the European Communities, ISBN 92-825-9946-9

[COST231_99] COST231. 1999. *COST 231 - Evolution of Land Mobile and Personal Communications*, Luxembourg, The Commission of the European Communities, ISBN 92-828-5416-7

[Craig96] Craig, K H. 1996. Impact of numerical methods on propagation modeling. In: *Modern radio science 1996*, Hamelin, J (editor). Oxford, UK, Oxford University Press. ISBN 0-19-856529-1

[Davidsen94] Davidsen, K, Danielsen, M. 1994. Predicting impulse responses in mountainous areas. In*: Proceedings of the Fourth IEEE International Symposium on Personal, Indoor and Mobile Radio Communications - PIMRC'94*, the Hague, the Netherlands, IEEE, 25-27

[DegliEsposti99] Degli-Esposti, V, Bertoni, H L. 1999. Evaluation of the role of diffuse scattering in urban microcellular propagation. In: *Proceedings of IEEE 49th Vehicular Technology Conference-VTC'99*, Houston, USA, IEEE, 1392-1396

[Deygout66] Deygout, J. 1966. Multiple knife-edge diffraction of microwaves. *IEEE Trans. on Antennas and Propagation*. 14 (4), 480-489

[DeRoo94] De Roo, R D, Ulaby, F W. Bistatic specular scattering from rough dielectric surfaces. *IEEE Trans. on Antennas and Propagation*. 42 (1), 220-231

[Duel-Hallen00] Duel-Hallen, A, Hu, S, Hallen, H. 2000. Long-range prediction of fading signals – Enabling adapting transmission for mobile radio channels. *IEEE Signal Processing Magazine*, 17 (3), 62-75

[Eggers92] Eggers, P, et. al. 1992. Assessment of GSM-link quality dependence on radio dispersion in rural environments. In*: Proceedings of the 42nd IEEE Vehicular Technology Conferences - VTC'92*, Denver, USA, IEEE. 532-535

[Epstein53] Epstein, J, Peterson, D W. 1953. An experimental study of wave propagation at 850 MC. *Proceedings of IRE*, 41 (5), 595-611

[Francechetti99] Francechetti, G, Palmieri, F. 1999. Propagation without wave equation toward an urban area model. *IEEE Trans. on Antennas and Propagation*. 47 (9), 1393-1404

[Fuhl98] Fuhl, J, Molisch, A F, Bonek, E. 1998. A unified channel model for mobile radio systems with smart antennas. *IEE Proceedings – Radar Sonar Navigation*, 145 (1), 32-41

[Gagliardi91] Gagliardi, R M. 1991. *Satellite Communications*, New York, USA, Van Nostrand Reinhold. ISBN 0-442-22745-0

[Geng95] Geng, N, Wiesbeck, W. 1995. Parabolic equation method simulations compared to measurements. In: *Proceedings of the IEEE Ninth International Conference on Antennas and Propagation-ICAP'95*, Eindhoven, the Netherlands, IEEE, 359-362

[Gonçalves00] Gonçalves, N C, Correia, L M. 2000. A propagation model for urban microcellular systems at the UHF band. *IEEE Trans. on Vehicular Technology*. 49 (4), 1294-1302

[Gschwendtner95] Gschwendtner, B E, et. al. Ray tracing vs. ray launching in 3-D microcell modeling. In: *Proceedings of the European Personal and Mobile Communications Conference - EPMCC'95*, Bologna, Italy, 74-79

[GSM92] ETSI. 1992. *European digital cellular telecommunications system (Phase 1; Radio transmission and reception (GSM 05.05)* (I-ETS 300 033)

[Gudmundson91] Gudmundson, M. 1991. Correlation model for fading in mobile radio systems. *Electronics letters*, 27 (23), 2145-2146

[Hansen96] Hansen, S I, Lehne, P H, Pettersen, M. *Intelligente antenner for mobilkommunikasjon* (in Norwegian), Kjeller, Norway, Telenor R&D. (Telenor R&D Scientific Document N 61/96)

[Harman63] Harman, W W. 1963. *Principles of Statistical Theory of Communication*. New York, USA, McGraw-Hill Electrical and Electronic Engineering Series

[Harrington61] Harrington, R F. 1961. *Time-harmonic electromagnetic fields*. New York, USA, McGraw-Hill Book Company, ISBN 0-07-026745-6

[Hata80] Hata, M. 1980. Empirical formula for propagation loss in land mobile radio services. *IEEE Trans. on Vehicular Technology*. VT-29 (3), 317-327

[Holma00] Holma, H, Toskala, A. 2000. *WCDMA for UMTS – Radio access for third generation mobile communications*. New York, USA, John Wiley & Sons. ISBN 0-471-72051-8

[Hoppe98] Hoppe, R, Wölfle, G, Landstorfer, F M. 1999. Fast 3-D ray tracing for the planning of microcells by intelligent preprocessing of the database. In: *Proceedings of the European Personal and Mobile Communications Conference - EPMCC'99*, Paris, France, 149-154

[Hufford48] Hufford, G. 1948. *On the propagation of horizontally polarized waves over irregular terrain*. University of Washington, Washington, USA (Master thesis)

[Hviid95] Hviid, J T, et.al. 1995. Terrain-based propagation model for rural area - An integral equation approach. *IEEE Trans. on Antennas and Propagation*. 43 (1), 41-46

[Ikegami84] Ikegami, F, Yoshida, S, Umehira, M. 1984. Propagation factors controlling mean field strength on urban streets. *IEEE Trans. on Antennas and Propagation*. 32 (8), 822-829

[ITU99] ITU. 1999. *Report of the eighteenth and final meeting of task group 8/1, Helsinki, Finland.* (ITU, Radio Communication Study Groups)

[Janacek93] Janacek, G, Swift, L. 1993. *Time Series – Forecasting, Simulation, Applications.* New York, USA, Ellis Horwood. ISBN 0-13-103581-9

[Janaswamy98] Janaswamy, R, Bach Andersen, J. 1998. Path loss predictions in urban areas sprawling over irregular terrain. In*: Proceedings of the Ninth IEEE International Symposium on Personal, Indoor and Mobile Radio Communications - PIMRC'98*, Boston, USA, IEEE, 874-878

[Kaplan86] Kaplan, P. 1986. Predicting Antenna Sidelobe Performance. *Microwave Journal*, 29 (9), 201-206

[Keller62] Keller, J B. 1962. Geometrical theory of diffraction. *Journal for the Optical Society of America*, 52 (2), 116-130

[Khenchaf96] Khenchaf, A, Daout, F, Saillard, J. 1996. The two-scale model for random rough surface scattering. In: *Proceedings of OCEANS '96, Prospects for the 21st Century.* MTS/IEEE, 887-891

[Khenchaf99] Khenchaf, A. 1999. The Brewster angle effect on sea surface scattering for near-grazing incidence. In: *Proceedings of International on Geoscience and Remote Sensing Symposium 1999 (IGARSS '99).* Stein, T I (Ed). IEEE, 2622-2624

[Kreyzig88] Kreyzig, E. *Advanced Engineering Mathematics*. New York, USA, John Wiley & son. ISBN 0-471-62787-9

[Kuhlmann95] Kuhlmann, P. 1995. *A forward scattering algorithm for prediction of the direct link in a three-dimensional model*. Poznan, Poland, COST231, (COST 231 TD(95)137)

[Kurner92] Kurner, T, Cichon, D J, Wiesbeck, W. 1992. Verification of deterministic wave propagation models for rural and urban areas. In: *Proceedings of IEEE Ant. and Prop. Society Int. Symposium*. IEEE, 1376-1397

[Kurner93] Kurner, T, Cichon, D J, Wiesbeck, W. 1993. *Concepts and results for 3D digital terrain-based wave propagation models: An overview*. IEEE Journ. on Selected Areas in Communications. 11(7), 1002-1012

[Kurner96] Kurner, T, Cichon, D J, Wiesbeck, W. 1996. Evaluation and verification of the VHF/UHF propagation channel based on a 3-D-wave propagation model. *IEEE Trans. on Antennas and Propagation*. 44 (3), 393-404

[LaCascue56] LaCascue, E O, Tamarkin, P. 1956. Underwater sound reflection from a corrugated surface. *Journal of Applied Physics*, 27(2), 138-148

[Landron93] Landron, O, Feuerstein, M J, Rappaport, T S. 1993. In situ microwave reflection coefficient measurements for smooth and rough exterior wall surfaces. In*: Proceedings of the 43rd IEEE Vehicular Technology Conferences - VTC'93*, Secaucus, USA, IEEE, 77-80

[Lebherz92] Lebherz, M, Wiesbeck, W, Krank, W. 1992. A versatile wave propagation model for the VHF/UHF range considering three-dimensional terrain. *IEEE Trans. on Antennas and Propagation*. 40(10), 1121-1131

[Lee01] Lee, B, Nix, A, McGeehan, J. 2001. A spatio-temporal ray launching propagation model for UMTS pico and microcellular environments. In: *Proceedings of IEEE 53rd Vehicular Technology Conference-VTC Spring'2001,* Rhodes, Greece, IEEE

[Lee82] Lee, W C Y. 1982. *Mobile Communications Engineering*. New York, USA, McGraw-Hill. ISBN 0-07-037039-7

[Lehne98] Lehne, P, et. al. 1998. *Smart antenna performance based on directional radio channel measurements.* Kjeller, Norway, Telenor R&D. (Telenor R&D Report R 42/98)

[Lehne99] Lehne, P H and Pettersen, M. 1999. An overview of smart antenna technology for mobile communications systems. *IEEE Communications Surveys* (Web Journal, www.comsoc.org/livepubs/surveys), IEEE

[Leppänen92] Leppänen, R, Lähteenmäki, J, Tallquist, S. 1992. *Radiowave propagation at 900 and 1800 MHz bands in wooded environments*, Helsinki, Finland, COST231 (COST231 TD(92)112)

[Levy00] Levy, M. 2000. *Parabolic equation methods for electromagnetic wave propagation*. London, UK, Institute of Electrical Engineers. ISBN 0-85296-764-0

[Liang98] Liang, G, Bertoni, H L. 1998. A new approach to 3-D ray-tracing for propagation prediction in cities. *IEEE Trans. on Antennas and Propagation*. 46 (6), 853-863

[Lie97] Lie, A, Remvik, P K. 1997. Performance efficient method for scattering reflection prediction in mobile cellular networks, In*: Proceedings of the 47th IEEE Vehicular Technology Conferences - VTC'97*, Phoenix, USA, IEEE, 1103-1107

[Liebendörfer99] Liebendörfer, M, Dersch, U. New algorithm allows fast indoor propagation prediction for changing tranmitter and receiver position. In: *Proceedings of VDE/ITG Messverfahren im Mobilfunk*, Günzberg/Donau, IEEE/VDE/ITG

[Liebenow94] Liebelow, U, Kuhlmann, P. 1994. Theoretical investigations and wideband measurements on wave propagation in hilly terrain. In*: Proceedings of the 44th IEEE Vehicular Technology Conferences - VTC'94*, Stockholm, Sweden, IEEE, 1803-1806

[Liebenow95] Liebenow, U. 1995. *A three-dimensional propagation model in comparison with measurements*. Florence, Italy, COST231 (COST231 TD(95)71)

[Liebenow96] Liebenow, U, Kuhlmann, P. 1996. A three-dimensional wave propagation model for macrocellular mobile communication networks in comparison with measurements. In*: Proceedings of the 46th IEEE Vehicular Technology Conference - VTC'96,* Atlanta, USA, IEEE, 1623-1627

[Løvnes91] Løvnes, G, Paulsen, S E, Rækken, R H. 1991. *UHF radio channel characteristics - Part one: Multipath propagation and description of the NTR channel sounder*. Kjeller, Norway, Telenor R&D. (Telenor R&D Report R 54/91)

[Løvnes92] Løvnes, G, Paulsen, S E, Rækken, R H. 1992. *UHF radio channel characteristics - Part two: Wideband propagation measurements in large cells*, Kjeller, Norway, Telenor R&D. (Telenor R&D Report R 19/92)

[Marshall90] Marshall, S V, Skitek, G G. 1990. *Electromagnetic Concepts and Applications.* Englewood Cliffs, NJ, USA, Prentice Hall International. ISBN 0-13-247842-0

[Molisch99] Molisch, A F, et.al. Efficient implementation of a geometry-based directional model for mobile radio channels. In: *Proceedings of IEEE 49th Vehicular Technology Conference-VTC'99,* Houston, USA, IEEE, 1999, 1449-1453

[Moroney95] Moroney, D, Cullen, P J. 1995. An integral equation approach to UHF coverage estimation. In: *IEEE Ninth International Conference on Antennas and Propagation-ICAP'99*. Eindhoven, the Netherlands, IEEE, 367-372

[Noll92] Noll, J, Borgeand, M. 1992. *Polarimetric properties of theoretical surface scattering models and comparisons with measured SAR-data*, ESA WPP-31, 41-48

[Nørklit98] Nørklit, O, Bach Andersen, J. 1998. Diffuse channel model and experimental results for array antennas in mobile environments, *IEEE Trans. on Antennas and Propagation*. 46 (6), 834-840

[Ogilvy91] Ogilvy, J A. 1991. *Theory of Wave Scattering from Random Rough Surfaces*. Bristol, UK, IOP Publishing Ltd. ISBN 0-7503-0063-9

[Okumura68] Okumura, Y, et.al. 1968. Field strength and its variability in VHF and UHF Land-Mobile Radio Service. *Review of the Electrical Communications Laboratory*, 16 (9-10), 825-873

[Oren95] Oren, M, Nayar, S K. 1995. Generalisation of the of the Lambertian Model and Implication for Machine Vision, *International Journal of Computer Vision*, 14 (3), 227-251

[Pahlavan95] Pahlavan, K, Levesque, A. 1995. *Wireless Information Networks*. New York, USA, John Wiley & Sons. ISBN 0-471-10607-0.

[Parsons92] Parsons, D. 1992. *The Mobile Radio Propagation Channel*. London, UK, Pentech Press. ISBN 0-7273-1316-9.

[Pedersen00] Pedersen, K I, Mogensen, P E, Fleury, B H. 2000. A stochastic model of the temporal and azimuthal dispersion seen at the base station in outdoor propagation environments. *IEEE Trans. on Vehicular Technology*, 49 (2), 437-447

[Pedersen98] Pedersen, K I, Mogensen, P, Fleury, B. 1998. Spatial channel characteristics in outdoor environments and their impact on BS antenna system performance, In: *Proceedings of IEEE 48th Vehicular Technology Conference-VTC'98*, Ottawa, Canada, IEEE, 719-723

[Pettersen01_1] Pettersen, M, Stette, G, Noll, J. 2001. Characterisation of natural surface scattering for 3D channel modelling. In: *Proceedings of the European Personal and Mobile Communications Conference - EPMCC2001*, Vienna, Austria

[Pettersen01_2] Pettersen, M, Stette, G, Noll, J. 2001. A novel approach to the modeling of natural surface scattering for 3D channel prediction. In: *Proceedings of the 53rd IEEE Vehicular Technology Conference – VTC-2001 Spring*, Rhodes, Greece, IEEE

[Pettersen02] Pettersen, M, Stette, G, Noll, J. 2002. Applicability of rough surface scattering to 3D radio planning. Submitted to: *IEEE Semiannual Vehicular Technology Conference – VTC'2002 Spring*, Birmingham, USA, IEEE

[Rice51] Rice, S O. 1951. Reflection of electromagnetic waves from slightly rough surfaces. *Comm. Pure Applied Mathematics*. 4, 351-378

[Rizk96] Rizk, K, el.al. 1998. Propagation in urban microcells with high-rise buildings. In*: Proceedings of the 46th IEEE Vehicular Technology Conferences - VTC'96*, Atlanta, USA, IEEE, 859-863

[Ro88] Ro, R, et.al. 1988. Facet-ensemble method for wave scattering from rough surface. In: *Proceedings of International Ultrasonic Symposium 1988.* McAvoy, B R (Ed). IEEE, 1075-1078

[Skyttemyr99] Skyttemyr, S A, Hansen, P S, Alsos, O. 1999. *A broadband cavity-backed S-band microstrip antenna*. Kjeller, Norway, Telenor R&D (Telenor R&D Scientific Document N 100/99)

[Sørensen98] Sørensen, T B. 1998. Correlation model for slow fading in small urban macrocell. In*: Proceedings of the Ninth IEEE International Symposium on Personal, Indoor and Mobile Radio Communications - PIMRC'98*, Boston, USA, IEEE, 1161-1165

[Stette93] Stette, G. 1993. *Radiotransmisjon i mikrobølgeområdet* (in Norwegian). Trondheim, Norway, Norwegian Institute of Technology

[Stocker92] Stocker, K E, Landstorfer, F M. 1992. Empirical prediction of radio-wave propagation by neural network simulator. *Electronics Letters*, 28 (8), 724-726

[Stocker93] Stocker, K E, Gschwendter, B E, Landstorfer, F M. 1993. Neural network approach to prediction of terrestrial wave propagation for mobile radio. *IEE-Proceedings-H*, 140 (4), 315-320

[Tameh00] Conversation with *Dr. Eustace Tameh*. 2000. University of Bristol, Bristol, UK

[Tameh97] Tameh, E K, Nix, A R, Beach, M A. 1997. A 3-D integrated macro and microcellular propagation model, based on the use of photogrammetric terrain and building data, In*: Proceedings of the 47th IEEE Vehicular Technology Conferences - VTC'97*, Phoenix, USA, IEEE, 1103-1107

[Tameh98] Tameh, E K, Nix, A R. 1998. The use of measurement data to analyse the performance of rooftop diffraction and foliage loss algorithms in a 3-D integrated urban/rural propagation model, In*: Proceedings of the 48th IEEE Vehicular Technology Conferences - VTC'98*, Ottawa, Canada, IEEE, 303-307

[Tamir77] Tamir, T. 1977. Radio wave propagation along mixed paths in forest environments. *IEEE Trans. on Antennas and Propagation*. 25(4), 471-477

[Tjelta97] Tjelta, T. 1997. *General diffraction principles in relation to mobile telephone coverage in urban areas*, Lecture on 17 March 1997 at Tromsø University

[Torsner99] Torsner, J, Malmgren, G. 1999. Radio network solutions for HIPERLAN/2. In: *Proceedings of IEEE 49th Vehicular Technology Conference-VTC'99*, Houston, USA, IEEE, 1217-1221

[Ulaby86] Ulaby, F T, Moore, R K, Fung, A K. 1986. *Microwave Remote Sensing, Active and Passive, Volume III - From Theory to Applications*. Norwood, MA, USA, Artech House. ISBN 0-89006-192-0

[Ulaby89] Ulaby, F T, Craig Dobson, M. 1989. *Handbook of Radar Scattering Statistics for Terrain*. Norwood, MA, USA, Artech House. ISBN 0-89006-336-2

[Ulaby90] Ulaby, F T, Elachi, C. 1990. *Radar Polarimetry for Geoscience Applications*. Norwood, MA, USA, Artech House. ISBN 0-89006-406-7

[Vogler82] Vogler, L E. 1982. An attenuation function for multiple knife-edge diffraction. *Radio Science*, 17 (6), 1541-1546

[Wagen94] Wagen, J-F, Rizk, K. 1998. Ray tracing based prediction of impulse response in urban microcells. In*: Proceedings of the 44th IEEE Vehicular Technology Conferences - VTC'94*, Stockholm, Sweden, IEEE, 210-214

[Walfisch88] Walfisch, J, Bertoni, H L. 1988. A theoretical model of UHF propagation in urban environments. *IEEE Trans. on Antennas and Propagation*, 36 (12), 1788-1796

[West99] West, J C. 1999. On iterative approaches for electromagnetic rough-surface scattering problems. *IEEE Trans. on Antennas and Propagation*. 47 (8), 1281-1288

[Winebrenner85] Winebrenner, D, Ishimaru, A. 1985. Application of the phase-perturbation technique to randomly rough surfaces. *Journal of the Optical Society of America*. 2 (12), 2285-2294

[Xia92] Xia, H H, Bertoni, H L. 1992. Diffraction of cylindrical and plane waves by an array of absorbing half-screens. *IEEE Trans. on Vehicular Technology*, 40(2), 170-177

[Xia93] Xia, H, et.al. 1993. Radio propagation characteristics for line-of-sight mocrocellular and personal communiaction. *IEEE Trans. on Antennas and Propagation*. 41 (10), 1439-1447

[Zwick00] Zwick, T, et.al. 2000. A stochastic spatial channel model based on wave-propagation modeling. *IEEE Journ. on selected areas in communications*. 18(1), 6-15

Appendix A. Polarisation dependant perturbation and Kirchoff theory

The methodology used to obtain vector solutions for perturbation theory and Kirchoff theory is described in e.g. [Ogylvi91]. Only the results will be repeated here.

Perturbation theory:

Assuming a linearly polarised plane wave incident wave, in general the average power for each of the polarisation combinations will be of the form

$$P_{\alpha\to\beta} = \frac{k^4 \Phi^P_{\alpha\to\beta}(\theta_i, \theta_s, \Delta\phi)}{r^2} A_M \, P(kA, kB) \qquad \textit{(eq. 123)}$$

where $\Phi^P_{\alpha\to\beta}$ is an angular factor dependant on polarisation, where $\alpha, \beta = v, h$. $P(s_1, s_2)$ is the surface power spectrum as described previously in Chapter 4. A_m is the surface size and *r* is the observation distance In the case of a perfectly conducting surface, the results are

$$\begin{aligned}
\Phi^P{}_{h\to h}(\theta_i, \theta_s, \Delta\phi) &= 4\cos^2\theta_i \cos^2\theta_s \sin^2\Delta\phi \\
\Phi^P{}_{h\to v}(\theta_i, \Delta\phi) &= 4\cos^2\theta_i \sin^2\Delta\phi \\
\Phi^P{}_{v\to v}(\theta_{i,}\theta_s, \Delta\phi) &= 4(\sin\theta_i \sin\theta_s + \cos\Delta\phi)^2 \\
\Phi^P{}_{v\to h}(\theta_s, \Delta\phi) &= 4\cos^2\theta_s \sin^2\Delta\phi
\end{aligned} \qquad \textit{(eq. 124)}$$

In the case of a non-perfectly conducting surface the expressions become slightly more complicated. The angular terms in this case can be written

$$\begin{aligned}
\Phi^P{}_{h\to h}(\theta_i, \theta_s, \Delta\phi) &= \frac{-(\varepsilon_r - 1)\cos\Delta\phi}{\left(\cos\theta_i + \sqrt{\varepsilon_r - \sin^2\theta_i}\right)\left(\cos\theta_s + \sqrt{\varepsilon_r - \sin^2\theta_s}\right)} \\
\Phi^P{}_{h\to v}(\theta_i, \theta_s, \Delta\phi) &= \frac{-(\varepsilon_r - 1)\sin\Delta\phi\sqrt{\varepsilon_r - \sin^2\theta_s}}{\left(\cos\theta_i + \sqrt{\varepsilon_r - \sin^2\theta_i}\right)\left(\varepsilon_r\cos\theta_s + \sqrt{\varepsilon_r - \sin^2\theta_s}\right)} \\
\Phi^P{}_{v\to v}(\theta_i, \theta_s, \Delta\phi) &= \frac{(\varepsilon_r - 1)\sin\theta_i \sin\theta_s + \cos\Delta\phi\sqrt{\varepsilon_r - \sin^2\theta_i}\sqrt{\varepsilon_r - \sin^2\theta_s}}{\left(\varepsilon_r\cos\theta_i + \sqrt{\varepsilon_r - \sin^2\theta_i}\right)\left(\varepsilon_r\cos\theta_s + \sqrt{\varepsilon_r - \sin^2\theta_s}\right)} \\
\Phi^P{}_{v\to h}(\theta_i, \theta_s, \Delta\phi) &= \frac{-(\varepsilon_r - 1)\sin\Delta\phi\sqrt{\varepsilon_r - \sin^2\theta_s}}{\left(\varepsilon_r\cos\theta_i + \sqrt{\varepsilon_r - \sin^2\theta_i}\right)\left(\cos\theta_s + \sqrt{\varepsilon_r - \sin^2\theta_s}\right)}
\end{aligned} \qquad \textit{(eq. 125)}$$

where ε_r is the relative permittivity of the scattering medium. Note that in neither case will there be any depolarisation in the incident plane, i.e. the direction $\Delta\phi = 180°$.

Kirchoff theory:

For Kirchoff theory a solution can be found in the special case of a perfectly conducting surface, when the reflection coefficients for the vertical and horizontal components will be $\Gamma_v = 1$ and $\Gamma_h = -1$, respectively. In this case the solution for the different combinations of polarisations can be found from

$$E_{s\_\alpha\to\beta} = \frac{jke^{jkr}}{4\pi r}\int_S (a_{\alpha\beta}h_x + b_{\alpha\beta}h_y - c_{\alpha\beta})\cdot\exp\left[jk\left(Ax_0 + By_0 + Ch(x_0, y_0)\right)\right]dx_0 dy_0 \qquad \textit{(eq. 126)}$$

where A, B and C are given in Chapter 4 and h_x and h_y are the derivative of the height function h in the x and y direction, respectively. The constants a, b and c are defined as follows for the different combinations of polarisations

$$\begin{aligned}
a_{vv} &= 2\sin\theta_s & b_{vv} &= 0 & c_{vv} &= -2\cos\theta_s\cos\Delta\phi \\
a_{vh} &= 0 & b_{vh} &= 0 & c_{vh} &= -2\sin\Delta\phi \\
a_{hh} &= 2\sin\theta_i\cos\Delta\phi & b_{hh} &= -2\sin\theta_i\sin\Delta\phi & c_{hh} &= -2\cos\theta_i\cos\Delta\phi \\
a_{hv} &= -2\sin\theta_i\cos\theta_s\sin\Delta\phi & b_{hv} &= 2(-\sin\theta_i\cos\theta_s\cos\Delta\phi + \cos\theta_i\sin\theta_s) & & \textit{(eq. 127)} \\
c_{hv} &= 2\cos\theta_i\cos\theta_s\sin\Delta\phi & & & &
\end{aligned}$$

In the case of Gaussian height statistics the *coherent* electric field can be written

$$E_{coh\_\alpha\to\beta}(\mathbf{r}) = e^{-g/2}\cdot E_{0\_\alpha\to\beta} \qquad \textit{(eq. 128)}$$

where $E_{0\_\alpha\to\beta}$ is the polarisation dependant electric field in the case of a smooth surface and g is defined in Chapter 4. In the case of a rectangular surface of extent $-X \le x_0 \le X, -Y \le y_0 \le Y$ the form of E_0 is

$$E_{0\_\alpha\to\beta} = -\frac{jke^{jkr}}{4\pi r}A_M c_{\alpha\beta}\left(\frac{\sin kAX}{kAX}\right)\left(\frac{\sin kBY}{kBY}\right) \qquad \textit{(eq. 129)}$$

where $c_{\alpha\beta}$ is as defined above.

For the diffuse field, like in the scalar case, the power is described as an infinite sum that can be truncated in the cases of slightly rough and medium rough surfaces. For *slightly rough surfaces* the power can be written

$$P_{diff\_\alpha\to\beta} = \frac{k^4\Phi^K_{\alpha\to\beta}(\theta_i, \theta_s, \Delta\phi)}{r^2}A_M P(kA, kB) \qquad \textit{(eq. 130)}$$

where the angular, polarisation dependant terms $\Phi^K_{\alpha\to\beta}$ are

$$\begin{aligned}
\Phi^K_{v\to v}(\theta_i,\theta_s,\Delta\phi) &= 4(\sin\theta_i\sin\theta_s+\cos\theta_i\cos\theta_s\cos\Delta\phi+\cos\Delta\phi)^2\\
\Phi^K_{v\to h}(\theta_i,\theta_s,\Delta\phi) &= 4\sin^2\Delta\phi(\cos\theta_i+\cos\theta_s)^2\\
\Phi^K_{h\to h}(\theta_i,\theta_s,\Delta\phi) &= \Phi^K_{v\to v}(\theta_i,\theta_s,\Delta\phi)\\
\Phi^K_{h\to v}(\theta_i,\theta_s,\Delta\phi) &= \Phi^K_{v\to h}(\theta_i,\theta_s,\Delta\phi)
\end{aligned} \qquad \textit{(eq. 131)}$$

In the case of *very rough surfaces*, defined as $g>>1$, the total average power P_{tot} can be estimated as

$$P_{tot}=\frac{k^2F^2_{\alpha\to\beta}\sigma^2}{r^2}\cdot\frac{1}{g}\cdot A_M\cdot p_{12}\left(\frac{A}{C},\frac{B}{C}\right) \qquad \textit{(eq. 132)}$$

where the angular and polarisation dependant terms $F_{\alpha\to\beta}$ are defined as

$$F^2_{\alpha\to\beta}=\frac{\Phi^K_{\alpha\to\beta}}{C^2} \qquad \textit{(eq. 133)}$$

and p_{12} is defines in Chapter 4. L_0 and σ are the surface correlation length and the standard deviation of the height variation as described in Chapter 4.

URN:NBN:no-1290

Appendix B. The statistics of the resulting fieldstrength in the amplitude/phase model

As described in Chapter 5, the resulting complex fieldstrength can in accordance with the amplitude/phase model assumption be written as

$$a_r = a_t \sum_m \sum_n T(m,n) \qquad \textit{(eq. 134)}$$

where a_t is the transmitted fieldstrength and T([m,n]) are the complex transfer functions via the individual subsurfaces ([m,n]). This is consistent with the concept of a *spread matrix*, where the relationship between the power *P* and the complex fieldstrength *a* is given as $a \cdot a^* = |a|^2 = P$. The equation above can also be written

$$a_r = \rho e^{j\chi} = u + jv = \sum_m \sum_n w_{mn} e^{j\phi_{mn}} \qquad \textit{(eq. 135)}$$

where w_{mn} and ϕ_{mn} are the amplitudes and phases of the contributions from each subsurface, respectively. This means that the resulting field is a "random walk", where the w_{mn} are the step lengths and ϕ_{mn} are the directions of each step (see Figure 21, Chapter 5). When the number $(m \cdot n)$ is large, as will be the case, the resulting real (u) and imaginary (v) parts of the resulting field will be approximately Gaussian by the *central limit theorem*.

For analytical solutions to be possible it must be assumed that *u* and *v* are independent. In this case the Gaussian bivariate probability distribution function is written as

$$p(u,v) = \frac{1}{2\pi\sigma_u\sigma_v} e^{\left\{-\left[\frac{(u-u_0)^2}{2\sigma_u{}^2} + \frac{(v-v_0)^2}{2\sigma_v{}^2}\right]\right\}} \qquad \textit{(eq. 136)}$$

where u_0 and v_0 are the expectation values and σ_u and σ_v are the standard deviations of the real and imaginary parts. If in addition it is assumed that the variances of the real and imaginary parts are equal, i.e. that $\sigma_u=\sigma_v$, it can be shown (e.g. [Ogilvy91]) that the distribution of the *amplitude* ρ of the resulting field can be written

$$p(\rho) = \frac{\rho}{\sigma_0{}^2} e^{\left[-\left(\frac{\rho^2+a^2}{2\sigma_0{}^2}\right)\right]} I_0\left(\frac{\rho a}{\sigma_0{}^2}\right) \qquad \textit{(eq. 137)}$$

where I_0 is the zeroth order modified Bessel function of the first kind. This is the *Rice distribution*, and can be interpreted as the sum of a coherent, non-random component with amplitude *a* and a Rayleigh distributed random vector. The expectation value of this distribution can be shown to be (e.g. [Harman63])

$$E(\rho) = \sqrt{\frac{\pi}{2}}\sigma_0 e^{-\frac{a^2}{4{\sigma_0}^2}}\left[\left(1+\frac{a^2}{2{\sigma_0}^2}\right)\cdot I_0\left(\frac{a^2}{4{\sigma_0}^2}\right)+\frac{a^2}{2{\sigma_0}^2}\cdot I_1\left(\frac{a^2}{4{\sigma_0}^2}\right)\right] \qquad \textit{(eq. 138)}$$

where I_1 is the first order modified Bessel function of the first kind.

When the coherent component is much larger than the diffuse one, the distribution is close to Gaussian, with expectation value a and variance $2\cdot{\sigma_0}^2$ and can be written

$$p(\rho) = \frac{1}{\sqrt{2\pi{\sigma_0}^2}}\cdot e^{-\frac{(\rho-a)^2}{2{\sigma_0}^2}} \qquad \textit{(eq. 139)}$$

For relatively smooth surfaces this will be the case close to the specular direction. When there is no coherent component, as will be the case in directions far away from the specular and for completely rough surfaces, the distribution is Rayleigh. In this case the amplitude distribution is only dependant on one parameter, σ_0, and can be written

$$p(\rho) = \frac{\rho}{{\sigma_0}^2}e^{-\frac{\rho^2}{2{\sigma_0}^2}} \qquad \textit{(eq. 140)}$$

The properties of the Rayleigh distribution are

$$\begin{aligned} E(\rho) &= 1.25\cdot\sigma_0 \\ E(\rho^2) &= 2\cdot{\sigma_0}^2 \\ STD(\rho) &= \frac{1}{1.52}\cdot\sigma_0 \end{aligned} \qquad \textit{(eq. 141)}$$

The relationship between Rice and Rayleigh distributions can be illustrated graphically as in Figure 59. The component a is the constant, non-random, coherent component. The distance ρ_σ is Rayleigh distributed with parameter σ_0, whereas the pointing direction α of ρ_σ is uniformly distributed ([0°, 360°]). The resulting distance ρ will then be Rice distributed as described above.

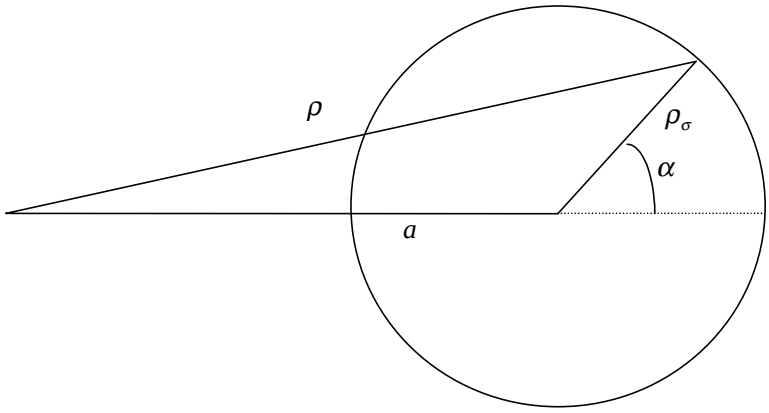

Figure 59. Graphical illustration of relationship between Rice and Rayleigh distributions.

The *K-factor* is often used as a measure of the coherent to diffuse power and is defined as

$$K = \frac{a^2}{2\sigma_0{}^2} \qquad \textit{(eq. 142)}$$

Although the above discussion shows that the distribution of the fieldstrength amplitude in all direction will be Ricean, the parameters a and σ_0 will of course be functions of direction. The coherent component *a* can be found by realising that *a* is the *absolute value of the complex expectation value of the fieldstrength* (compare with Figure 59), which itself is the sum of the independent random processes of the contributions from the individual squares. The value of the contribution from square [m,n] is given as

$$a(\Phi)_{mn} = w_{mn} e^{j\cdot(\phi_{mn}+\Phi)} \qquad \textit{(eq. 143)}$$

where Φ is the *phase shift* as described in Chapter 5 and w_{mn} and ϕ_{mn} are the amplitude and phase contributions, respectively. Keeping in mind that the *phase shift* in each square is assumed uniformly distributed in the interval $[-\Phi_0/2, \Phi_0/2]$ the expectation value in this case is given as

$$E(a_{mn}) = \int_{-\Phi_0/2}^{\Phi_0/2} w_{mn} e^{j(\phi_{mn}+\phi)} \cdot \frac{1}{\Phi_0} d\phi = w_{mn} e^{\phi_{mn}} \int_{-\Phi_0/2}^{\Phi_0/2} \left[\cos(\phi) - j\cdot\sin(\phi)\right] \cdot \frac{1}{\Phi_0} d\phi =$$

$$\frac{\sin(\Phi_0/2)}{\Phi_0/2} \cdot w_{mn} e^{j\phi_{mn}}$$

(eq. 144)

which means that the expectation value has the same direction (phase) as in the case of no phase shift (plane surface) and is weighted with the factor $\frac{\sin(\Phi_0/2)}{(\Phi_0/2)} = \mathrm{sinc}(\Phi_0/2)$. This is illustrated in Figure 60. For values of Φ_0 below 180° this function can be approximated within an error of 3 % by $\mathrm{sinc}(\Phi_0/2) = \cos(\Phi_0/\sqrt{12}) = \cos(\Phi_{rms})$ where Φ_{rms} is the rms phase shift. The total expectation value is given as

$$E(a) = \mathrm{sinc}(\Phi_0/2) \cdot \sum_m \sum_n w_{mn} e^{j \cdot \phi_{mn}} = \mathrm{sinc}(\Phi_0/2) \cdot a_p \qquad \textit{(eq. 145)}$$

where a_p is the fieldstrength in the plane surface (no phase shift) case. This also means that the coherent component can be written

$$a_{coh} = \mathrm{sinc}(\Phi_0/2) \cdot \Gamma \cdot a_0 \qquad \textit{(eq. 146)}$$

where Γ is the reflection coefficient (Chapter 2), and a_0 is the fieldstrength in the case of a plane, perfectly conducting surface of the same size. This shows that the coherent scattered component from the rough surface can be found by using standard techniques, for instance by solving for the boundary conditions and using the surface equivalence theorem [Balanis89]. These are techniques well known from e.g. antenna theory.

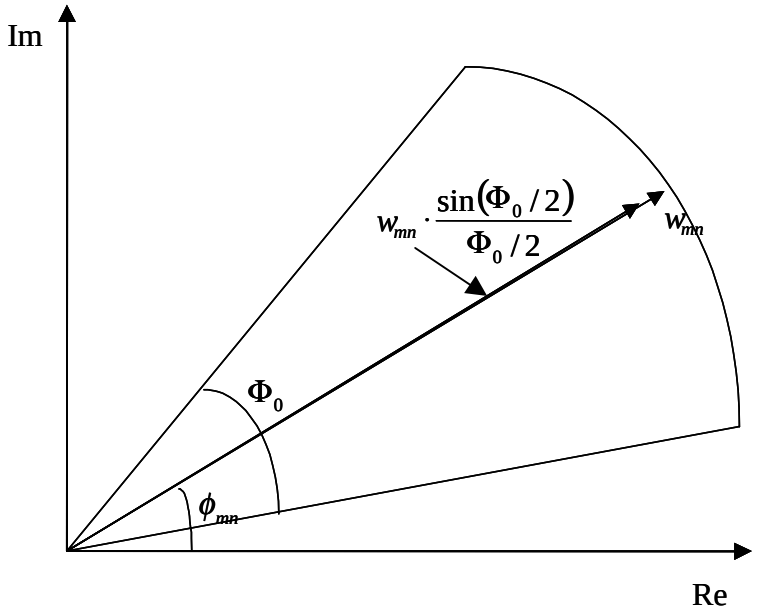

Figure 60. The expectation value of the complex contribution from one square [m,n] has the same phase as in the plane surface case

The distribution of diffuse power in the angle space will have the same shape as the scattering from the individual squares *da* [Kaplan86][41], which means that it is circular symmetric and follows

$$P_{\text{diff}} \sim (1+\cos\theta_s)^2 \qquad \textit{(eq. 147)}$$

The value of the diffuse power can then be found from arguments of preservation of power. The power that illuminate the surface can be divided into three parts; P_{loss} , the power loss due to ohmic losses and refraction; P_{coh} , the specular, non-random part and P_{diff} , the diffuse part that is due to the roughness. If the total illumination power is denoted P_{tot} , this can be written as

$$P_{tot} = P_{loss} + P_{coh} + P_{diff} \qquad \textit{(eq. 148)}$$

P_{coh} has been shown above to be

$$P_{coh} = \Gamma^2 \cdot \text{sinc}^2(\Phi_0 / 2) \cdot P_{tot} \qquad \textit{(eq. 149)}$$

and it is also known that

$$P_{loss} = (1 - |\Gamma|^2) \cdot P_{tot} \qquad \textit{(eq. 150)}$$

By comparing with equation 15 it then follows that

$$P_{diff} = P_{tot} \cdot \Gamma^2 \cdot \left[1 - \text{sinc}^2(\Phi_0 / 2)\right]. \qquad \textit{(eq. 151)}$$

From eq. 151 and the relationship in eq. 147 the average diffuse power density S_{diff} as a function of scattering direction at an observation distance R_r can be shown to be

$$S_{diff}(\theta_s) = \frac{P_{tot} \cdot 3}{16\pi {R_r}^2} \cdot \Gamma^2 \cdot \left[1 - \text{sinc}^2(\Phi_0 / 2)\right] \cdot (1+\cos\theta_s)^2 . \qquad \textit{(eq. 152)}$$

[41] This can be shown by a 2 dimensional Fourier transform of the complex signal over the surface and inspect the resulting angular domain description.

Appendix C. Measurement equipment

Non-grazing set-up

General build-up

The equipment is illustrated schematically in Figure 29, Chapter 5. The transmitting antenna was a $d_t = 1.8m$ parabolic antenna and the receiving antenna was a $d_r = 0.9m$ parabolic antenna. The Rx antenna was mounted on a 4-meter high construction so that the pointing angle towards the surface could easily be altered, but the antenna was always pointing towards the same position on the ground, which was also the Tx antenna pointing position. The received power was monitored by a spectrum analyser and logged by a PC. A picture of the receiver set-up is shown in Figure 61.

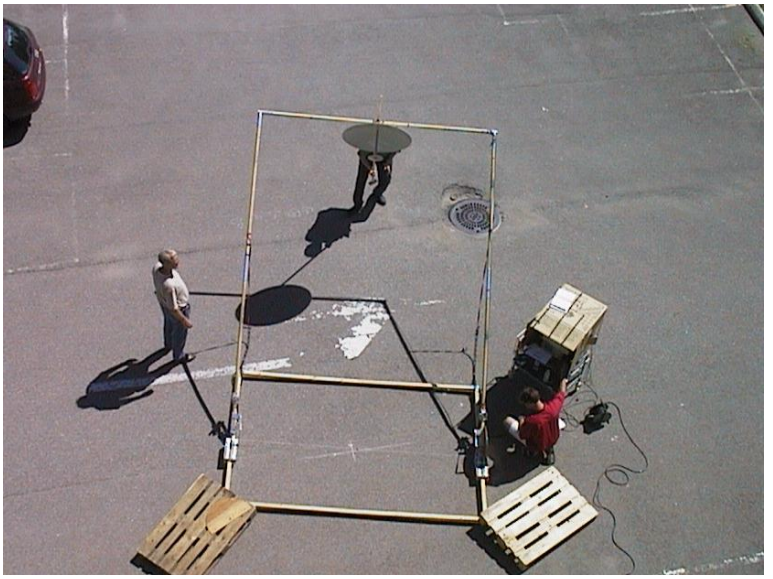

Figure 61. Picture of the receiver set-up, non-grazing

The antennas were illuminated uniformly, which leads the theoretical power radiation pattern to be symmetrical and given by (e.g. [Gagliardi91])

$$g(\beta) = \left(\frac{\pi d}{\lambda}\right)^2 \cdot \left(\frac{2 \cdot J_1(\frac{\pi d}{\lambda}\sin\beta)}{\frac{\pi d}{\lambda}\sin\beta}\right)^2 \qquad \textit{(eq. 153)}$$

where $J_1(x)$ is the Bessel function of the first kind of the first order, β is the angle away from the main beam direction and d is the antenna diameter. The *half-power beamwidth (HPBW)* of such an antenna is

$$HPBW[rad] = \frac{1.02\lambda}{d} \qquad \textit{(eq. 154)}$$

A picture of the Tx antenna in a measurement series is shown in Figure 62. The antenna radiation patterns were also measured on a calibrated antenna measurement facility to minimise the estimation error (Chapter 5). The achieved accuracy in these measurements is sufficient for the analysis of the scattering properties. The Rx antenna has a maximum gain of 20.7 dB and a HPBW of 12.7° in E-plane and 11.8° in H-plane. The radiation patterns are shown in Figure 63. The Tx antenna has a maximum gain of 28.3 dB and a HPBW of 6.2° in E-plane and 6.1° in H-plane, respectively. The patterns are shown in Figure 64.

Figure 62. Picture of Tx-antenna, non-grazing set-up

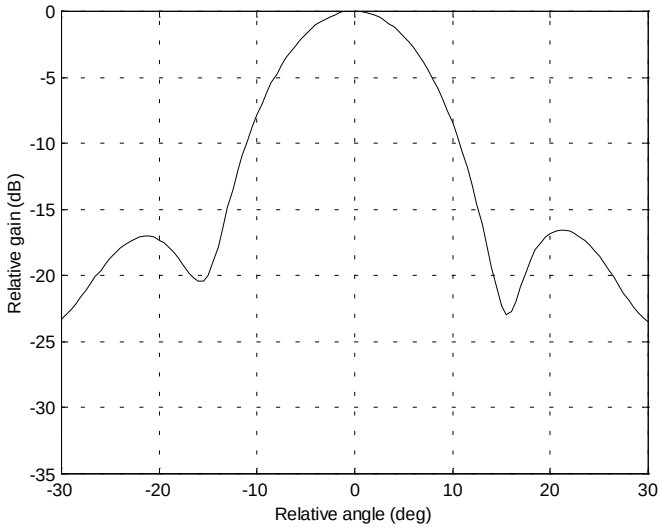

a)

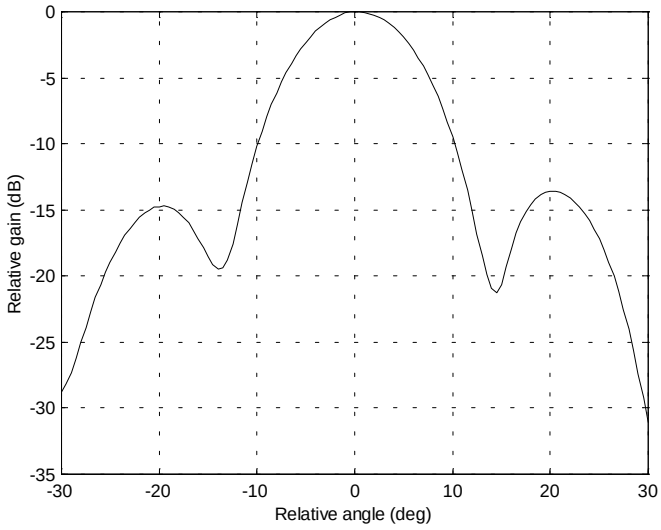

b)

Figure 63. Rx-antenna diagram, non-grazing set-up; a) E-plane, b) H-plane

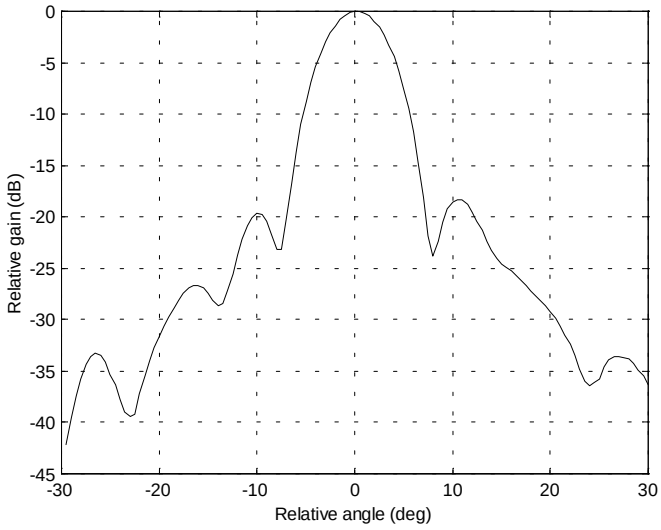

a)

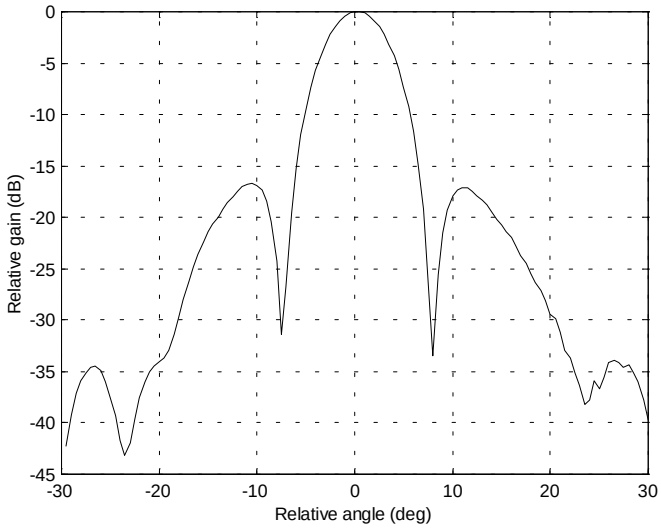

b)

Figure 64. Tx-antenna diagram, non-grazing set-up; a) E-plane, b) H-plane.

The 3-dB contour on the ground are ellipses with minor axis

$$a_{\text{minor}} = 2 \cdot R \cdot \sin\left(\frac{HPBW}{2}\right) \qquad \textit{(eq. 155)}$$

and major axis

$$a_{major} = 2 \cdot R \cdot \frac{\sin(HPBW/2)}{\sin\psi} \qquad \textit{(eq. 156)}$$

where R is the distance to the point of maximum illumination and ψ is the complement of the incidence angle θ_i, as shown in Figure 65. This is important as in the experiments possible error reflection sources had to be kept far enough from the illuminated area to not interfere with measurements. In particular the wooden frame that can be seen in Figure 61 had to be made large enough not to interfere with the experimental results. In all the experiments performed the receiving antenna illuminated the smallest area and therefore restricted the area from which scattering contributions were received. Table 9 shows the major and minor axis in the cases of incidence angles 0°… 70°. The Table shows that the values always are considerable smaller than the frame which was approximately 4 m 4 m. The antenna gain towards the frame was always reduced by at least 15 dB compared to maximum direction for all measurements.

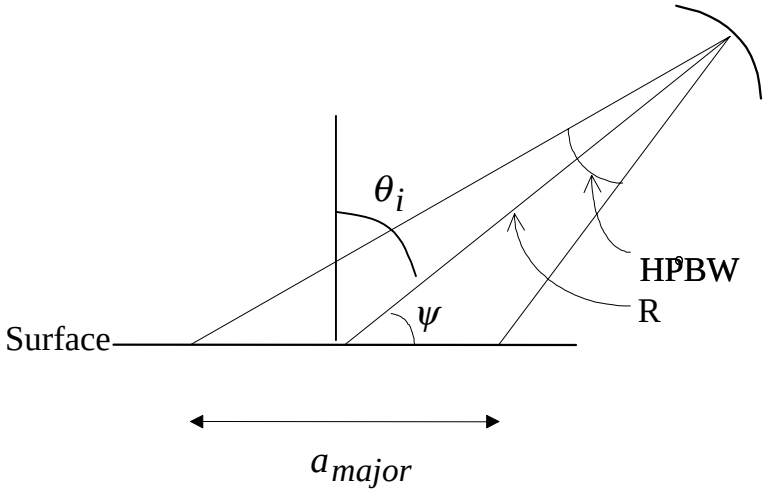

Figure 65. Plane through point of illumination and antenna, non-grazing set-up

Inc. angle [deg]	**a_{major} [m]**	**a_{minor} [m]**
0	0.84	0.84
10	0.85	0.84
20	0.89	0.84
30	0.97	0.84
40	1.09	0.84
50	1.30	0.84
60	1.67	0.84
70	2.45	0.84

Table 9. Major and minor axis of the half power illuminated area for the Rx antenna

Measurements were performed by recording the received power level while lowering the Rx antenna at constant speed. This was repeated for different values of $\Delta\phi$. The parameters used in the measurement set-up are listed in Table 10. Note that the measurements were performed with a monochromatic signal.

System:	
Frequency	1625 MHz
Bandwidth	0 Hz
Rx Power	-9.5 dBm
θi	70°, 60°, 45°, 30°[42]
θs	0°…65° (70°[43])
$\Delta\phi$	135°, 140°, …185°
Spectrum analyzer:	
Resolution bandwidth	100 kHz
Sweep time	50 ms
Average samples	5

Table 10. Measurement parameters, non-grazing *measurements*

Far-field verification

Tests were performed to inspect whether the antenna gains differs from the measured antenna patterns due to the antennas being used at Tx-Rx-distances slightly less than common far field assumptions[44]. Firstly the Tx was positioned at the shortest distance from the scattering surface that was to be used, which was at R_t=14 meters and θ_i=60°. R_r remained at 4 meters and the receiving antenna was positioned at the angle of maximum reception (the mirror angle, θ_s=60°, $\Delta\phi$=180°). Polarisation was vertical on both antennas. The illuminated area was then covered by a 2m 1m metal plate, simulating an ideal ground plane. Using this set-up and a transmitted power of P_t=-9.5 dBm the maximum received power was –30.5 dBm. The link budget equation was used to perform measurements of the antenna gain.

$$P_r[dB] = P_t[dB] - L_{fs}[dB] + G_t[dB] + G_r[dB] - L_{cr}[dB] \qquad \textit{(eq. 157)}$$

where L_{fs} is the free space loss, G_t and G_r are the transmitting and receiving antenna gains respectively and L_{cr} is the cable loss. In this case L_{fs} =61.7 dB and L_{cr} =9.1 dB giving G_t+G_r=49.8 dB. The measured value, as shown earlier in this appendix is G_t+G_r=28.3 dB+20.7

[42] Not all angles were measured on all surfaces, see Chapter 5 for details.

[43] Only used for θ_i=70°.

[44] A common definition of the minimum far field distance is $R>2D^2/\lambda$ [Balanis89], where D is the largest dimension in the antenna. This gives 8.8 m for the 0.9 m antenna and 35 m for the 1.8 m antenna.

dB=49.0 dB. This is a close fit, showing that the metal plate can be regarded as a ground plane and also that the antennas have gains similar to the far-field gains at the lowest distances used.

The experiment was then repeated with the antennas pointing directly towards each other at a distance of 15 meters. The same calculation in this case resulted in G_t+G_r=48.1 dB. This latter type of experiment was repeated at a Tx-Rx-distance of 55 meters, which is well above the far field limit. In this case the calculations showed G_t+G_r=48.3 dB. The fact that the experiment gave almost the same result at 15 m as at 55 m confirms that the antenna gains were not affected by the relatively low Rx-Tx-distances used.

Isolation

The *isolation* (*S*) between the Tx and Rx antennas is defined as the difference between the received signal level assuming no scattering loss in the reflection (smooth surfaces with reflection coefficient $|\Gamma| = 1$) and the "leakage" signal received directly from one antenna to the other. This can be written as

$$S[dB] = \frac{G_{r\_\max}}{G_r(\beta_r)}[dB] + \frac{G_{t\_\max}}{G_t(\beta_t)}[dB] + \frac{R^2}{(R_r + R_t)^2}[dB], \qquad \textit{(eq. 158)}$$

where the angles β_r and β_t are defined by Figure 66 and *R* is the distance between Tx and Rx. The first two terms are due to the difference in antenna gain between the maximum direction (towards maximum illumination on the ground) and the direction towards the other antenna. The last term is due to the difference in path loss between the reflected and the direct components. S is a function of R_r and R_t and of the orientation angles θ_i, θ_s and $\Delta\phi$. It is desireable that *S* is as large as possible. Typical values of S in the described measurements were above 40 dB for the maximum directions.

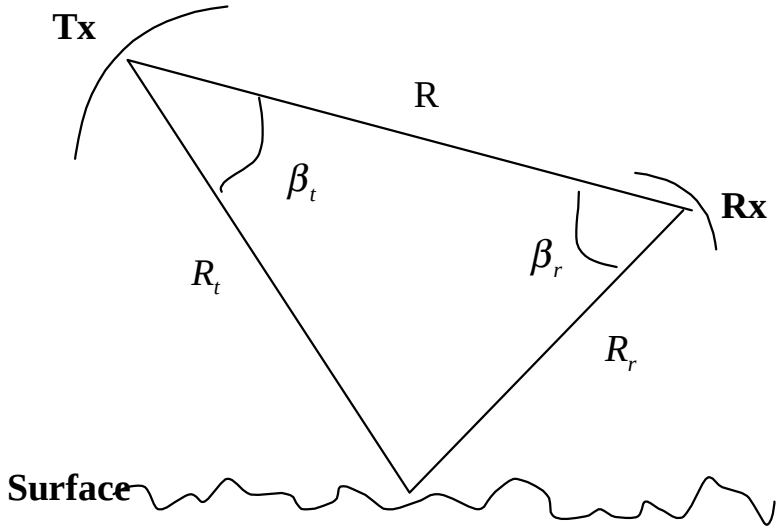

Figure 66. Definition of angles for calculation of the isolation, non-grazing set-up

In order to calculate the noise threshold for each measurement point (a fixed R_t and θ_i) the *minimum* S (S_{min}) for the point is found. The noise threshold gives the *sensitivity* of the measurement and is given simply by

$$N = P_{\max}[dB] - S_{\min}[dB] + \text{margin} \qquad \textit{(eq. 159)}$$

where P_{max} is the theoretically largest received power, the power received if the reflection coefficient of the surface has absolute value of 1. *S* provides the dynamic range of the measurement. The margin should be large enough to provide the direct component from contributing to the total received power, and was for the experiments chosen to be 5 dB. For all the experiments the measured values were compared to the noise threshold to make sure the signal measured was not affected be the direct radiated signal. Typical values of N in the described measurements were below –60 dBm, for the maximum directions. Almost no measurements below noise threshold were observed in any of the experiments.

Grazing set-up

The equipment is illustrated schematically in Chapter 5. The set-up is similar to the one described e.g. in [Aanvik97]. It uses a channel sounder able to measure the wideband complex channel response. The complex impulse response (CIR) was recorded on each of the eight elements in an eight-element antenna array. By using the phase information of the CIRs from each antenna element, the Direction of Arrival (DoA) in azimuth angle associated with each multipath component could be estimated.

A large number of methods to perform the DoA estimation exist. The simplest implementation is the Fourier-algorithm, which is based on a Fourier-transform on the signals received along the array. However, so-called *super resolution methods* show much better performance with respect to angular resolution by assuming the incoming signal to be a finite number of plane waves.

By positioning the transmitter and receiver over the surface to be inspected, and by flipping the array vertically, the set-up was able to resolve reflected components from the ground from the direct component. The reflected, incoming waves could then be separated in the vertical plane. A picture of the transmitting side is shown in Figure 67 and a picture of the receiving side is shown in Figure 68. The antennas were arranged so that the specular reflecting component would arrive at approximately 10° relative to the direct component.

Figure 67. Grazing set-up, transmitting side

Figure 68. Grazing set-up, receiving side

Two super-resolution directional estimation methods were tested; the SAGE *(Space-Alternating Generalised Expectation-maximisation)* algorithm and the ESPRIT *(Estimation of Signal Parameters via Rotational Invariance Techniques)* algorithm. The SAGE method is based on using the expectation-maximisation (EM) algorithm to compute the maximum

likelihood (ML) estimate of the desired set of parameters (e.g. [Lehne98]). The ESPRIT algorithm is a so-called *subspace method*, the main principle being that the eigenvectors of the signal correlation matrix corresponding to the noise are orthogonal to the signal steering vectors. It was decided to use the ESPRIT algorithm because it seemed to have a slightly better angular resolution, which is essential in this type of experiment. Typically a resolution down to a few degrees can be achieved, depending on the signal-to-noise-ratio and the accuracy in the measured antenna diagram.

A log-periodic antenna was used on the transmitting side. The antenna had a HPBW of 97° in H-plane and a gain of 7.5 dB. It was important that the gain in the direction towards the Tx antenna and towards the points of reflection were the same, because the ESPRIT algorithm did not calibrate for the Tx antenna diagram. This was achieved by using an antenna pointing direction slightly below horizontal. The antenna could be flipped so that both vertical and horizontal Tx could be tested. The Rx array-antenna was a cavity-backed broadband microstrip antenna [Skyttemyr99]. The element gains were approximately 7 dB and the HPBW approximately 90°. Since the antenna was dual-polarised, both polarisations could be measured also on the receiving side. Figure 69 shows measured element diagrams for the horizontal elements, measured in E-plane. Figure 70 shows measured element diagrams for the vertical elements, measured in H-plane.

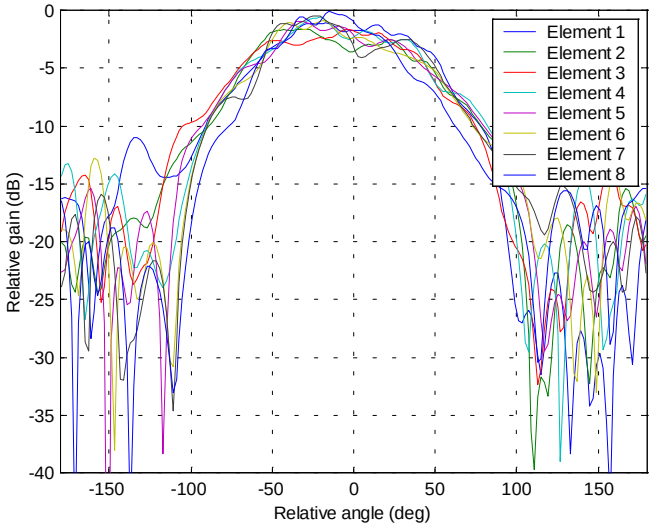

Figure 69. Element diagrams, receiving antenna, grazing set-up, horizontal elements, measured in E-plane

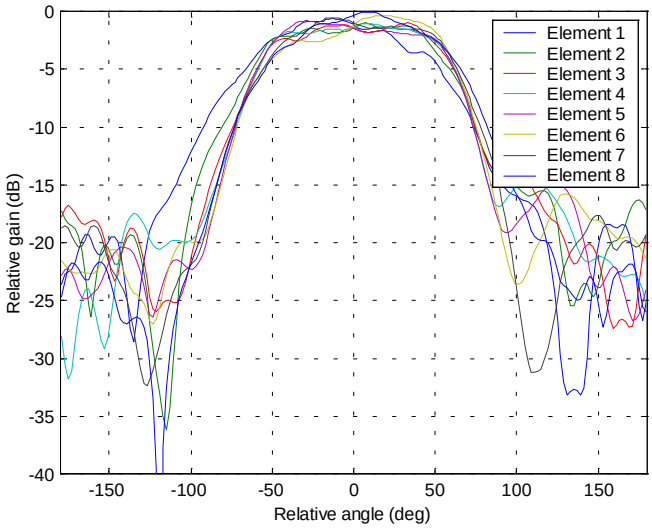

Figure 70. Element diagrams, receiving antenna, grazing-set-up, vertical elements, measured in H-plane

The measurement parameters are listed in Table 11.

Frequency	2.1 Hz
Bandwidth	50 MHz
Time to measure all elements	1 ms
Measurement frequency	5 Hz

Table 11. Measurement parameters, grazing set-up

URN:NBN:no-1290

Appendix D. Detailed steps in the method of analysis for the amplitude/phase model

Non-grazing set-up

As described in Chapter 5, the analysis starts with the estimation of the Rice parameters $a(\theta_s, \Delta\phi)$ and $\sigma_0(\theta_s, \Delta\phi)$ for each measurement series in the directions in which power measurements were performed. This was done in a least square sense, which can be written

$$[a \quad \sigma_0]_{opt} = \min_{[a \quad \sigma_0]} \sum_{\theta_s} \sum_{\Delta\phi} \left(\tilde{\rho}(\theta_s, \Delta\phi) - E_\rho(\theta_s, \Delta\phi)\right)^2 \qquad \textit{(eq. 160)}$$

where $\tilde{\rho}$ was the measured amplitude in each direction, and E_ρ was the expectation value of the amplitude from the amplitude/phase model given the current values of $[a \quad \sigma_0]$.

Test cases showed that this method gave slightly uncertain estimates for σ_0 for very smooth surfaces, when the rms phase variations of the surface were small, because imperfections in the measurement set-up lead to uncertainties of the same order of magnitude as the measurement values in the directions furthest away from the specular directions. Therefore a different approach was used in these cases. In the directions furthest from specular (typically more than 40º from maximum direction) the diffuse components would dominate and the distribution would be approximately Rayleigh. Therefore the σ_0 in these directions could be estimated as[45]

$$\sigma_{0\_est} = \frac{\bar{\rho}}{1.25} \qquad \textit{(eq. 161)}$$

where $\bar{\rho}$ is the mean value of the measured amplitudes in this *Rayleigh area*[46], or alternatively by calculating the standard deviation of the measured values using numerical methods and estimating σ_0 as[47]

$$\sigma_{0\_est} = 1.52 \cdot STD(\rho) \qquad \textit{(eq. 162)}$$

These two methods provided consistent results.

From the estimated σ_0 and *a*, the desired values Γ and Φ_0 could be calculated using arguments of preservation of power as described below. Γ and Φ_0 are functions of θ_s and $\Delta\phi$, which are omitted for clarity.

[45] In the Rayleigh distribution the expectation value is $E(\rho)=1.25\ \sigma_0$

[46] If the area over which the average was calculated was over a significant range of θ_s-values, the cos-variation of σ_0 had to be taken into account.

[47] In the Rayleigh distribution the standard deviation is $STD(\rho)=(1/1.52)\cdot\sigma_0$

Detailed steps in the method of analysis for the amplitude/phase model

The power that illuminates the surface (P_{tot}) can always be divided into three parts; P_{loss}, the power loss in the ground and refraction, P_{coh}, the specular, non-random part and P_{diff}, the diffuse part that is due to the roughness. This can be written as

$$P_{tot} = P_{loss} + P_{coh} + P_{diff} \qquad \textit{(eq. 163)}$$

or alternatively as values normalised to the total power, so that

$$\overline{P}_{loss} + \overline{P}_{coh} + \overline{P}_{diff} = 1 \qquad \textit{(eq. 164)}$$

Using preservation of power, $\overline{P}_{coh}$ can be found as

$$\overline{P}_{coh} = \frac{\oiint a^2 ds}{\oiint {a_0}^2 ds} \qquad \textit{(eq. 165)}$$

where the integration can be over any closed surface over the half sphere above the illuminated surface. This reduces to

$$\overline{P}_{coh} = \left(\frac{a}{a_0} \right)^2 \qquad \textit{(eq. 166)}$$

since the ratio a / a_0 is a constant at different angles as shown in Appendix B.

Similarly, $\overline{P}_{diff}$ can be estimated using the relationship

$$\overline{P}_{diff} = \frac{\oiint S_{diff} ds}{\oiint {a_0}^2 ds} \qquad \textit{(eq. 167)}$$

where S_{diff} is the diffuse power density in any direction. The integral in the nominator of eq. 167 can be evaluated using the relationship

$$S_{diff} = 2{\sigma_0}^2 . \qquad \textit{(eq. 168)}$$

Since $\overline{P}_{loss} = 1 - |\Gamma|^2 = 1 - \overline{P}_{coh} - \overline{P}_{diff}$, Γ can then be estimated from

$$\Gamma^2 = \overline{P}_{coh} + \overline{P}_{diff} \qquad \textit{(eq. 169)}$$

The total power scattered from the illuminated surface can be written

$$P_s = \iint a_0^2 \Gamma^2 dS \qquad \textit{(eq. 170)}$$

The coherent, non-random part of this power can be written, as shown in Appendix B, as

$$p_{coh} = \iint a_0^2 \Gamma^2 \mathrm{sinc}^2(\Phi_0 / 2) ds = P_s \cdot \mathrm{sinc}^2(\Phi_0 / 2) \qquad \textit{(eq. 171)}$$

Using preservation of power, the remaining power must be the diffuse, omnidirectional part. This can be written

$$P_{diff} = P_s - P_{coh} = P_s (1 - \mathrm{sinc}^2(\Phi_0 / 2)), \qquad \textit{(eq. 172)}$$

where P_{diff} is known from before to be

$$P_{diff} = \iint 2\sigma_0^2 ds . \qquad \textit{(eq. 173)}$$

This gives the desired relationship for the phase variation

$$\Phi_0 = 2 \cdot \mathrm{sinc}^{-1} \sqrt{1 - \frac{P_{diff}}{P_s}} \qquad \textit{(eq. 174)}$$

which is used for the estimation of Φ_0 in the measurements. As discussed in Chapter 5 there is a direct relation ship between Φ_0 and the desired height variation Δh. Sometimes the rms values h_{rms} and Φ_{rms} are desired, these can be found using $\Phi_{rms} = \Phi_0 / \sqrt{12}$.

Figure 71 shows an example of the relationship between the phase shift Φ_0 and the amount of diffuse power for different values of Γ. When the value of Φ_0 reaches 2π, the surface is *completely rough*, and all the scattered power is diffuse, therefore the curves flatten. Note that in the case $\Gamma = 1$ this means that all the illuminating power (P_{tot}) goes into diffuse scattering.

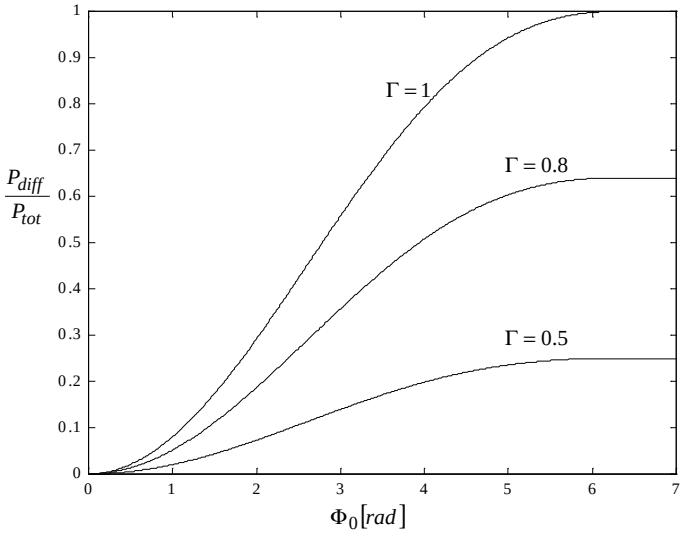

Figure 71. Relationship between the phase shift (Φ_0) and the relative amount of diffuse power, P_{diff}/P_{tot}

For smooth surfaces, where Φ_0 (or Φ_{rms}) are small there is an approximately linear relationship with the Rayleigh parameter σ_0. This is illustrated in Figure 72, which shows an example from a computer generated test case.

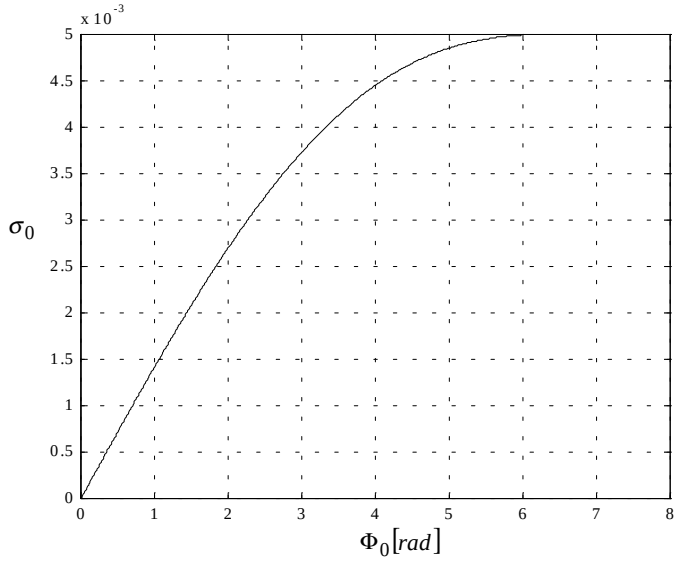

Figure 72. Relationship between the phase shift (Φ_0) and the Rayleigh parameter σ_0

The estimation method can be summarised as follows:

Detailed steps in the method of analysis for the amplitude/phase model

1. Estimate the Rice parameters from the measurements using the fact that the amplitude in all directions will be Ricean distributed with parameters $a(\theta_s, \Delta\phi) = \hat{a} \cdot a_0(\theta_s, \Delta\phi)$ and $\sigma_0(\theta_s, \Delta\phi) = \hat{\sigma}_0 \cdot (1 + \cos\theta_s)$.
2. Estimate Γ by calculating the amount of power in the coherent and diffuse parts of the scattering and using preservation of power.
3. Estimate Φ_0 (and Φ_{rms}) from the relationship between diffuse and scattered power as given in eq. 174.

Grazing set-up

As described in Chapter 5 the analysis of the grazing measurements starts with the estimation of the reflection coefficient Γ using the outputs from the ESPRIT-algorithm.

To estimate the diffuse part of the scattered signal, which would enable the estimation of the roughness related phase parameter Φ_0, it was necessary to take one step back and inspect the total signal impinging on the channel sounder receiver. The ESPRIT algorithm expects the received signal as a sum of plane waves, while the A/P model will lead to a description of the received signal as a sum of two plane waves (*direct, free space* and *coherent, reflected*) as well as a *diffuse, continuous, random signal spectrum*. This is illustrated in Figure 73.

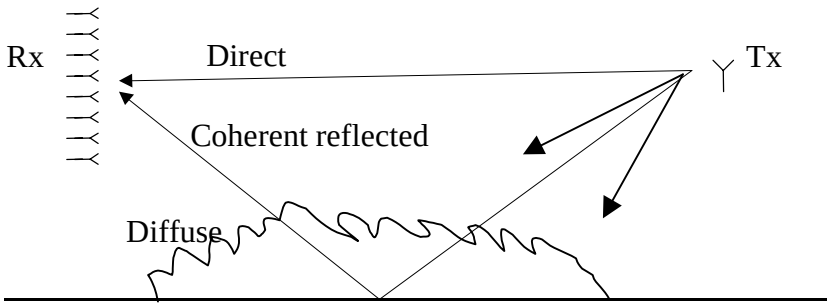

Figure 73. Illustration of the received signal, consisting of two plane waves and a contiuous, diffuse spectrum, grazing set-up

The received signal can be written as an 8-dimensional time function vector **x**(t)

$$\mathbf{x}(t) = \sum_{n=1}^{2} \alpha_n \cdot \mathbf{a}(\phi_n) \cdot u(t - \tau) + \mathbf{y}(t) + N(t) \qquad \textit{(eq. 175)}$$

The thermal noise N(t) has been assumed to be insignificant and is therefore ignored. Also, the compensation for the antenna radiation patterns has been omitted for clarity. In the equation, the **x**(t) is the total received signal vector, the two-term sum accounts for the contributions from the direct and coherent reflected components and **y**(t) is the contribution from the diffuse part of the spectrum. $[\alpha_n, \phi_n]$ are the amplitude and direction (defined as in Figure 74) of the direct and coherent reflected components as estimated by the ESPRIT-algorithm, u(t) is the sounding

time signal and $\mathbf{a}(\phi)$ is the array steering vector for the direction ϕ. The elements of the steering vector are defined as (if the phase reference is at element 0, Figure 74)

$$a_n(\phi) = e^{-jk_0 nd\cos\phi} \qquad \textit{(eq. 176)}$$

where $n \in [0,7]$ and d is the element separation, which was λ/2 in this case. This is illustrated in Figure 74, which shows the array geometry.

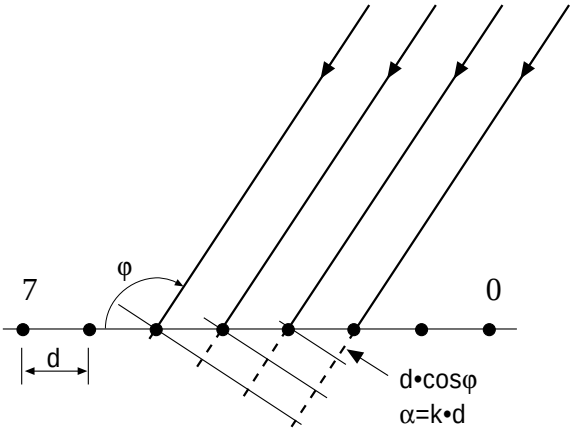

Figure 74. Illutstration of the geometry of the receiving antenna array

Eq. 175 can alternatively be written simply as

$$\mathbf{x}(t) = \mathbf{s}(t) + \mathbf{y}(t) \qquad \textit{(eq. 177)}$$

In this expression the **x**(t), which have been measured, and the **s**(t), which can be calculated as

$$\mathbf{s}(t) = \sum_{n=1}^{2} \alpha_n \cdot \mathbf{a}(\phi_n) \cdot u(t-\tau) \qquad \textit{(eq. 178)}$$

are known. An estimate of **y**(t) can therefore be found as

$$\mathbf{y}_{est}(t) = \mathbf{x}(t) - \mathbf{s}(t) \qquad \textit{(eq. 179)}$$

From the estimate of **y**(t) the diffuse signal spectrum can be found by performing a Fourier transform along the signal vector, as

$$F(\phi,\tau) = \sum_{n=0}^{7} y_n(\tau)\, \mathrm{e}^{-jk_0 nd\cos\phi} \qquad \textit{(eq. 180)}$$

where the geometry is the same as in Figure 74. Due to all the impinging signal components arriving within a time frame that is short compared to the sounding bandwidth, all the components will appear at approximately the same time delay τ_0, and all the information will appear at a cross-section of the three-dimensional function; $F(\phi, \tau_0)$. This will effectively remove the dependency on time delay in the analysis.

A simple illustration of the technique is shown in Figure 75. A signal consisting of 3 components was generated, two components with equal amplitude at 90° and 70°, plus a component at 80° with amplitude –20 dB relative to the other two. Figure 75 a) shows the Fourier spectrum of the total received signal, Figure 75 b) shows the spectrum with the direct (90°) component subtracted, whereas Figure 75 c) shows the spectrum of the remaining signal after the two strong components had been subtracted. The reason for the two peaks not having the same height in Figure 75 a) is the complex addition of the three signal contributions. Note the difference in scale in Figure 75 c) compared to Figure 75 a) and Figure 75 b), resembling the 20 dB amplitude difference.

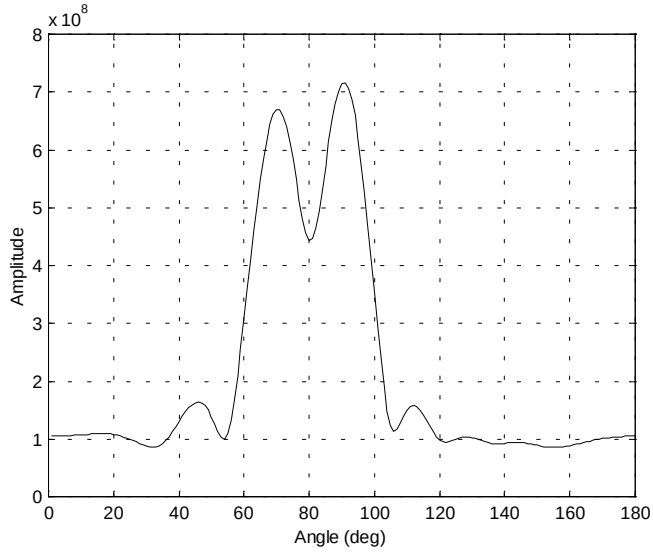

a)

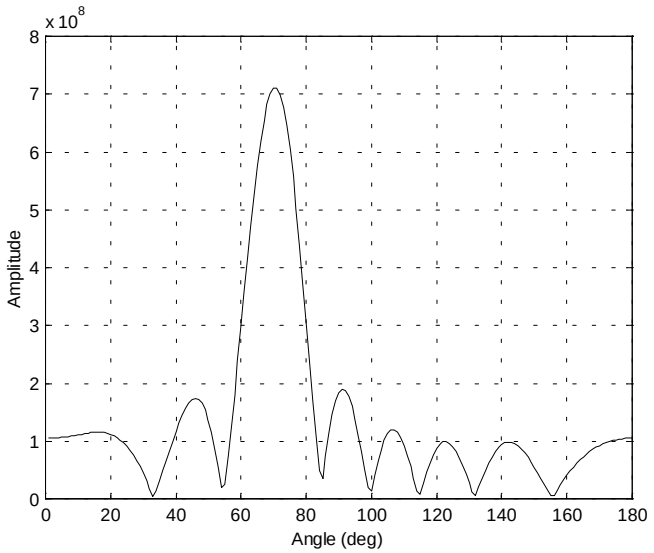

b)

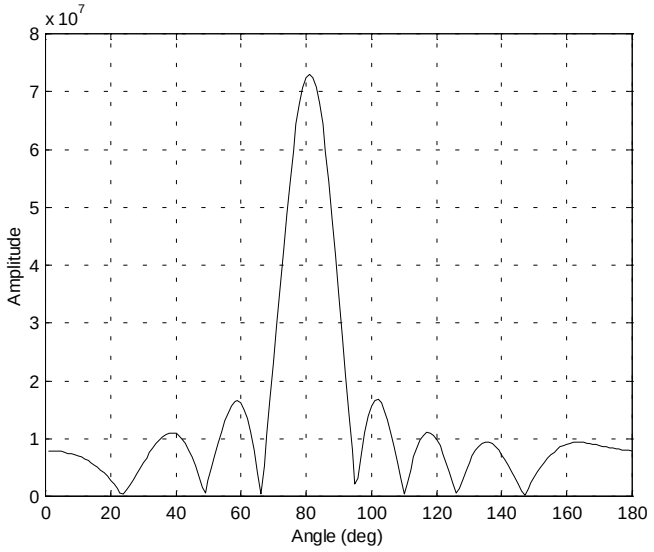

c)

Figure 75. Illustration of method which subtracts the effect of the direct and coherent components from the received signal and calculates the Fourier spectrum; a) spectrum of received signal, b) spectrum of signal with the direct component subtracted, c) spectrum of signal with the direct and coherent components subtracted

The estimation method can be summarised as follows:

1. Estimate Γ from the output of the ESPRIT algorithm.

2. Subtract the contributions of the direct and the coherent reflected components from the total received signal (using eq. 177, eq. 178 and eq. 179) to find the *diffuse received signal* **y**(t).
3. Estimate the diffuse received angular spectrum by performing a Fourier transform on **y**(t). The diffuse received spectrum can be used in the estimation of the roughness parameters Δh and Φ_0 in the A/P model.

Detailed steps in the method of analysis for the amplitude/phase model

Appendix E. Scattering and diffraction measurement results

Table 12 and Table 13 show the results from the analysis of the non-grazing measurements on asphalt, for horizontal and vertical incidence polarisation, respectively. Table 14 and Table 15 show the results from the non-grazing measurements on grass. Similarly, Table 16 and Table 17 show the results from measurements on a ploughed field. Table 18 shows the results from forest measurements. The Tables show the following values for each measurement series: the estimated power (percent) into coherent reflection, diffuse scattering and loss; the estimated value for the reflection coefficient Γ; the estimated value for the phase shift window Φ_0; the rms phase shift; and the corresponding estimated height variation for the surface.

Table 19 shows the results from the analysis of the grazing measurements. The Table shows the estimated values for the reflection coefficient Γ, but because of the lack of stability in the equipment mentioned in Chapter 5 the values are given in terms of the mean and median values. The number of measurements in each case is also indicated.

Pictures from the different measurement scenarios are shown at the end of this appendix. Figure 76 shows a picture from measurements on dry asphalt, Figure 77 shows a picture from wet asphalt, Figure 78 from grass, Figure 79 from ploughed field without snow, Figure 80 from ploughed field with snow and Figure 81 from forest.

Inc. angle [deg]	**Surface cond.**	**Power (%)**			**Refl. Coeff, Γ**	**Phase shift window, Φ_0, [deg]**	**Rms phase shift [deg]**	**Estimated height variation, Δh [cm]**
		Non-random, coherent	**Random, diffuse**	**Loss**				
30	dry	10.1	0.23	89.7	0.32	30	8.6	0.88
45	dry	14.9	0.86	84.2	0.40	47	13.5	1.70
60	dry	25.0	0.15	74.9	0.50	15.2	4.4	0.78
60	wet	22.4	*)	*)	0.47	*)	*)	*)
70	wet	70.4	*)	*)	0.83	*)	*)	*)

Table 12. Analysis results, asphalt, horizontal incident polarisation, *) Somewhat uncertain because of limited number of samples

Inc. angle [deg]	**Surface cond.**	**Power (%)**			**Refl. Coeff, Γ**	**Phase shift window, Φ_0, [deg]**	**Rms phase shift [deg]**	**Estimated height variation, Δh [cm]**
		Non-random, coherent	**Random, diffuse**	**Loss**				
30	dry	7.3	0.16	92.6	0.27	30	8.6	0.88
45	dry	7.0	0.86	92.1	0.27	39	11.2	1.40
60	dry	3.9	0.058	96.0	0.20	24	6.9	1.22
70	wet	5.3	*)	*)	0.23	*)	*)	*)

Table 13. Analysis results, asphalt, vertical incident polarisation, *) Somewhat uncertain because of limited number of samples

URN:NBN:no-1290

Inc. angle [deg]	Surface cond.	Power (%)			Refl. Coeff, Γ	Phase shift window, Φ_0, [deg]	Rms phase shift [deg]	Estimated height variation, Δh [cm]
		Non-random, coherent	Random, diffuse	Loss				
30	dry	3.8	0.48	95.8	0.21	69	20	2.03
45	dry	2.8	0.84	96.3	0.19	100	29	3.61
45	wet	12.0	*)	*)	0.35	*)	*)	*)

Table 14. Analysis results, grass, horizontal incident polarisation, *) Somewhat uncertain because of limited number of samples

Inc. angle [deg]	Surface cond.	Power (%)			Refl. Coeff, Γ	Phase shift window, Φ_0, [deg]	Rms phase shift [deg]	Estimated height variation, Δh [cm]
		Non-random, coherent	Random, diffuse	Loss				
30	dry	12.7	1.22	86.1	0.37	60	17.3	1.77
45	dry	4.6	0.59	94.8	0.23	69	20	2.49
45	wet	26.8	*)	*)	0.53	*)	*)	*)

Table 15. Analysis results, grass, vertical incident polarisation, *) Somewhat uncertain because of limited number of samples

Inc. angle [deg]	Surface cond.	Power (%)			Refl. Coeff, Γ	Phase shift window, Φ_0, [deg]	Rms phase shift [deg]	Estimated height variation, Δh [cm]
		Non-random, coherent	Random, diffuse	Loss				
50	dry	1.83	5.26	92.9	0.27	215	62	9.16
50	snow	5.53	0.67	93.8	0.25	67	19.3	2.66

Table 16. Analysis results, ploughed field, horizontal incident polarisation, *) Somewhat uncertain because of limited number of samples

Inc. angle [deg]	Surface cond.	Power (%)			Refl. Coeff, Γ	Phase shift window, Φ_0, [deg]	Rms phase shift [deg]	Estimated height variation, Δh [cm]
		Non-random, coherent	Random, diffuse	Loss				
50	dry	0.49	3.91	95.6	0.21	260	75	11.09
50	snow	5.3	4.3	90.4	0.31	148	43	5.90

Table 17. Analysis results, ploughed field, vertical incident polarisation, *) Somewhat uncertain because of limited number of samples

Inc. angle [deg]	Surface cond.	Power (%)			Refl. Coeff, Γ	Phase shift window, Φ_0, [deg]	Rms phase shift [deg]	Estimated height variation, Δh [cm]
		Non-random, coherent	Random, diffuse	Loss				
80	dry, in leaf	0 *)	0.87 *)	99.3 *)	0.093 *)	360	104	53.16

Table 18. Analysis results, forest, horizontal incident polarisation, *) Somewhat uncertain because of limited number of samples

Surface	Asphalt (dry)		Grass (dry)		Ploughed Field (without snow)	
Polarisation	**h**	**v**	**h**	**v**	**h**	**v**
# meas.	35	41	27	25	68	37
Mean Γ	0.48	0.89	0.62	0.89	0.57	0.29
Median Γ	0.44	0.91	0.61	0.86	0.55	0.30

Table 19. Estimation of reflection coefficient, grazing incidence, incidence angle 80-82°

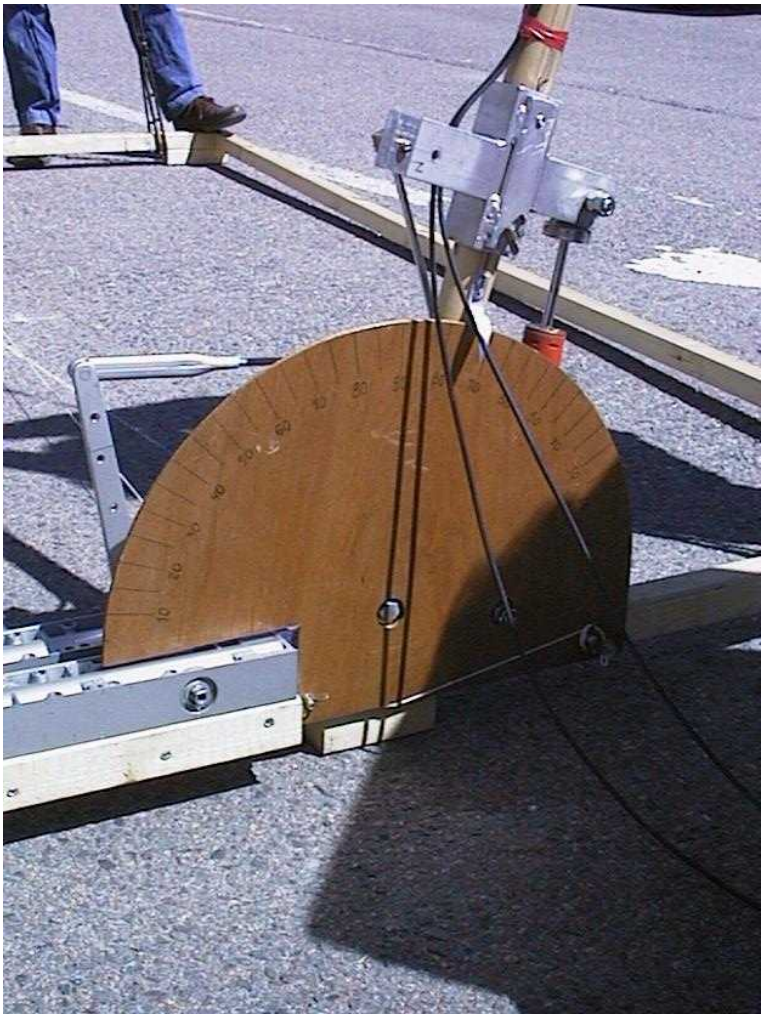

Figure 76. Picture from measurements on (dry) asphalt

Figure 77. Picture from measurements on (wet) asphalt

Figure 78. Picture from measurements on grass

Figure 79. Picture from measurements on ploughed field, without snow

Figure 80. Picture from measurements on ploughed field, with snow

Figure 81. Picture from measurements in forest

Appendix F. Results from comparison between scattering models

This appendix provides the results from the optimisation described in Chaper 6. The results are given in terms of the parameters from the optimisation, as well as the mean square error (dB) compared to measurements, relative to the amplitude/phase model.

Plane surface model

Table 20 shows the results from the analysis of the plane surface optimisation for asphalt. The Table shows the estimated Γ as well as the mean square error relative to the amplitude/phase model. Table 21 and Table 22 show similar results for grass and ploughed field, respectively.

Inc. angle (deg)	Surf. conditions	Polarisation (v or h)	Estimated Γ	Rel. mean square error (dB)
30	Dry	v	0.26	0.9
30	Dry	h	0.30	0.4
45	Dry	v	0.27	1.0
45	Dry	h	0.41	1.2
60	Dry	v	0.14	1.2
60	Dry	h	0.43	2.2

Table 20.Analysis results, optimisation plane surface model, asphalt.

Inc. angle (deg)	Surf. conditions	Polarisation (v or h)	Estimated Γ	Rel. Mean square error (dB)
30	Dry	v	0.27	1.3
30	Dry	h	0.19	1.7
45	Dry	v	0.18	3.4
45	Dry	h	0.18	3.5

Table 21. Analysis results, optimisation plane surface model, grass

Inc. angle (deg)	Surf. conditions	Polarisation (v or h)	Estimated Γ	Rel. mean square error (dB)
50	No snow	v	0.05	6.3
50	No snow	h	0.15	4.3

Table 22.Analysis results, optimisation plane surface model, ploughed field

Small perturbation method, initial estimation

Table 23 shows the results from the analysis of the Small perturbation method optimisation for asphalt. The Table shows the estimated values for correlation length L and the rms height variation h as well as the mean square error relative to the amplitude/phase model. Table 24 and Table 25 show similar results for grass and ploughed field, respectively.

Inc. angle (deg)	Surf. conditions	Polarisation (v or h)	Estimated L/λ	Estimated h/λ	Rel. mean square error (dB)
30	Dry	v	0.006	0.78	8.5
30	Dry	h	3.06	0.009	8.4
45	Dry	v	0.005	1.29	3.9
45	Dry	h	0.006	1.81	3.2
60	Dry	v	0.007	0.65	6.3
60	Dry	h	0.005	0.83	12.4

Table 23. Analysis results, optimisation Small perturbation method, asphalt

Inc. angle (deg)	Surf. conditions	Polarisation (v or h)	Estimated L/λ	Estimated h/λ	Rel. mean square error (dB)
30	Dry	v	0.010	0.82	4.1
30	Dry	h	1.84	0.007	11.8
45	Dry	v	0.004	2.32	11.0
45	Dry	h	0.004	1.43	13.4

Table 24. Analysis results, optimisation Small perturbation method, grass

Inc. angle (deg)	Surf. conditions	Polarisation (v or h)	Estimated L/λ	Estimated h/λ	Rel. mean square error (dB)
50	Dry	v	0.004	4.05	12.2
50	Dry	h	0.009	2.15	12.8

Table 25. Analysis results, optimisation Small perturbation method, ploughed field

Small perturbation method, measured permittivities

As Table 23 to Table 25 show, the assumed permittivity parameters for SPM lead to unrealistic values of L and h. An additional roughness analysis has been performed using better fitted values for the permittivities, taken from measurements. For a more detailed explaination, see Chapter 6. Table 26 shows the results from the analysis of the Small perturbation method optimisation for asphalt using the measured permittivity values as described in Section 6.2. The Table shows the estimated values for correlation length L and the rms height variation h as well

as the mean square error relative to the amplitude/phase model. Table 27 and Table 28 show similar results for grass and ploughed field, respectively.

Inc. angle (deg)	Surf. conditions	Polarisation (v or h)	Estimated L/λ	Estimated h/λ	Rel. mean square error (dB)
30	Dry	v	0.00	8.77	1.7
30	Dry	h	2.55	0.02	-1.5
45	Dry	v	0.01	2.69	3.2
45	Dry	h	0.01	6.05	0.8
60	Dry	v	0.00	0.13	9.4
60	Dry	h	1.03	3.75	6.7

Table 26. Analysis results, optimisation Small perturbation method, asphalt, measured permittivities

Inc. angle (deg)	Surf. conditions	Polarisation (v or h)	Estimated L/λ	Estimated h/λ	Rel. mean square error (dB)
30	Dry	v	0.00	6.20	4.9
30	Dry	h	0.01	9.07	0.7
45	Dry	v	0.02	5.75	3.3
45	Dry	h	0.01	1.92	7.0

Table 27. Analysis results, optimisation Small perturbation method, grass, measured permittivities

Inc. angle (deg)	Surf. conditions	Polarisation (v or h)	Estimated L/λ	Estimated h/λ	Rel. mean square error (dB)
50	Dry	v	0.00	32.56	1.3
50	Dry	h	0.03	1.89	5.6

Table 28. Analysis results, optimisation Small perturbation method, ploughed field, measured permittivities

Kirchoff model, initial estimation

Table 29 shows the results from the analysis of the Kirchoff model optimisation for asphalt. The Table shows the estimated values for correlation length L and the rms height variation h as well as the mean square error relative to the amplitude/phase model. Table 30 and Table 31 show similar results for grass and ploughed field, respectively.

Inc. angle (deg)	Surf. conditions	Polarisation (v or h)	Estimated L/λ	Estimated h/λ	Rel. mean square error (dB)
30	Dry	v	0.04	0.10	2.0
30	Dry	h	0.02	0.10	-0.3
45	Dry	v	0.27	0.08	0.8
45	Dry	h	0.23	0.10	0.9
60	Dry	v	0.55	0.14	0.4
60	Dry	h	0.58	0.16	4.2

Table 29. Analysis results, optimisation Kirchoff model, asphalt

Inc. angle (deg)	Surf. conditions	Polarisation (v or h)	Estimated L/λ	Estimated h/λ	Rel. mean square error (dB)
30	Dry	v	0.19	0.08	0.1
30	Dry	h	0.04	0.13	1.3
45	Dry	v	0.30	0.14	0.6
45	Dry	h	0.06	0.17	2.5

Table 30. Analysis results, optimisation Kirchoff model, grass

Inc. angle (deg)	Surf. conditions	Polarisation (v or h)	Estimated L/λ	Estimated h/λ	Rel. mean square error (dB)
50	Dry	v	1.23	0.76	2.7
50	Dry	h	0.38	0.28	2.7

Table 31. Analysis results, optimisation Kirchoff model, ploughed field

Kirchoff model, measured permittivities

Following the same approach as for SPM, an additional roughness analysis using measured permittivities were carried out. Table 32 shows the results from the analysis of the Kirchoff model optimisation for asphalt using the measured permittivity values as described in Section 6.3. The Table shows the estimated values for correlation length L and the rms height variation h as well as the mean square error relative to the amplitude/phase model. Table 33 and Table 34 show similar results for grass and ploughed field, respectively.

Inc. angle (deg)	Surf. conditions	Polarisation (v or h)	Estimated L/λ	Estimated h/λ	Rel. mean square error (dB)
30	Dry	v	0.19	0.00	2.0
30	Dry	h	0.16	0.03	-0.3
45	Dry	v	0.19	0.00	3.3
45	Dry	h	0.00	0.00	0.6
60	Dry	v	0.00	0.00	11.0
60	Dry	h	0.34	0.11	4.1

Table 32. Analysis results, optimisation Kirchoff model, asphalt, measured permittivities

Inc. angle (deg)	Surf. conditions	Polarisation (v or h)	Estimated L/λ	Estimated h/λ	Rel. mean square error (dB)
30	Dry	v	0.19	0.00	5.2
30	Dry	h	0.00	0.08	0.3
45	Dry	v	0.00	0.00	7.0
45	Dry	h	0.16	0.08	1.2

Table 33. Analysis results, optimisation Kirchoff model, grass, measured permittivities

Inc. angle (deg)	Surf. conditions	Polarisation (v or h)	Estimated L/λ	Estimated h/λ	Rel. mean square error (dB)
50	Dry	v	0.00	0.00	3.9
50	Dry	h	0.25	0.19	9.6

Table 34. Analysis results, optimisation Kirchoff model, ploughed field, measured permittivities

Oren model

Table 35 shows the results from the analysis of the Oren model optimisation for asphalt. The Table shows the estimated values for R and σ^2 as well as the mean square error relative to the amplitude/phase model. Table 36 and Table 37 show similar results for grass and ploughed field, respectively.

Inc. angle (deg)	Surf. conditions	Polarisation (v or h)	Estimated R	Estimated σ^2	Rel. mean square error (dB)
30	Dry	v	1.26	2.1e10	8.2
30	Dry	h	1.40	1.5e10	8.9
45	Dry	v	0.64	7.7e-9	5.9
45	Dry	h	1.63	1.8e-8	5.1
60	Dry	v	0.15	4.1e-7	11.0
60	Dry	h	1.87	7.5e-10	13.2

Table 35. Analysis results, optimisation Oren model, asphalt

Inc. angle (deg)	Surf. conditions	Polarisation (v or h)	Estimated R	Estimated σ^2	Rel. mean square error (dB)
30	Dry	v	1.46	2.2e10	6.2
30	Dry	h	1.00	1.3e8	5.2
45	Dry	v	0.34	2.0e-7	7.4
45	Dry	h	0.54	5.5e-8	4.3

Table 36. Analysis results, optimisation Oren model, grass

Inc. angle (deg)	Surf. conditions	Polarisation (v or h)	Estimated R	Estimated σ^2	Rel. mean square error (dB)
50	Dry	v	0.49	0.38	-0.5
50	Dry	h	0.81	2.7e-7	-0.4

Table 37. Analysis results, optimisation Oren model, ploughed field

Appendix G. Simulation results from sensitivity analysis

Table 38, Table 39 and Table 40 show simulation results from the analysis from the example case Bristol, for land use forest, field and grass. Table 41, Table 42, and Table 43 show similar results for example case Lillehammer. The Tables show the value of the 2D component, the mean Rx-level as well as values for different percentiles in the cumulative distribution function.

			Prob. P<p (%)						
2D comp. Attenuation (dB)	**2D Comp (dBm)**	**Mean Rx Power (dBm)**	**1**	**5**	**10**	**50**	**90**	**95**	**99**
0.0	-51.8	-51.6	-55.3	-54.0	-53.5	-51.7	-50.1	-49.8	-49.1
5.0	-56.8	-56.4	-63.9	-61.0	-59.8	-56.4	-54.1	-53.6	-53.2
10.0	-61.8	-61.1	-75.8	-69.4	-66.9	-60.9	-57.9	-57.6	-56.7
15.0	-66.8	-63.9	-82.0	-75.1	-72.0	-64.2	-59.5	-58.6	-57.5
20.0	-71.8	-65.3	-83.8	-77.1	-74.0	-65.9	-60.8	-59.7	-58.0
25.0	-76.8	-66.0	-84.5	-77.8	-74.7	-66.6	-61.4	-60.2	-58.4
30.0	-81.8	-66.2	-84.6	-78.0	-74.9	-66.7	-61.5	-60.4	-58.6
35.0	-86.8	-66.2	-84.6	-78.0	-75.0	-66.8	-61.6	-60.5	-58.7
40.0	-91.8	-66.3	-85.0	-78.0	-75.0	-66.8	-61.6	-60.5	-58.7
45.0	-96.8	-66.3	-85.0	-78.0	-75.0	-66.8	-61.6	-60.5	-58.7
50.0	-101.8	-66.3	-85.0	-78.1	-75.0	-66.8	-61.6	-60.5	-58.7

Table 38. Results from example case Bristol. Surface forest.

			Prob. P<p (%)						
2D Attenuation (dB)	**2D Comp (dBm)**	**Mean Rx Power (dBm)**	**1**	**5**	**10**	**50**	**90**	**95**	**99**
0.0	-51.8	-51.7	-54.6	-53.7	-53.2	-51.7	-50.5	-50.1	-49.6
5.0	-56.8	-56.6	-62.4	-60.3	-59.3	-56.6	-54.5	-54.1	-53.6
10.0	-61.8	-61.1	-73.7	-68.3	-66.2	-61.2	-57.9	-57.2	-56.0
15.0	-66.8	-64.7	-82.4	-75.4	-72.4	-64.9	-60.5	-59.6	-58.1
20.0	-71.8	-66.6	-85.0	-78.3	-75.2	-67.2	-62.1	-61.1	-59.4
25.0	-76.8	-67.5	-85.7	-79.3	-76.1	-68.1	-62.9	-61.8	-60.1
30.0	-81.8	-67.8	-86.6	-79.6	-76.5	-68.4	-63.2	-62.1	-60.3
35.0	-86.8	-67.9	-86.6	-79.7	-76.6	-68.4	-63.3	-62.2	-60.4
40.0	-91.8	-67.9	-86.6	-79.7	-76.6	-68.5	-63.3	-62.2	-60.5
45.0	-96.8	-67.9	-86.6	-79.7	-76.6	-68.5	-63.4	-62.2	-60.5
50.0	-101.8	-67.9	-86.6	-79.7	-76.6	-68.5	-63.4	-62.2	-60.5

Table 39. Results from example case Bristol. Surface field.

			Prob. P<p (%)						
2D Attenuation (dB)	**2D Comp (dBm)**	**Mean Rx Power (dBm)**	**1**	**5**	**10**	**50**	**90**	**95**	**99**
0.0	-51.8	-51.7	-53.0	-52.6	-52.4	-51.8	-51.2	-51.0	-50.7
5.0	-56.8	-56.6	-59.0	-58.2	-57.9	-56.7	-55.6	-55.3	-54.9
10.0	-61.8	-61.6	-66.2	-64.7	-64.0	-61.7	-59.9	-59.5	-58.7
15.0	-66.8	-66.2	-76.0	-72.1	-70.4	-66.3	-63.5	-62.8	-61.7
20.0	-71.8	-70.2	-86.8	-80.1	-77.2	-70.4	-66.3	-65.4	-64.1
25.0	-76.8	-72.7	-90.9	-84.3	-81.2	-73.2	-68.3	-67.3	-65.6
30.0	-81.8	-73.9	-92.6	-85.6	-82.6	-74.4	-69.3	-68.2	-66.5
35.0	-86.8	-74.3	-92.6	-86.2	-83.1	-74.9	-69.8	-68.7	-66.9
40.0	-91.8	-74.5	-92.6	-86.2	-83.2	-75.0	-69.9	-68.8	-67.1
45.0	-96.8	-74.5	-92.6	-86.3	-83.2	-75.1	-69.9	-68.8	-67.1
50.0	-101.8	-74.5	-92.9	-86.3	-83.3	-75.1	-69.9	-68.9	-67.1

Table 40. Results from example case Bristol. Surface grass.

			Prob. P<p (%)						
2D Attenuation (dB)	**2D Comp (dBm)**	**Mean Rx Power (dBm)**	**1**	**5**	**10**	**50**	**90**	**95**	**99**
0.0	-64.6	-64.3	-69.6	-67.7	-66.8	-64.3	-62.3	-61.9	-61.2
5.0	-69.6	-69.0	-80.6	-75.7	-73.7	-69.0	-66.1	-65.6	-65.1
10.0	-74.6	-72.6	-89.8	-83.1	-80.2	-72.9	-68.6	-67.6	-66.2
15.0	-79.6	-74.8	-93.3	-86.4	-83.4	-75.3	-70.3	-69.2	-67.5
20.0	-84.6	-75.8	-94.4	-87.6	-84.5	-76.3	-71.2	-70.1	-68.3
25.0	-89.6	-76.1	-94.5	-87.9	-84.8	-76.7	-71.5	-70.3	-68.6
30.0	-94.6	-76.2	-94.9	-88.0	-84.9	-76.8	-71.6	-70.5	-68.7
35.0	-99.6	-76.2	-94.9	-88.0	-84.9	-76.8	-71.6	-70.5	-68.7
40.0	-104.6	-76.3	-94.9	-88.0	-85.0	-76.8	-71.6	-70.5	-68.7
45.0	-109.6	-76.3	-94.9	-88.0	-85.0	-76.8	-71.6	-70.5	-68.7
50.0	-114.6	-76.3	-94.9	-88.0	-85.0	-76.8	-71.6	-70.5	-68.7

Table 41. Results from example case Lillehammer. Surface forest.

			Prob. P<p (%)						
2D Attenuation (dB)	**2D Comp (dBm)**	**Mean Rx Power (dBm)**	**1**	**5**	**10**	**50**	**90**	**95**	**99**
0.0	-64.6	-64.5	-66.0	-65.6	-65.3	-64.5	-63.8	-63.6	-63.2
5.0	-69.6	-69.5	-72.3	-71.4	-71.0	-69.5	-68.3	-67.9	-67.4
10.0	-74.6	-74.3	-80.1	-78.0	-77.1	-74.3	-72.3	-71.8	-71.1
15.0	-79.6	-78.8	-91.2	-85.9	-83.9	-78.9	-75.7	-75.0	-73.8
20.0	-84.6	-82.5	-100.0	-93.2	-90.2	-82.7	-78.3	-77.4	-75.9
25.0	-89.6	-84.5	-103.0	-96.1	-93.0	-85.0	-79.9	-78.9	-77.2
30.0	-94.6	-85.3	-104.0	-97.0	-94.0	-85.9	-80.7	-79.6	-77.8
35.0	-99.6	-85.6	-104.5	-97.5	-94.4	-86.2	-81.0	-79.9	-78.1
40.0	-104.6	-85.7	-104.5	-97.5	-94.4	-86.3	-81.1	-80.0	-78.2
45.0	-109.6	-85.8	-104.5	-97.5	-94.5	-86.3	-81.2	-80.0	-78.3
50.0	-114.6	-85.8	-104.5	-97.7	-94.5	-86.4	-81.2	-80.1	-78.3

Table 42. Results from example case Lillehammer. Surface field

Simulation results from sensitivity analysis

			Prob. P<p (%)						
2D Attenuation (dB)	**2D Comp (dBm)**	**Mean Rx Power (dBm)**	**1**	**5**	**10**	**50**	**90**	**95**	**99**
0.0	-64.6	-64.5	-65.0	-64.9	-64.9	-64.6	-64.3	-64.3	-64.1
5.0	-69.6	-69.5	-70.4	-70.1	-70.0	-69.5	-69.1	-69.0	-68.8
10.0	-74.6	-74.4	-76.1	-75.6	-75.4	-74.5	-73.7	-73.5	-73.2
15.0	-79.6	-79.4	-82.5	-81.6	-81.1	-79.5	-78.1	-77.8	-77.2
20.0	-84.6	-84.2	-90.4	-88.2	-87.2	-84.3	-82.1	-81.6	-80.7
25.0	-89.6	-88.8	-102.2	-96.5	-94.2	-88.8	-85.5	-84.8	-83.5
30.0	-94.6	-92.0	-109.9	-102.9	-99.9	-92.3	-87.9	-87.0	-85.5
35.0	-99.6	-94.0	-112.7	-105.7	-102.7	-94.5	-89.5	-88.5	-86.8
40.0	-104.6	-94.8	-113.2	-106.5	-103.2	-95.3	-90.3	-89.2	-87.5
45.0	-109.6	-95.0	-113.2	-106.7	-103.6	-95.5	-90.5	-89.4	-87.7
50.0	-114.6	-95.1	-113.2	-106.7	-103.7	-95.6	-90.6	-89.5	-87.8

Table 43. Results from example case Lillehammer. Surface grass

Table 44 shows the results from example case Bristol, in the cases of field with snow and grass with water. The Table shows the attenuation of the 2D component, the value of the corresponding 2D component and the mean of the resulting distribution. Table 45 shows similar results for Lillehammer.

2D comp. Attenuation (dB)	Field with snow		Grass with water	
	2D Comp (dBm)	Mean Rx Power (dBm)	2D Comp (dBm)	Mean Rx Power (dBm)
0.0	-51.8	-51.6	-51.8	-51.7
5.0	-56.8	-56.5	-56.8	-56.6
10.0	-61.8	-60.9	-61.8	-61.4
15.0	-66.8	-64.3	-66.8	-65.6
20.0	-71.8	-66.1	-71.8	-68.6
25.0	-76.8	-66.8	-76.8	-70.1
30.0	-81.8	-67.1	-81.8	-70.6
35.0	-86.8	-67.2	-86.8	-70.8
40.0	-91.8	-67.2	-91.8	-70.9
45.0	-96.8	-67.2	-96.8	-70.9
50.0	-101.8	-67.2	-101.8	-70.9

Table 44. Results from example case, Bristol. Surface field with snow ad grass with water

2D Attenuation (dB)	Field with snow		Grass with water	
	2D Comp (dBm)	Mean Rx Power (dBm)	2D Comp (dBm)	Mean Rx Power (dBm)
0	-64.6	-64.5	-64.6	-64.5
5	-69.6	-69.5	-69.6	-69.5
10	-74.6	-74.4	-74.6	-74.3
15	-79.6	-79.2	-79.6	-79.4
20	-84.6	-83.4	-84.6	-84.1
25	-89.6	-86.5	-89.6	-88.1
30	-94.6	-88.1	-94.6	-91.0
35	-99.6	-88.7	-99.6	-92.2
40	-104.6	-89.0	-104.6	-92.7
45	-109.6	-89.0	-109.6	-92.9
50	-114.6	-89.1	-114.6	-93.0

Table 45. Results from example case, Lillehammer. Surface field with snow and grass with water

Table 46, Table 47 and Table 48 show the mean received value in the case of land use field for example case Bristol, with varying values of ε_r, Δh and σ, respectively. Table 49, Table 50 and Table 51 show similar results for example case Lillehammer. In all cases 2D attenuation of 10 dB as well as infinite (3D only) has been simulated.

	2D comp. attenuation (dB)	
ε_r	**10**	**Inf. (3D only)**
1.2	-61.6	-76.1
2	-61.6	-73.2
3	-61.5	-71.8
4	-61.4	-70.5
5	-61.3	-69.5
6	-61.2	-68.6
7	-61.1	-67.9
8	-61.0	-67.3
9	-60.8	-66.9
10	-60.8	-66.5
11	-60.7	-66.1
12	-60.6	-65.8
13	-60.6	-65.5
14	-60.4	-65.3
15	-60.4	-65.0
16	-60.3	-64.8
17	-60.2	-64.6
18	-60.2	-64.5
19	-60.2	-64.3
20	-60.1	-64.1

Table 46. Simulation results from example case Bristol. Sensitivity analysis for the mean value of the received power due to variations of ε_r .

Δh (cm)	2D comp. attenuation (dB)	
	10	**Inf. (3D only)**
0.4	-61.8	-90.0
2	-61.6	-76.3
4	-61.4	-71.2
6	-61.2	-69.1
8	-61.1	-68.2
10	-61.1	-67.9
12	-61.1	-67.8
14	-61.0	-67.6
16	-61.0	-67.4
18	-61.0	-67.1
22	-60.9	-66.7
30	-60.7	-65.9
40	-60.5	-65.2

Table 47. Results from example case Bristol. Sensitivity analysis for the mean value of the received power due to variations of Δh.

σ	2D comp. attenuation (dB)	
	10	**Inf. (3D only)**
0.000	-61.1	-67.9
0.150	-61.1	-67.9
0.285	-61.1	-67.9

Table 48. Results from example case Bristol. Sensitivity analysis for the mean value of the received power due to variations of σ.

ε_r	2D comp. attenuation (dB)	
	10	**Inf. (3D only)**
1.2	-74.2	-84.1
2	-74.2	-82.2
3	-74.1	-82.9
4	-74.2	-83.7
5	-74.3	-84.6
6	-74.3	-85.3
7	-74.3	-85.8
8	-74.3	-86.1
9	-74.3	-86.3
10	-74.3	-86.3
11	-74.3	-86.3
12	-74.3	-86.2
13	-74.3	-86.1
14	-74.3	-85.9
15	-74.3	-85.7
16	-74.3	-85.5
17	-74.2	-85.2
18	-74.3	-85.0
19	-74.2	-84.8
20	-74.2	-84.6

Table 49. Simulation results from example case Lillehammer. Sensitivity analysis for the mean value of the received power due to variations of ε_r .

	2D comp. attenuation (dB)	
Δh (cm)	**10**	**Inf. (3D only)**
0.4	-84.5	-120.8
2	-84.5	-107.0
4	-84.4	-101.5
6	-84.4	-98.8
8	-84.3	-97.1
10	-84.3	-95.8
12	-84.3	-94.6
14	-84.2	-93.5
16	-84.2	-92.6
18	-84.2	-91.9
22	-83.9	-90.7
30	-83.6	-89.1
40	-83.3	-88.1

Table 50. Simulation results from example case Lillehammer. Sensitivity analysis for the mean value of the received power due to variations of Δh

	2D comp. attenuation (dB)	
σ	**20**	**40**
0.000	-74.3	-85.8
0.150	-74.3	-85.7
0.285	-74.3	-85.4

Table 51. Simulation results from example case Bristol. Sensitivity analysis for the mean value of the received power due to variations of σ.